Probing Structure and Dynamics with Photoelectrons generated in Strong Fields

The front part of the cover shows a strong field photoelectron hologram of xenon 6s. By ionizing xenon 6s with 7 µm radiation from the Free Electron Laser for IntraCavity Experiments (FELICE), this image was obtained. After performing numerical calculations, we could proof that this is actually a hologram of the xenon 6s, formed by the photoelectrons from the atom itself. A large part of this thesis is focussed on this phenomenon. On the back side, three different photoelectron measurements are displayed: ionization of xenon 12s (middle left) with 31.2 µm radiation, ionization of xenon 7p with 7 µm (bottom right) and ionization of a superposition of xenon 6s and 7p with 16 µm (top right).

ISBN: 978-90-77209-60-8

An electronic version of this thesis is available at www.amolf.nl/publications

Probing Structure and Dynamics with Photoelectrons generated in Strong Fields

PROEFSCHRIFT

ter verkrijging van de graad van Doctor
aan de Radboud Universiteit Nijmegen,
op gezag van de rector magnificus
prof. mr. S.C.J.J. Kortmann,
volgens besluit van het college van decanen
in het openbaar te verdedigen op woensdag 2 mei 2012
om 13.30 uur precies

door

Ymkje Huismans

Geboren op 25 januari 1982
te Amsterdam

Promotor:	Prof. dr. M. J. J. Vrakking
Manuscriptcommissie:	Prof. dr. D. H. Parker Prof. dr. W. Becker, Max Bron Institute, Berlin Dr. A. F. Koenderink, FOM Instituut AMOLF

Nederlandse titel: Meten van Beweging en Structuur met in Sterke Velden gegenereerde Fotoelektronen

The work described in this thesis was performed at the FOM-institute AMOLF, Science Park 104, 1098 XG, Amsterdam, The Netherlands.

This work is part of the research programme of the 'Stichting voor Fundamenteel Onderzoek der Materie (FOM)', which is financially supported by the 'Nederlandse Organisatie voor Wetenschappelijk Onderzoek (NWO)'.

Contents

1 Introduction

"It's of no use whatsoever... This is just an experiment that proves Maestro Maxwell was right, we just have these mysterious electromagnetic waves that we cannot see with the naked eye. But they are there."

This is what Heinrich Hertz said about his experimental discovery of the photoelectric effect in 1887 [1], clearly underestimating its value. In 1922 Einstein received the Nobel Prize for the theoretical description [2] and nowadays the photoelectric effect is used in many devices, ranging from digital cameras to remote controls. Beside its technical applications, the photoelectric effect is at the basis of a huge variety of experimental techniques that investigate the properties of atoms, molecules, solid states and biologically relevant samples. This beautifully demonstrates how seemingly useless discoveries can turn out to be very valuable instead.

Curiosity driven and based on the photoelectric effect, are current efforts to resolve ultrafast electron dynamics. Because electrons play a crucial role in all chemical reactions, resolving their dynamics is relevant for many scientific fields, ranging from atomic and solid state physics to biology. It is however challenging to do so, since this dynamics takes place on an attosecond timescale (10^{-18} s), which implies that one should invent a "camera" with an attosecond shutter time. Until recently this was not possible, but in the last decade, two techniques have emerged that are able to resolve and steer electron dynamics in atoms and small molecules.

Both methods are based on high harmonic generation (HHG), a process in which via ionization and re-absorption higher harmonics of the fundamental ionization frequency are emitted. The process is commonly explained by the three step model, as introduced by Corkum [3]. In the first step a gas target, usually consisting of rare gas atoms, is tunnel-ionized by an intense infrared laser field. In the continuum the photoelectrons oscillate in the laser electric field and can be driven back to the target ion (second step), where they can recombine and emit radiation with photon-energies proportional to the energy gained by the electrons in the laser field (third step). The resulting light spectrum consists of higher harmonics that upon proper tuning can constitute an attosecond pulse train [4] or even an isolated attosecond pulse (current world record: 80 as [5]).

Both the attosecond pulses as well as the HHG signal itself can be used to probe attosecond dynamics. When using attosecond pulses the most common

method is to perform a pump probe experiment, as pioneered by Zewail for probing femtosecond (10^{-15} s) dynamics [6]. By continuously varying the time delay between a pump, which initiates a particular reaction, and a probe, which probes its current status, a movie of the involved dynamics can be made. Femtosecond resolution is most commonly achieved by laser pulses with a pulse duration on the order of femtoseconds. This allows one to study molecular dynamics and it has become a wide field of research, called femtochemistry, in which major achievements have been made in following chemical reactions on their relevant timescales. The attosecond XUV light however allows for resolving the attosecond electron dynamics. In the optimal situation both pump and probe are an attosecond pulse, but due to the low intensities of attosecond XUV pulses, the probe is usually replaced by a femtosecond infrared laser field. Many studies have successfully used a streaking method [7–9] or other XUV pump - IR probe method to resolve electron dynamics. Examples are the measurements of small delays in the photoionization from different orbitals [10], the stepwise ionization dynamics that occurs in a strong laser field [11], the measurement of the Auger lifetimes [12], the electron dynamics in solid states [13] and the evolution and control of electron localization in H_2 and D_2 [14].

Attosecond temporal information is also stored in the high harmonic signal together even with Ångström spatial information. This is due to the fact that the high harmonic generation constitutes a pump probe experiment itself, as nicely demonstrated in Figure 1.1. The pump is the moment of ionization, induced by the infrared laser, the probe is the recombination event, during which spatial information is stored in the phase and amplitude of the high harmonics. Since each harmonic is created with a different time delay between ionization and recombination, they provide individual snapshots of a movie. In 2004 Itatani at al performed a pioneering experiment using the HHG-signal to reconstruct the shape of the highest occupied molecular orbital (HOMO), demonstrating its high spatial resolution. Furthermore they demonstrated theoretically that also sub-femtosecond time information is encoded in the harmonic signal [16]. Recording both spatial and temporal evolution of orbitals was for example done by Smirnova *et al.*, who expanded this technique to resolve multi-electron dynamics in CO_2 [17]. These and many other experiments demonstrate the great potential of higher harmonics for resolving electron distributions and (multi) electron and hole dynamics.

Besides following attosecond electron dynamics (HHG and attosecond spectroscopy) and femtosecond molecular dynamics (femtochemistry), the time-dependent determination of molecular structure is another important aspect of the real time following of chemical reactions, that can be achieved by employing short pulsed XUV or X-ray radiation. Photoelectrons resulting from this ionization can "illuminate the molecule from within". If the de Broglie wavelength of the photoelectrons is on the order of the interatomic spacing, they can record a diffraction or holographic image of the molecule by scattering off the neighboring atoms in the molecule. Using synchrotron radiation, this is an established method for the structure determination of crystals (see references [18–24] and references therein). Provided that the orientation of the molecules is known, this method can also be used for gas-phase molecules as shown by the pioneering experiment of Landers *et al.* [25], who recorded a diffraction pattern of CO with synchrotron radiation.

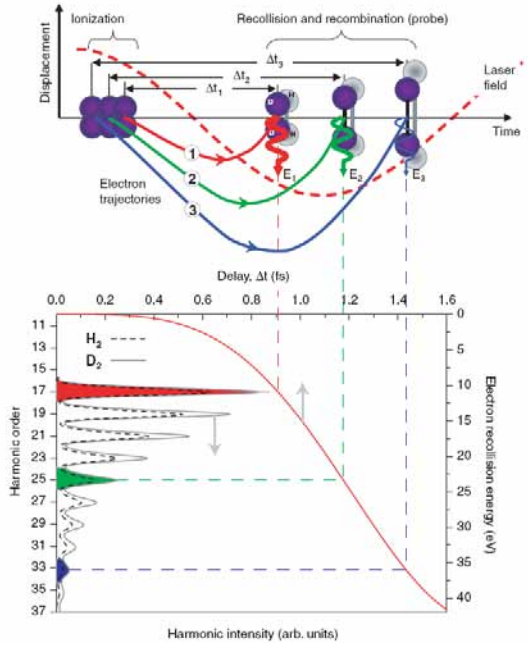

FIGURE 1.1: **Encoding of nuclear dynamics within harmonic spectra**. Upper panel: The trajectory of the ionized electron differs depending on the exact time of ionization. Three possible electron trajectories labeled 1, 2, and 3 are shown, which recollide with the molecular ion after delays Δt_1, Δt_2, and Δt_3, with increasing kinetic energy E_1, E_2, and E_3, resulting in the emission of increasingly higher frequency photons after recombination (shown as the 17^{th}, 25^{th}, and 33^{rd} harmonics for the purpose of this illustration). Note: Although the curves in the lower panel are physically accurate, the electron trajectories shown in the upper panel have been slightly altered to improve clarity. (Figure and caption taken from Baker *et al.* [15]).

Recording both structural and temporal information of molecules requires the use of short pulsed XUV of X-ray radiation instead of synchrotron radiation. Currently the required photon energies and light intensities of attosecond XUV-radiation are not sufficient [26, 27]. However with the commissioning of the free electron laser in Stanford (Lineac Coherent Light Source, LCLS) in 2009 [28], the hard X-ray regime is reached in combination with few femtosecond pulse durations and high pulse energies enabling one to time-dependently "illuminate molecules from within".

Apart from using the X-ray photons to ionize the target, they can also be used to scatter. X-ray photons generated in synchrotron facilities are commonly used to create diffraction patterns of crystals in order to retrieve their structure. However, the high intensities required usually deteriorate the sample. This problem can be overcome by using the femtosecond X-ray pulses from LCLS, which are short enough to probe systems before heavy damage sets in. This has been demonstrated very recently by two seminal experiments from Chapman *et al.* [29]

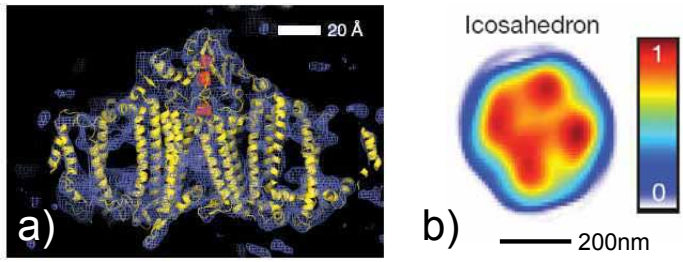

FIGURE 1.2: (Left) Electron density map (blue mesh) retrieved from the acquired diffraction pattern with 1.8keV LCLS radiation and pulseduration of 70fs. The yellow structure was obtained from a refined model. (Right) Reconstructed image of the mimivirus particle that shows an inhomogeneous distribution of dense material inside the viron. (Figure taken from [29, 30])

and Seibert *et al.* [30], who respectively managed to image a crystallized membrane protein with 8.5 Å resolution (Figure 1.2a) and retrieve the structure of a non-crystalline mimi-virus in a single shot experiment (Figure 1.2b).

All these experiments and theoretical investigations are based on the use of novel light sources. They beautifully demonstrate how we can use the light-matter interaction to follow dynamics down to the attosecond timescale and how we can (time dependently) probe various types of spatial distributions, ranging from molecular orbitals to non-crystalline large scale molecules. In this thesis a new method will be presented that has the potential to follow electron dynamics with attosecond time resolution and molecular dynamics with a few femtosecond time- and Ångström spatial resolution. The method is based on the concept of holography [31] in combination with strong field ionization. In conventional holography a coherent light or electron beam is split into two identical beams that travel different paths: a reference beam that goes to the detector directly and an object beam that first scatters off the target. The interference of the object and reference beam on a detector, constitutes a hologram containing spatial information about the target. In a strong field experiment, a coherent beam of electrons is created by tunnel ionization. The ionized electrons (from here on called "electron wave packets", whenever their wave nature needs to be stressed) follow different trajectories in the continuum under the influence of the laser field. Depending on their initial lateral velocity (i.e. velocity orthogonal to the laser polarization), either the electron wave packet will return to the target and scatter or it will make a wide turn and go to the detector without any interaction with the target (see Figure 1.3). In this way an object wave (the scattering electron wave packet) and a reference wave (the direct electron wave packet) are created, just as in conventional holography. The interference of the reference and object wave on the detector results in a hologram of the target. Because there is for every electron trajectory a different time delay between ionization and scattering (similar to HHG), also time information is stored. For wavelengths of a few µm, the corresponding time resolution is on the order of a few femtoseconds for probing the dynamics of the target and even sub femtoseconds for probing the ionization dynamics.

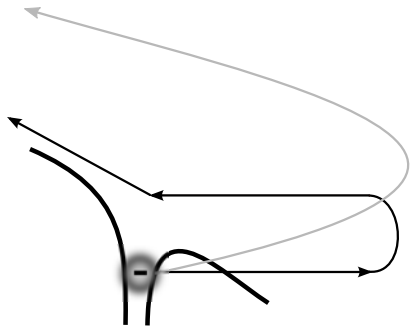

FIGURE 1.3: **Concept of strong field photoelectron holography.** Electron wave packets are generated via tunnel ionization (grey and black arrow). Once in the continuum their motion is governed by the laser electric field. Depending on their initial velocity component orthogonal to the laser polarization, the electron wave packet will either be turned around and make a wide turn around the ion (grey line) or will be driven back to the ion and scatter (black line). The first type of electron wave packets form a reference wave, the second type the object wave. The interference pattern of the electron waves constitutes a hologram on the detector, storing temporal and spatial information on the ionization dynamics and targets structure.

In this thesis the first measurement of a strong field photoelectron hologram will be presented along with a detailed theoretical analysis of the pattern demonstrating that for the correct choice of laser parameters, time information on a sub-femtosecond scale and spatial information with Ångström resolution is encoded in the photoelectron hologram. This work paves the way to investigate the possibility to establish time-resolved photoelectron holography as a new technique to resolve ultrafast time- and atomic spatial information. This technique could be complementary to other techniques, given the possibility to use long wavelengths in combination with moderate intensities, making it ideal for studying larger molecules, i.e. molecules with a small ionization potential.

Besides the proof of photoelectron holography and the extensive analysis, other patterns observed in the three dimensional photoelectron spectra arising from the strong field ionization of atoms and molecules will be presented. Upon ionizing selected xenon Rydberg states, ionization dynamics will be studied and the specific fingerprint that each atomic orbital leaves on the final electron distribution will be unraveled. Furthermore a study on the large and complex C_{60} molecule will be presented, in which its electron dynamics and electron correlation effects are investigated.

Because all these studies are based on strong field ionization, in the following a short overview on strong field physics and its basic concepts is given. To be able to appreciate and understand the observed and analyzed structures in the presented three-dimensional photoelectron momentum spectra, this introductory chapter will subsequently zoom in on the rich amount of information stored in the photoelectron signal. In the last part a detailed outline of the thesis and the achievements will be given.

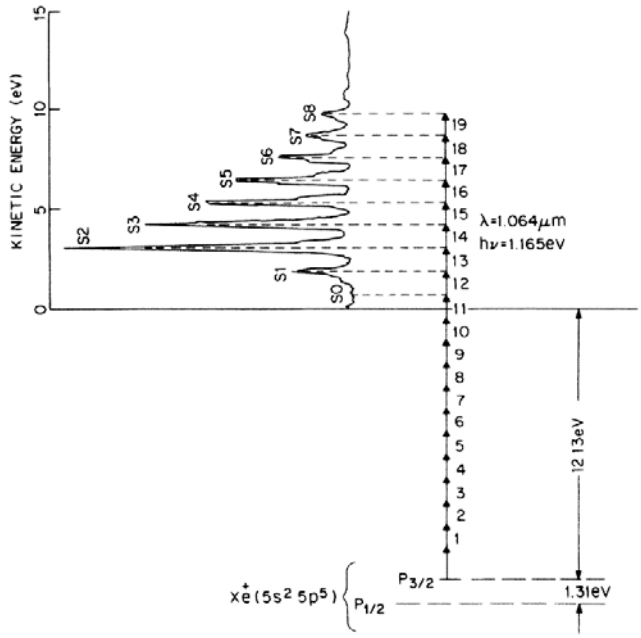

FIGURE 1.4: Typical ATI spectrum measured in xenon with a wavelength of 1064 nm and an intensity exceeding $1 \cdot 10^{13}$ W/cm^2. The multiphoton absorption process is schematically indicated in the spectrum (figure taken from [32])

1.1 Strong Field Ionization

With the advent of the laser in 1960, it became possible to ionize atoms and molecules in a strong field, where "strong" refers to a field strength which is comparable to the Coulomb force that binds the electron. As opposed to the standard photoelectric effect, which is characterized by a single photon absorption process, strong field ionization is non-linear and happens via the absorption of a number of photons. In 1979 Agostini *et al.* [33] showed that the electrons can even absorb photons in excess of the ionization threshold, leading to peaks in the photoelectron spectrum that are separated by the photon energy. This mechanism is called Above Threshold Ionization (ATI) and a typical spectrum arising from the ionization of xenon is shown in Figure 1.4.

Besides ionizing the target, the strong laser field also induces a Stark Shift, which up-shifts the ionization threshold. Consequently the effective ionization potential increases and the final kinetic energy of the photoelectron is given by (in atomic units (a.u.)):

$$E = n\omega - (\mathrm{IP} + U_p) \tag{1.1}$$

With the number of absorbed photons n, the energy of one photon ω, the ionization potential IP and ponderomotive energy U_p. The latter is the average quiver

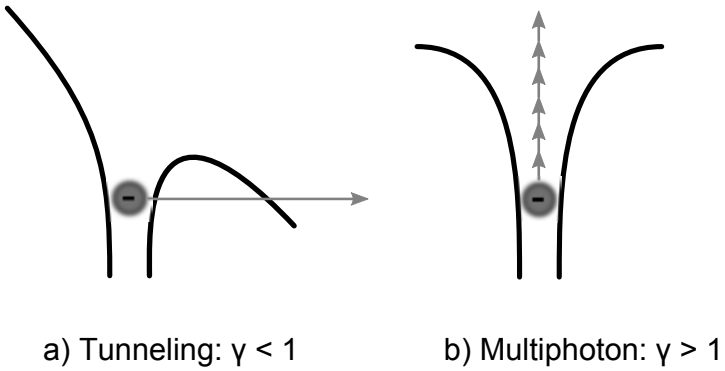

FIGURE 1.5: Schematic drawing of the two ionization regimes .a) If $\gamma < 1$, the laser field suppresses the Coulomb barrier such that the electron can tunnel out. b) If $\gamma > 1$, ionization happens "vertically", by the absorption of a multiple number of photons.

energy which an electron has in the laser field and is defined by $U_p = F^2/4\omega^2$, with the laser parameters F and ω for respectively the field strength and the frequency. Since U_p is equal to the induced Stark Shift, the effective ionization potential is $(\mathrm{IP}+U_p)$. This is usually called the "Up-shift", because it shifts the photoelectron peaks by U_p. When the light intensity increases, U_p increases too, and the whole spectrum shifts towards lower energy. In an experiment the laser focus usually exhibits a Gaussian transversal intensity distribution, with the highest intensities found in the center of the beam. Consequently the target experiences different ionization intensities and different Up-shifts, which results in a gradual broadening of the ATI peaks. For very high intensities, the Up-shift induced by the peak intensity can easily exceed the photon energy and wash out the ATI structure completely.

The ionization pathway illustrated in Figure 1.4 is "vertically". However, depending on the laser parameters and the ionization potential of the target, the ionization can proceed differently. Already in 1964 Keldysh introduced a parameter to distinguish between two ionization pathways [34]. The so called Keldysh parameter is given by $\gamma = \sqrt{\mathrm{IP}/2U_p} = (\omega/F)\sqrt{\mathrm{IP}}$, where $\gamma > 1$ marks the "multiphoton regime" and $\gamma < 1$ the "tunnel-ionization regime". The parameter depends on three variables, the laser field strength, the laser frequency and the ionization potential. The effect of the laser field is to distort the potential barrier as illustrated in Figure 1.5a. In case the field is strong enough, the forbidden region separating the initial state from the ionization continuum, becomes so thin that the electron can quantum mechanically tunnel through, provided that there is enough time to do so. In case either the frequency is too high to create a static barrier or the field strength is too weak to sufficiently suppress it, the electron can only escape via the vertical pathway as discussed before and illustrated in Figure 1.5b.

After ionization the interaction with the laser is not over; in the oscillating field the electron will follow a quiver motion. By simply applying Newton's equations it can be demonstrated that the maximum energy transferred from the laser

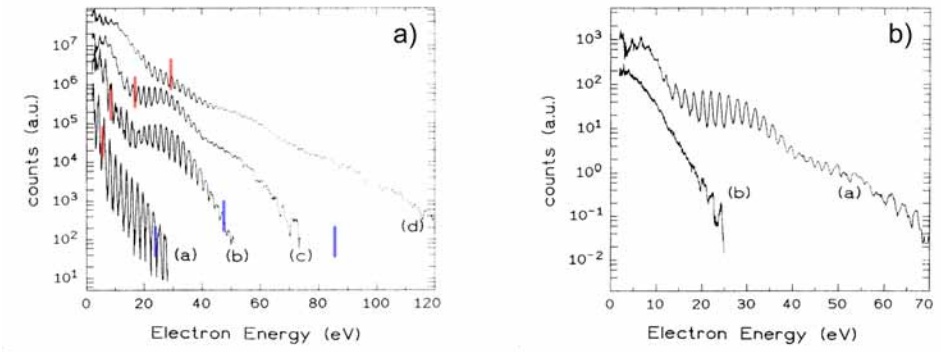

FIGURE 1.6: ATI spectra from the ionization of argon with 40 fs, 630 nm pulses. a) Ionization at different intensities (a) $6 \cdot 10^{13}$ W/cm^2, (b) $1.2 \cdot 10^{14}$ W/cm^2, (c) $2.4 \cdot 10^{14}$ W/cm^2, (d) $4.4 \cdot 10^{14}$ W/cm^2. The $2U_p$ and $10U_p$ cut-offs are marked by respectively red and blue vertical stripes. b) Ionization at $2.4 \cdot 10^{14}$ W/cm^2 with (a) linear polarized and (b) circularly polarized light. Spectra taken from Paulus *et al.* [35]

field to the electron is twice the ponderomotive energy ($2U_p$) [3, 36–38]. Consequently the photoelectron yield in the ATI spectrum shows a drop at this energy. This is shown in Figure 1.6a where the ATI spectrum of argon was measured for a range of intensities and in which the $2U_p$ cut-off energies are marked by red stripes. The signal does however not drop to zero at $2U_p$, instead a plateau is observed that extends to much higher energies. This effect is caused by scattering. When the electron oscillates in the laser electric field, it can be driven back to the target, where it can either be absorbed by or scatter off the parent ion. Upon scattering and subsequent oscillation in the field, the electron can gain a maximum energy of $10U_p$, as marked by blue stripes in Figure 1.6a. The experimental proof that the plateau is caused by recollision-electrons is given in Figure 1.6b, where the photoelectron spectrum is measured for both linearly polarized and circularly polarized light. In the latter case, the chance for the electron to return to the core is highly suppressed and indeed no plateau is visible.

1.2 Photoelectron Signal

Photoelectrons form a rich source of information on ionization pathways, electron dynamics and the structure of molecular orbitals. Below, major achievements in studying (angularly resolved) photoelectron spectra are discussed.

1.2.1 One Dimensional Photoelectron spectra

In conventional photoelectron spectra the electron yield is recorded versus the kinetic energy of the photoelectrons, resulting in spectra like displayed in Figure 1.4 and 1.6. Many aspects of the strong laser - matter interaction have been revealed by these type of spectra, such as its non-linear character resulting in

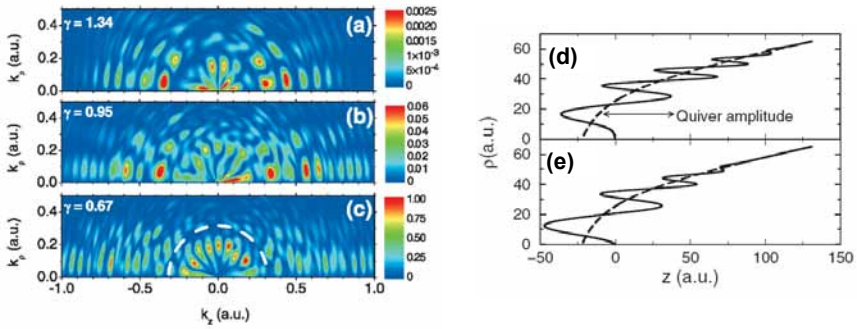

FIGURE 1.7: Left: TDSE calculations on the ionization of Hydrogen, with a wavelength of 910 nm and various intensities leading to values for the Keldysh parameter of (a) $\gamma = 1.34$, (b) $\gamma = 0.95$, (c) $\gamma = 0.67$. In figure (c) the flower pattern emerges for very low energies, as marked by the white dashed circle. Right: Classical trajectories of laser driven electrons (solid lines) and unperturbed Kepler hyperbola (dashed lines). The two trajectories displayed differing in the number of quiver oscillations, (e) has one more oscillation than trajectory displayed in (d). Figures taken from Arbó *et al.* [40].

the ATI pattern [33], the typical dynamics of electrons in a strong laser field leading to the $2U_p$ and $10U_p$ cut-offs [3, 35–38] and Stark shifting of the ionization threshold leading to the U_p shift of the ATI peaks [39]. The Stark shift is also crucial in the observation of yet another effect, the Freeman resonances. In 1987 Freeman reported the observation of substructures in the ATI peak, which repeat themselves in each subsequent ATI peak [39]. This effect is attributed to ionization via resonant intermediate states and is caused by the fact that only states close to the ionization threshold experience the full stark Stark shift, while the ground state does not. When keeping the frequency fixed, different Rydberg states can shift into resonance as the intensity is changed. As mentioned before, in the focal volume a range of intensities is present, leading to the resonant ionization of different states and hence the observed substructure in the ATI peaks. For different peak intensities, these structures appear at the same position, since they experience the same shift as the ionization threshold, i.e. they do not show the U_p shift.

1.2.2 Angular resolved Photoelectron spectra

Due to the extra dimension involved in angular resolved photoelectron spectra additional information is stored. Below a selection of major discoveries is given, to which will often be referred in the various chapters of this thesis.

Low energy electrons

Low energy electrons play a special role in photoelectron spectra, since they are most strongly influenced by the parent ion's Coulomb Potential. One example is the "flower pattern"; a highly structured photoelectron angular distribution that emerges in the tunneling regime, close to zero kinetic energy. In 2004 Rudenko *et*

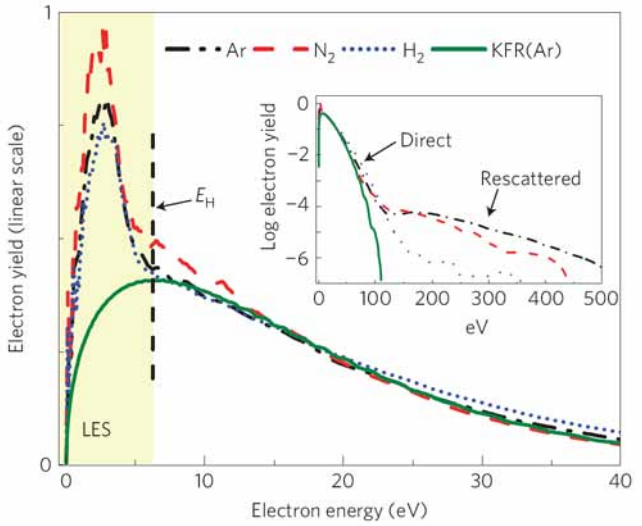

FIGURE 1.8: Photoelectron spectra for argon, nitrogen, and hydrogen ionized with $1.5 \cdot 10^{12}$ W/cm^2, and 2 µm. In green the Keldysh-Faisal-Reiss (KFR) method is used to calculate the photoelectron spectrum, clearly not reproducing the Low Energy Structure (LES). Figure taken from Blaga *et al.* [42].

al. measured this pattern in Argon [41] and two years later Arbó *et al.* explained the effect by applying two theoretical models [40]: a "Time Dependent Schrödinger Equation" (TDSE) model, that solves the Schrödinger Equation exactly for a one electron system and a "Coulomb Trajectory Monte Carlo simulation with Tunneling" (CTMC-T) that is based on calculating the electron trajectories in a semi-classical way. In Figure 1.7 the results of the TDSE calculation on the ionization of Hydrogen, for a laser wavelength of 910 nm and different values for the Keldysh parameter are shown. The highly oscillatory pattern in Figure 1.7c can be described in terms of a superposition of Legendre polynomials that is dominated by $\ell_0 = 8$. This exactly corresponds to the angular momentum of the Kepler hyperbola that the electron follows in the combined laser and Coulomb field, as inferred from an analytical derivation and the CTMC-T model and shown in Figures 1.7d, e. Measurements and calculations on other atomic species show that this effect is universal and independent of the core potential. It is consequently the long range Coulomb potential combined with the laser field that dictates the electrons motion and its final angular momentum.

Another remarkable effect is the "Low Energy Structure", described by Blaga an coworkers in 2009 [42]. It is signified by a peak in the photoelectron spectrum at very low energies that only appears for wavelengths in the mid-infrared regime and that scales with the Keldysh parameter (Figure 1.8). Yan *et al.* demonstrated that this effect is due to electrons that are emitted in the direction away from the detector and are subsequently turned around by the laser field as well as alter

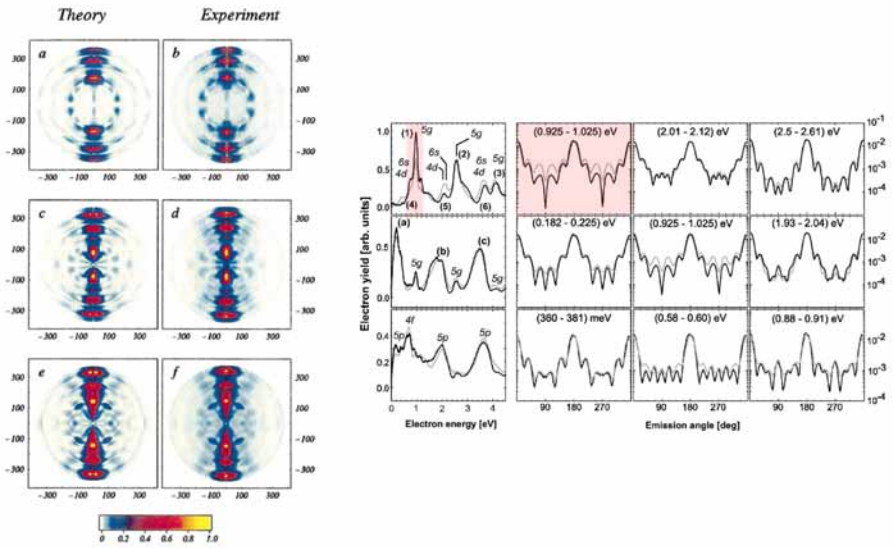

FIGURE 1.9: Left: Theoretical and experimental photoelectron momentum distributions resulting from the ionization of Argon with 800 nm and $I = 3.8 \cdot 10^{13}$ W/cm^2 (a,b), $I = 5 \cdot 10^{13}$ W/cm^2 (c,d) and $I = 7 \cdot 10^{13}$ W/cm^2 (e,f). Right: the first column shows angular integrated photoelectron spectra for $I = 3.8 \cdot 10^{13}$ W/cm^2 (top), $I = 5 \cdot 10^{13}$ W/cm^2 (middle) and $I = 7 \cdot 10^{13}$ W/cm^2 (bottom). In the following columns the angular distributions are shown for specific energy intervals. Figures taken from Wiehle *et al.* [44].

their lateral momentum due to the interaction with the Coulomb force [43].

Multiphoton absorption and resonances

Upon ionizing rare gasses in the multiphoton regime, highly structured photoelectron angular distributions were observed for ATI orders up to energies extending well into the plateau region [44–46]. In these experiments ionization usually passes through a resonant state (Freeman resonance, see above). It was demonstrated that the final angular distribution depends on the angular momentum of the resonant state, plus the number of photons absorbed from the resonance state to the continuum. The theory behind this is that upon each photon absorption the angular momentum can change by $\ell = \pm 1$. So if for example the ionization process passes through a resonant state with angular momentum $\ell = 4$, i.e. a g-state, its final angular momentum after the absorption of one more photon to reach the continuum will be $\ell = 3$ or $\ell = 5$, leading to respectively 3 or 5 nodes in the angular distribution over 180 degrees. This is nicely demonstrated by the measurements and TDSE calculations from Wiehle *et al.* as presented in Figure 1.9. The left figure shows the calculated and measured photoelectron angular momentum spectrum for three different intensities, all showing highly structured features. In the right figure the angular distribution in each energy regime is analyzed in detail. The first column shows the angular integrated photoelectron spectra for the same three intensities. The following columns show the corresponding angular distri-

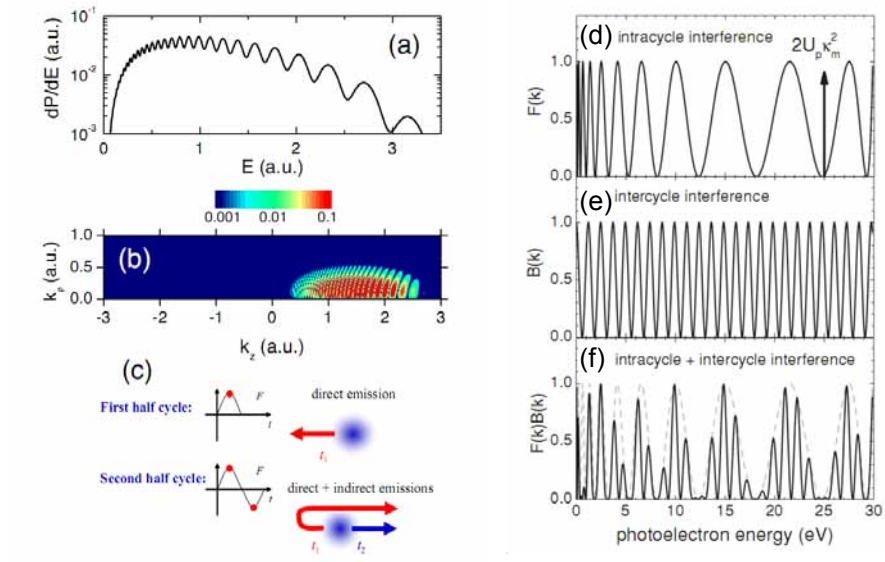

FIGURE 1.10: Left: (a) semi-classical photoelectron spectra resulting from the ionization of Hydrogen, with $\lambda = 910$ nm and $I = 2 \cdot 10^{14}$ W/cm^2 and a single laser cycle. (b) corresponding momentum distribution. (c) Schematic diagram to illustrate the ionization and continuum dynamics of the photoelectron responsible for the observed interference pattern. Figure taken from [47]. Right: Semiclassical intra-cycle (d) and inter-cycle (e) interference patterns for hydrogen ionized with $\lambda = 1$ µm and $I = 1.6 \cdot 10^{14}$ W/cm^2. (f) Total semiclassical interference for two cycle ionization. Figure taken from [48].

bution of certain energy intervals as specified in the figures. Highly structured angular distributions are measured, which can be related to the resonant states through which the ionization passed, as identified in the photoelectron spectra. As an example let's focus on the highlighted angular momentum spectrum. Here five antinodes are observed, corresponding to an angular momentum of $\ell = 5$ as in agreement with the fact that the ionization passes through the 5g state ($\ell = 4$) from which it needs one more photon to get to the continuum.

Electron Wavepacket Interferences

Electron wave packets are ionized at different instances in the laser cycle and can follow different trajectories in the continuum. The acquired phase difference leads to an interference pattern on the detector. ATI is an example of such an interference pattern. In the subsection on ATI its origin was explained in the energy domain, as the absorption of multiple photons in excess of the ionization threshold. ATI can, however, also be explained in the time domain, by electron wave packet interferences. When the laser field reaches a maximum the chance for tunneling and releasing an electron wave packet is the highest. This happens twice per laser cycle, once at the negative maximum and once at the positive maximum. The interference of photoelectrons that are ionized every cycle, i.e. with a time

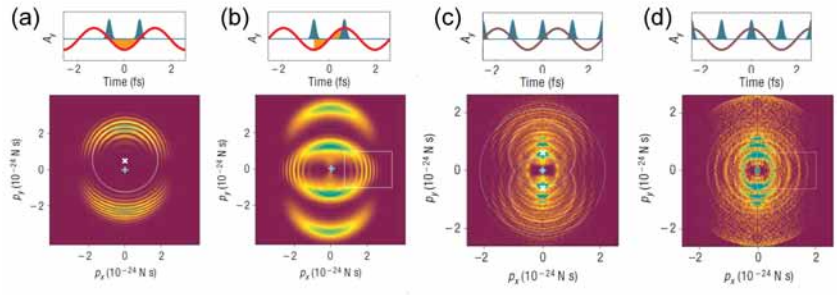

FIGURE 1.11: (a,b) Photoelectron momentum spectra of helium ionized by two 180-as, 46 eV pulses synchronized to an infrared field, as calculated by a TDSE method. (c,d) Measured Photoelectron momentum spectra of argon ionized with an attosecond pulse train with pulses of about 200 as and 11 eV, synchronized to an infrared field. Figure taken from [51]

separation of a full laser cycle, forms the ATI pattern. This is thus an inter-cycle interference for which a minimum number of 2 laser cycles is required. The electron wave packets from each half laser cycle can also interfere, forming a different type of oscillation in the photoelectron spectrum. This intra-cycle interference effect, for which only one laser cycle is required, was measured with short laser pulses [49, 50]. By applying a semiclassical calculation Arbó *et al.* reproduced the pattern as shown in Figures 1.10a and b [47]. It is an ATI like pattern, but the maxima in the spectrum are not evenly spaced in energy. The cartoon in Figure 1.10c shows the electron trajectories responsible for the interference and their ionization times.

In the right Figures 1.10d, e the difference between the intra-cycle interference and inter-cycle interference is shown, which clearly shows the unevenly spaced intra-cycle interference pattern and an evenly spaced inter-cycle interference pattern, corresponding to ATI. In Figure 1.10f the superposition of both interferences is shown.

In quite a different experiment Remetter *et al.* [51] developed interferometric techniques for retrieving the phase of electron wave packets. In optical interferometry, the light wave of interest is split into two replicas that either travel a different path or are given a different shear. The same can be done for photoelectrons by ionizing the atom with two consecutive attosecond XUV pulses that create two coherent electron wave packets i.e. two replicas. The shear or path difference can be induced by synchronizing the ionization to an IR-field. The idea is illustrated by TDSE calculations in Figure 1.11a, b. As demonstrated in Figure 1.11a, a path difference is created by synchronizing the ionization to the zeros of the vector potential ($A(t) = 0$) of the IR-field, because the first electron experiences half an oscillation more than the second one. An energy shear can be induced by synchronizing the ionization to the maxima of the vector potential ($A(t) = A_0$) of the IR-field. Because the field transfers a momentum of $-eA(t)$ to the electron, the two replicas will get an energy shear of respectively $-eA_0$ and $+eA_0$. From the resulting interference pattern the phase of the continuum

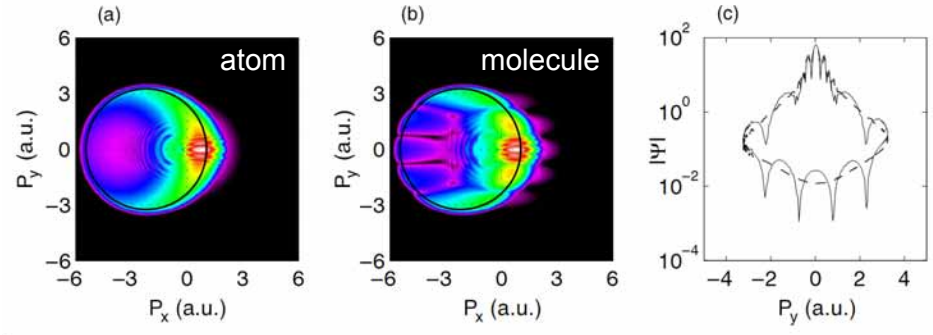

FIGURE 1.12: Semiclassical calculations on recollision-induced diffraction for a single phase of birth. (a) Reference signal $|\Psi(v_x, v_y)|$ for a model atom, each new color corresponds to the next order of magnitude; (b) $|\Psi(v_x, v_y)|$ for a model diatomic molecule; (c) circular cuts for the atom (dashed) and the molecule (solid). Figure taken from [52].

electron wave packet can be determined. In Figures 8c and d experimental results are shown that allowed for the partial retrieval of the phase. Full retrieval was not yet possible, since these measurements were complicated by the use of an attosecond pulse train, leading to multiple ionization events instead of only two and by the fact that the ground state wavefunction of argon is not a simple $\ell = 0$, $m = 0$ state, but a $\ell = 1$, $m = 0$ or $m = \pm 1$ state, resulting in a superposition of final m-states. However, the fact that an attosecond pulse train is used and not a two single attosecond pulses, does highlight the similarity of this process to a standard strong field ionization process resulting from a single color experiment. In the latter case, photoelectrons are ionized dominantly at the maxima of the laser electric field, which is identical to the process shown in Figure 1.11b, where the XUV ionizes electrons at the zeros of the vector potential (i.e. the maxima of the field). In this figure an oscillatory pattern is observed that arises from electron wave packet interferences and which resembles patterns described in the paragraph on multiphoton absorption. This suggests that these patterns can be described by both conservation of angular momentum upon photon absorption, as outlined in that paragraph, as well as arising from electron wave packet interferences, as suggested by the experiment from Remetter. Furthermore it indicates that also multiphoton absorption happens dominantly at the laser field maxima. This topic will be addressed in this thesis.

Diffraction

As mentioned earlier in this Introduction, continuum electrons can be driven back to the target-ion by the laser field, scatter off and create a holographic pattern upon interfering with the unscattered electrons. Without interfering with any direct electron, the scattered electrons can also form a diffraction pattern that, just as in photoelectron holography, contains both spatial and temporal information. The idea to use rescattering electrons to probe molecular dynamics dates back to 1996, when it was proposed by the group of Bandrauk [53]. In 2002 Niikura *et*

al. thoroughly investigated the properties of the returning electron wave packet, showing that the electron current at the target is many orders of magnitude higher than currently produced by state of the art electron guns [54]. This, and the inherent time resolution provided by recolliding electron wave packets make these electrons an ideal probe for attosecond dynamics. A detailed analysis on the retrieval and interpretation of the diffraction pattern was given by Spanner *et al.* [52]. In Figure 1.12 their semiclassical calculations on strong field ionization of an atom and a diatomic molecule are shown. Electrons with identical rescattering energy lie on a circle with radius $v(t)$, displaced from the centre by $v_0 sin\omega t$. Here $v(t)$ is the rescattering velocity and v_0 is defined by $v_0 = F/t$. In Figure 1.12c a spectral cut is shown that shows both fast and slow oscillations. For both the atomic and molecular target fast oscillations occur in a narrow region where direct and scattered electrons contribute to the final signal. They can be considered as a hologram of the target, as extensively studied in this thesis. The diffraction signal however occurs in a region where only scattered electrons contribute and it is characterized by coarse oscillations that are only present in the molecular spectrum and from which the internuclear distance can be derived.

The first measurement on molecular diffraction was done by Meckel *et al.* [55]. By taking the circular cuts as introduced above, the internuclear distance of the O_2 molecule could be determined. They furthermore demonstrated that the tunnel ionized electrons carry a fingerprint of the Highest Occupied Molecular Orbital (HOMO), as shown in Figure 1.13, where the photoelectron angular distributions for ionization of molecular oxygen and nitrogen ion are shown. Below the experimental data theoretical calculations are shown that are in excellent agreement with the experiment and reveals patterns that are specific to the HOMOs of respectively O_2 and N_2.

1.3 Outline of this thesis

The examples given above show that photoelectron signals carry a rich amount of information on the ionization pathways, electron dynamics and targets structure. Furthermore the high current density of returning electron wave packets and the accompanying high spatial and temporal resolution make them an ideal probe for ultrafast dynamics. These aspects of strong field photoelectron spectroscopy are utilized to unravel ionization dynamics and most importantly to obtain the first experimental proof of time-resolved strong field photoelectron holography. In the first six chapters, xenon is ionized with mid-infrared laser light. Besides the fact that hardly any strong field experiments have been performed in the mid-infrared wavelength regime, these wavelengths also provided ideal conditions to study high lying Rydberg states as well as to obtain the first experimental proof of time-resolved photoelectron holography. In the last chapter the complex C_{60} molecule is studied, which can serve as a model for other complex molecules.

The long wavelengths used in chapters were obtained from the Free Electron Laser for IntraCavity Experiments (FELICE). The benefit of performing experiments in the cavity is that all the light is used, instead of the 1% fraction coupled out. This leads to available pulse energies of up to at least 0.5 mJ. This, in com-

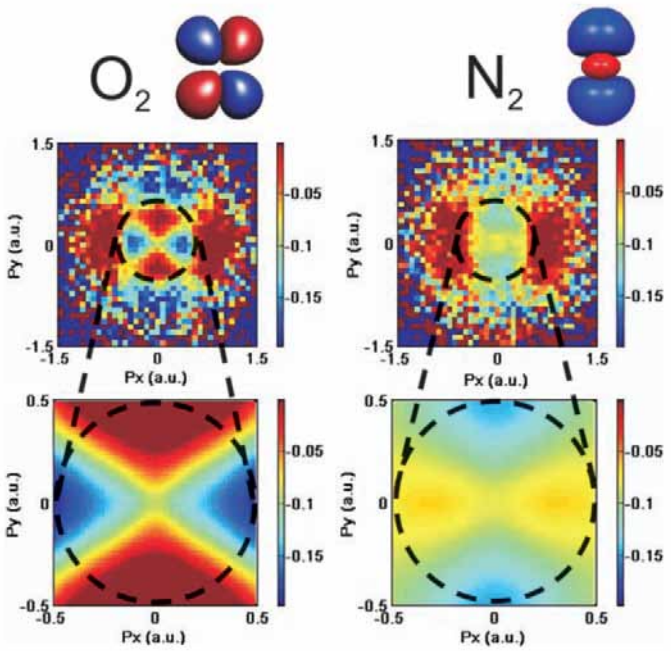

FIGURE 1.13: Two-dimensional photoelectron signal taken in the plain orthogonal to the direction of the laser polarization (p_z), to observe the imprint of the structure of the HOMO. The signal is a normalized difference signal from aligned and anti-aligned molecules, ionized with $\lambda = 800$ nm, $I = 2.5 \cdot 10^{14}$ W/cm^2 and $tau = 40$ fs. Left: from top to bottom: HOMO of O_2, experimental data and theoretical calculation. Left: from top to bottom: HOMO of N_2, experimental data and theoretical calculation. Figure taken from Meckel *et al.* [55].

bination with the integrated Velocity Map Imaging spectrometer, which measures the electron momenta in all directions, created the possibility to do high quality strong field ionization experiments in the mid-infrared wavelength regime.

The first chapter on the exploration of the mid-infrared regime is Chapter 2, called "Mid-infrared Ionization of Xenon Rydberg States". Wavelengths ranging from 24 to 31 µm were used to ionize different high lying Rydberg states in xenon, like the 10s, 11p, 11d and 8f state. The different ℓ-states leave their own typical imprint on the final photoelectron angular distribution. Furthermore we investigated the evolution of the three-dimensional photoelectron spectra as a function of wavelength for the ionization of both the 10s and 11p state. Using a number of theoretical models, the rich angular distributions observed in the lower order ATI peaks were analyzed from two perspectives; as a multiphoton absorption process in which the angular momentum of the photoelectron is conserved and as an electron wave packet interference pattern.

By going to shorter wavelengths (~ 7 µm) and ionizing xenon metastable atoms

(6s), spectacular patterns emerged that were new to us. After extensive theoretical modeling we could prove that we had measured a hologram of the xenon ion, containing both spatial and temporal information. Because of the novelty of this topic and its possible interesting applications, Chapters 3 up to 7 deal with this discovery of photoelectron holography.

In Chapter 3, "Time-Resolved Holography with Photoelectrons", the observation of photoelectron hologram of xenon 6s is shown, obtained by ionization with 7 µm light. The experimental observation of the hologram was confirmed by a TDSE calculation and two semiclassical methods, the generalized Strong FIeld Approximation (gSFA) and the Coulomb Corrected Strong Field Approximation (CCSFA). Both methods are based on the Strong Field Approximation (SFA), a common theoretical method in Strong Field Physics. In SFA an expression for the ionization amplitude is obtained by solving the time-dependent Schrödinger equation with the approximation that in the continuum the photoelectron only experiences the laser field and that the Coulomb force can be neglected. The gSFA method improves on SFA by including scattering. With this method it was possible to demonstrate that the holographic image stores time information on both the target structure as well as on the ionization dynamics, with respectively few-femtosecond and sub-femtosecond resolution. To get closer to the real experiment the CCSFA method was employed, which also includes the long range Coulomb force. Despite being a semi-classical method remarkably good quantitative agreement with the experimental data was obtained. Furthermore the ability to trace the electron trajectories in this code, make it an ideal play ground to gain detailed insight on how specific patterns are generated. In Chapter 4, "Strong Field Approximation Theories", these two methods (gSFA and CCSFA) are derived and described in detail.

While being puzzled and excited about holographic patterns, we decided to study its evolution with wavelength and intensity. The pattern remained almost unchanged upon varying the intensity, explaining its persistence in a focal volume averaged ionization experiment. At the same time clear changes were observed upon tuning the wavelength from 8 to 16 µm. With the gSFA and CCSFA methods, it was possible to analyze and explain these trends with wavelength and intensity, even analytically, as outlined in Chapter 5, "Scaling laws for photoelectron holography in the mid-infrared wavelength regime".

In Chapter 6, "Criteria for the observation of strong-field photoelectron holography" the experimental observation of holographic patterns for wavelengths as short as 800 nm is reported. This observation triggered the theoretical investigation on the criteria for observing photoelectron holography. Upon exploring a wide range of parameters by performing TDSE calculations we obtained an empirical law for the observation of the hologram. Last but not least the holographic pattern turned out to be sensitive to the shape of the atomic orbital, as shown in Chapter 7, "Sub-cycle interference dynamics of time-resolved photoelectron holography with mid-infrared laser pulses". In this chapter also other sub-cycle interference patterns are investigated, that demonstrate that all interference patterns are characterized by an oscillating structure in energy, except for the holographic interference which manifests itself in the angular direction. This makes it possible to distinguish the photoelectron hologram from the other interferences.

The first steps taken in "photoelectron holography", as outlined in chapter 3 to 7, show that the photoelectron signal carries high resolution time and spatial information making them an ideal probe for time resolving dynamics on a sub-femtosecond time scale. The next step is obviously to investigate how time and spatial information can be retrieved from the hologram.

The final goal in strong field physics is to time-resolve dynamics in larger molecules. This is a challenging and complicated goal. Current studies are mostly focused on measuring dynamics in atoms and small molecules, to create the basic knowledge required for scaling the experiments towards larger molecules. In the last part of this thesis, Chapter 8, "Macro-atom vs many-electron effects in ultrafast ionization of C_{60}", a model study on complex molecules is performed by strong field ionizing C_{60} with 800 nm light at a broad range of intensities. The resulting angle and energy resolved photoelectron spectra were analyzed by a TDSE model and a statistical model. The first model shows that the C_{60} molecule can be largely regarded as a kind of super-atom with a single active electron, a surprising result for such a complicated molecule. As shown by the statistical method the influence of electron-electron correlations is limited to weakening the contrast of the observed ATI peaks.

2 Photoelectron angular distributions from the ionization of xenon Rydberg states by mid-infrared radiation

Angle-resolved photoelectron spectra, resulting from the strong field ionization of atoms or molecules, carry a rich amount of information on ionization pathways, electron dynamics and target structure. We have investigated angle resolved spectra arising from the non-resonant ionization of xenon Rydberg atoms in the multiphoton regime using strong field mid-infrared radiation, from a free electron laser. The experimental data reveal a rich oscillatory structure in the low-order above threshold ionization (ATI) region. By performing quantum mechanical and semi-classical calculations, the observed oscillations could be well reproduced and explained both by a multiphoton absorption picture as well as by a model invoking electron wave packet interferences. Furthermore, we demonstrate that the shape and orientation of the initial Rydberg state leaves its own fingerprint on the final angular distribution.

2.1 Introduction

Strong field ionization of atoms or molecules can be well characterized by measuring the ejected photoelectrons. In conventional photoelectron spectra, information on the ionization dynamics and the target structure is encoded in the form of the electron yield versus the kinetic energy. This has revealed many features of the ionization process, like its non-linear character [33], the maximum energy transfer to the electron of two times the ponderomotive energy ($2U_p$) [36], the existence of Freeman resonances [39] and many other processes. Due to the extra dimension involved, the angular dependence of the ejected photoelectrons is known to carry additional details about the ionization dynamics and the target system. Examples are the signature of the molecular orbital in the electron diffraction signal [55], the encoding of temporal and spatial information of both ion and electron, by means of photoelectron holography [56] and the influence of the Coulomb force on low energy electrons [40–43].

Depending on the ionization regime, angular structures are commonly explained in two different ways. The tunnel-ionization regime is quantified by the Keldysh parameter $\gamma = \sqrt{\mathrm{IP}/2U_p} < 1$, with ionization potential IP and ponderomotive energy (i.e. the electrons' average quiver enery) $U_p = F^2/4\omega^2$, with field

strength F and frequency ω. In this regime the field strength is strong enough to sufficiently suppress the Coulomb barrier, to provide a tunnel for the electron to escape. Simultaneously the laser frequency is low enough to provide a static barrier during tunneling. As a consequence, ionization happens mainly at the field-maxima and the dominant structures observed in the photoelectron spectra are explained as interferences between electron wave packets emitted at different times within the laser cycle [47, 49, 56, 57]. In the multiphoton ionization regime (MPI, $\gamma > 1$), either the field strength is too low to sufficiently suppress the barrier or the frequency too high, such that the electron does not get enough time to tunnel out. In this case the ionization is viewed as going "vertically", i.e. the electron absorbs a number of photons in order to exceed the ionization threshold. Structures in the photoelectron spectra are consequently described as being due to multiphoton transitions [44, 45], in which the observed dominant angular momentum is interpreted in terms of the addition of the angular momentum of the initial state and the angular momentum of each absorbed photon, according to the dipole selection rules.

An example in which the same structure is explained using these two complementary pictures is the above threshold ionization (ATI) photoelectron spectrum, which is characterized by maxima in the electron yield separated by the energy of one photon. In the multiphoton ionization domain, this structure is explained as the absorption of multiple photons above the ionization threshold. In the tunneling ionization domain it is explained as the interference of photoelectron wave packets that are ionized at field maxima separated by one laser-cycle from each other. This is an example of two coexisting explanations for the same pattern and shows that the distinction between these two regimes is not as strict as outlined above [11, 58]. It is therefore interesting to study photoelectron angular distributions from both perspectives.

In this Chapter, we have investigated the multiphoton ionization of selected Rydberg states of the xenon atom using mid-infrared radiation between 24 and 31 µm, obtained from the Free Electron Laser for IntraCavity Experiments (FELICE) [59]. The observed rich angular distributions in the photoelectron momentum spectra are analyzed using various theoretical models. First, by solving the time dependent Schrödinger equation (TDSE), where the typical imprint that different atomic orbitals and their orientations leave on the final angular distribution could be identified. Second, the oscillatory structure in the low-order ATI rings was analyzed using a biased random walk model [60, 61] and by performing strong field approximation (SFA) calculations. In the random walk model, each photon absorption leads to an altering of the angular quantum number by $\Delta\ell = \pm 1$, biased towards $\Delta\ell = +1$ [62], consistent with a multiphoton absorption picture. By performing SFA calculations we show that the same structures can be explained by photoelectron wave packet interferences and identify the origin of the nodes in the ATI rings. Upon combining experimental results with a number of theoretical models we will be able to explain the measured angular distributions by the two complementary pictures. Furthermore, it allows identifying the specific imprint an atomic orbital and its orientation leaves on the final photoelectron angular momentum spectra.

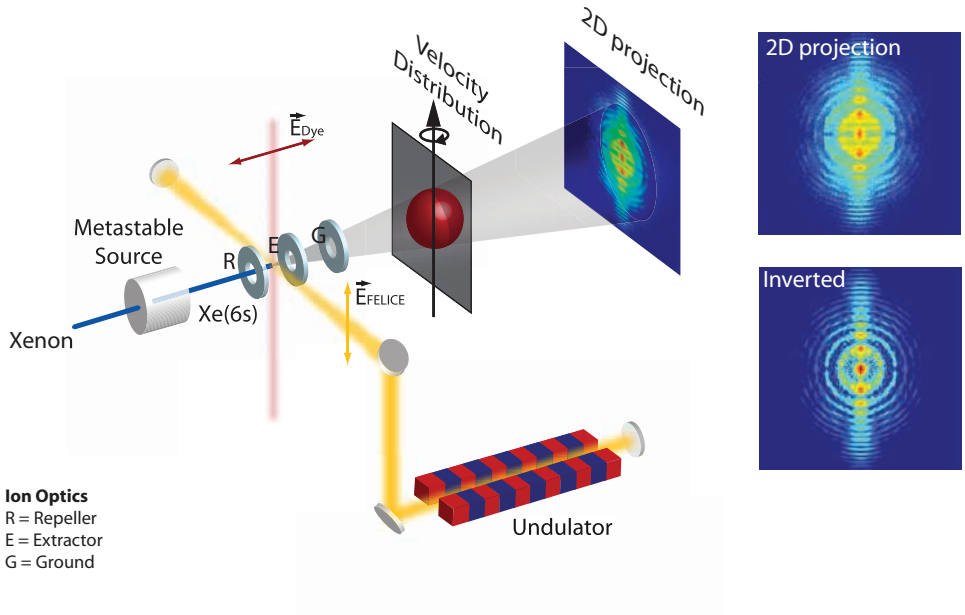

FIGURE 2.1: **Experimental setup.** Xenon was injected with a pulsed valve into the vacuum chamber. In the metastable source [63], a significant fraction was promoted to the metastable xenon $5p^5(^2P_{3/2})6s[3/2]_2$ state. In the interaction region, a tunable dye laser (in red) excited the xenon to the Rydberg states of interest. Ionization of these states proceeded by interaction with the FELICE laser (in yellow), of which more details are given in the caption of Figure 3.2. The photoelectrons were detected with a velocity map imaging (VMI) spectrometer [64], which consisted of a set of electrodes and a position sensitive detector. The electrodes, denoted by R (repeller), E (extractor)E and G (ground), act as a lens and bring all electrons with the same velocity vector to the same spot on the detector. This detector (not shown in the figure), consisted of a stack of dual micro-channel plates (MCPs), a phosphor screen and a CCD-camera. The three-dimensional velocity distribution, which was projected on the two-dimensional detector, can be retrieved by an inversion method based on an inverse Abel transformation. In this Chapter an Abel inversion routine was used that is based on a Legendre polynomial expansion, similar to the BASEX method [65]. The inversion is only possible when the geometry is cylindrical symmetric. Therefore the polarization of the FELICE laser was chosen parallel to the detector. The momentum maps studied in this thesis are slices through the three-dimensional distribution (denoted by "inverted"). To populate $|m_\ell| = 1$ states the polarization of the dye-laser was chosen to be orthogonal to the FELICE-laser polarization. Consequently, cylindrical symmetry was only achieved for fully symmetric atomic orbitals, i.e. s-orbitals. Because an inversion will not lead to the correct three-dimensional distribution for all the other cases, their two-dimensional projections will be presented. This will be mentioned in the figure captions.

2.2 Experimental setup & theoretical models

In the experimental setup (Figure 2.1) high lying xenon Rydberg states where ionized with the FELICE laser. The resulting photoelectrons were detected with

a velocity map imaging spectrometer (VMI). By using an inversion procedure, the three-dimensional velocity distributions were retrieved. The presented data are slices through this three-dimensional distribution and are referred to as momentum maps. Note that upon populating $|m_\ell| = 1$ states, or higher, the cylindrical symmetry is lost. Therefore, these data are presented by their two-dimensional projection, as explained in the figure caption.

As described above, two theoretical models were used in the analysis. In the quantum mechanical TDSE-model, the time-dependent Schrödinger equation was solved on a three-dimensional grid using the single active electron (SAE) approximation. A mixed gauge approach was used, with the length gauge close to the core and the velocity gauge far away from the core. The switching of gauges happened outside the initial Rydberg orbital. The laser pulse envelope was chosen to be a sine-squared shape. A more detailed description of this method can be found in [66–69]. To analyze electron wave packet interferences a standard SFA model [70] was used. In the SFA, an expression for the ionization amplitude is obtained by solving the time-dependent Schrödinger equation with the approximation that in the continuum the photoelectron only experiences the laser field and therefore the Coulomb force can be neglected. SFA calculations were performed using a saddle-point method in order to determine the most relevant ionization times.

2.3 Analysis of xenon 10s ionization

Figure 2.2 shows the evolution of the photoelectron angular distribution as a function of the laser wavelength, recorded after ionization of xenon atoms that were prepared in the $10s[3/2]_2$ state. The top figure of each panel shows the experimental momentum maps. As expected, the dominant ionization is along the laser polarization axis of the ionizing laser, i.e. the z-axis. Also, all of the electron momentum distributions show a clear ring structure that corresponds to ATI and which is highly structured. Upon increasing the wavelength (i.e. decreasing the photon-energy) the ATI-rings move inward. In order to decipher the observed angular distribution of the ejected photoelectrons, the experimental data are compared to focal volume averaged [71] TDSE calculations solved for a maximum value of A = 0.12 a.u. for the vector potential and a total pulse duration of 16 cycles i.e., about 6 cycles at full width half maximum (FWHM). These values of the vector potential and pulse duration provided the best agreement between calculation and experiment as shown in Figure 2.2, where the TDSE calculations are displayed in the bottom figure of each panel. The judgement was based on the comparison between the angle integrated photoelectron spectra, from which the slope of the spectra and the modulation depth in the ATI structures could be compared and by comparison of the angular distributions of the first ATI rings. The pulse duration of 6 cycles at FWHM does however not agree with the obtained values for the pulse duration in the experiment: from the acquired wavelength spectra of the FELICE pulses, a rough estimation of 1-2 ps (20 cycles) at FWHM was obtained. This discrepancy is most likely due to the fact that the FELICE micro pulses have a pulse envelope that differs substantially from a sine-squared shape as used in the TDSE calculation. Furthermore, as measured with a power meter, the micropulse

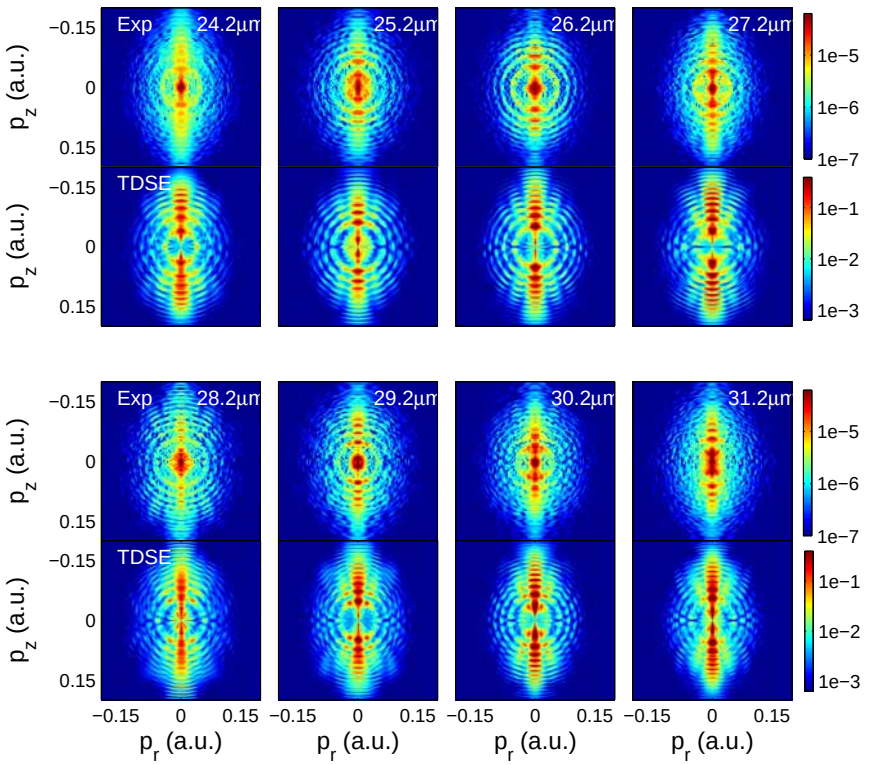

FIGURE 2.2: Electron momentum distribution recorded after ionization of xenon $10s[3/2]_2$ state as a function of FEL-wavelength. For the values of the intensity and pulse duration, the reader is referred to the discussion in the text. Each panel shows the inverted experimental data (top) and the focal volume averaged TDSE calculations with a maximum field strength of $A_{max} = 0.12$ a.u. and considering 16 full laser cycles (bottom). The laser polarization direction is along the z-axis and the values for momentum are expressed in atomic units (a.u.).

energies varied between 0.5 and 1.3 mJ, leading to values for the vector potential ranging from A = 0.4 to 1 a.u., for a beam waist at the focal spot of about 0.7 mm. This is much higher than the maximum value used in the calculation, suggesting a highly saturated ionization. This was experimentally confirmed by the fact that the spectra did not show any changes upon lowering the intensity. Saturation was also confirmed by our TDSE calculations, however, according to these calculations saturation is expected to set in only for higher values of A_{max}. The latter discrepancy could be a result of the different time structure used in the experiment and in the calculations. Despite these uncertainties, the TDSE calculations do show reasonable agreement: a dominant contribution along the laser polarization is observed together with highly structured ATI rings, for which the number of nodes usually agrees with the experimental data. The positions of the ATI peaks differ slightly (0.01 eV), due to the static electric field produced

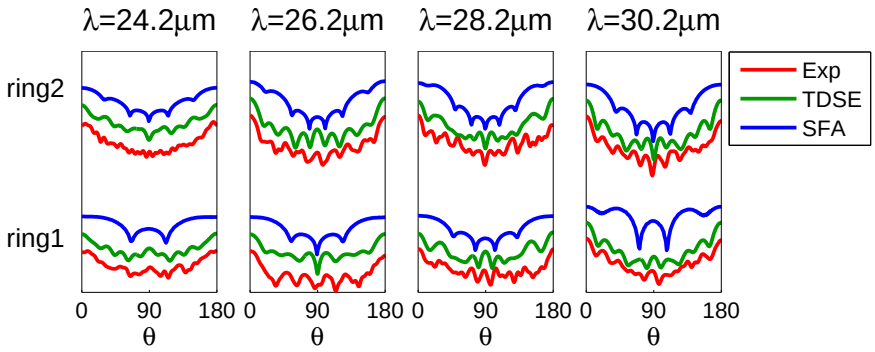

FIGURE 2.3: Angular distributions of the first and second ATI ring observed after ionization of xenon $10s[3/2]_2$ state as a function of FEL-wavelength. The presented angular distributions for the experimental data (red) and TDSE calculations (green) are derived from the momentum distributions presented in Figure 2.2. SFA calculations (blue) were performed for a single intensity of $1 \cdot 10^8$ W/cm^2, which is justified by the fact that the focal volume averaged TDSE calculations show only minor differences in the angular distribution with respect to the single intensity $1 \cdot 10^8$ W/cm^2 TDSE calculations. The y-axis represents the signal strength in arbitrary units and the different angular distributions are shifted with respect to each other for clarity.

by the VMI extraction region in the experiment. Other differences, like the higher contrast in the TDSE calculation for the ATI rings and their substructures, are mainly attributed to the different time structure of the FELICE micro pulses, as argued before.

A more detailed comparison of the angular distributions of the first and second ATI rings is given in Figure 2.3, in which experimental data, the TDSE calculations and the SFA calculations are compared. The nodal structure changes parity for each subsequent ATI ring as observed for example at 26.2 μm, where at 90 degrees there is a minimum in ring 1, and a maximum in ring 2. Though the TDSE calculations in general show sharper oscillations, the number and position of oscillations agree to a large extent. In previous experiments on multiphoton ionization with 800 nm laser light, the number of nodes in the ATI rings was directly related to the angular momentum of the ground or resonance state plus the number of photons absorbed [44, 45]. Each time a photon is absorbed, the dipole selection rules apply and a transition to a $\Delta\ell = \pm 1$ state is made, with a bias towards $\Delta\ell = +1$, which in reality is often the case, as explained by Fano [62]. If for example an electron starts out in a $\ell = 1$ state, upon absorbing three photons it can end up in a superposition of $\ell = 0, 2$ and 4. A dominance of angular momentum $\ell = 4$ will lead to 4 minima over a 180 degrees angle. This furthermore implies that a minimum or maximum (i.e. the parity) at 90 degrees indicates whether the final angular momentum is a superposition of respectively odd or even angular momenta.

Following this line of reasoning, one can apply a biased random walk model [60, 61] to predict the number of observed maxima in the angular distributions.

λ (µm)	N	Obs. L	Pred. L
24.2	8	8	8
25.2	9	7/9	7
26.2	9	7	7
27.2	9	7	7
28.2	10	6/8	8
29.2	10	8	8
30.2	10	8	8
31.2	11	9	9

TABLE 2.1: Comparison of the observed dominant angular momentum L (Obs. L) in the first ATI ring from ionization of xenon 10s with predicted angular momentum L (Pred. L) by the biased random walk model with a chance for an electron to go to $\Delta\ell = -1$ versus $\Delta\ell = +1$ of 0.115:0.885. N in the table represents the number of photons that leads to the first ATI ring.

Chen *et al.* [61] and Arbó *et al.* [60] obtained a good fit to their low energy electron angular distribution using a ratio of 0.3325:0.6675 for transitions $\Delta\ell = -1$ and $\Delta\ell = +1$, respectively. We applied the model in the same manner as Chen *et al.*. The observed angular momentum was retrieved from the angular distributions by counting the number of minima over 180 degrees (see Table 2.1). Perfect agreement is achieved for a ratio of 0.115:0.885 for $\Delta\ell = -1 : \Delta\ell = +1$, with an error of ± 0.005. There is no reason to assume that the obtained ratio should match the one obtained by Chen *et al.* and Arbó *et al.*, since the bias depends, in a non-trivial way, on the quantum numbers n and ℓ [72], which are very different in our case.

So far, we have explained the angular distribution of the ejected photoelectron using a multiphoton picture, with the number of nodes related to the angular momentum quanta $\Delta\ell = \pm 1$ transmitted each time a photon is absorbed. A similar nodal structure in the angular distributions can be obtained using a wave packet interference picture. This is demonstrated in Figure 2.4a which shows the result of an SFA calculation for the ionization of the xenon 10s state with 29 µm light and an intensity of $1 \cdot 10^8$ W/cm^2. The calculation was done for a three and a half cycle laser pulse with half cycle turn on and turn off. A nodal structure in each ATI ring is observed, with alternating parity for each subsequent ATI ring. This agrees with what was found in the experimental data and TDSE calculations shown in Figure 2.2 and 2.3, and with what was predicted by the random walk model (Table 2.1). As described above, the ATI structure can be explained as an interference of trajectories ionized at subsequent maxima of the laser field, separated by a full laser cycle. The trajectories they follow are identical, but the first ionized electron feels one more oscillation. This interpretation of the ATI structure is confirmed by the calculation shown in Figure 2.4b, in which only trajectories from the first half and the third half cycle are included. The interference between these two electron wave packets indeed leads to an ATI structure. We have verified that the addition of trajectories from the second and fourth maxima also leads to an ATI pattern. The rings that characterize the ATI pattern are however structureless (Figure 2.4b). The nodal structure comes from a different type of wave packet

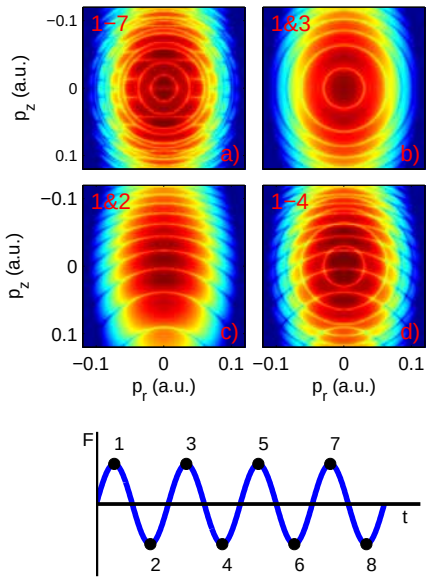

FIGURE 2.4: SFA calculations on ionization of xenon 10s with $\lambda = 29$ µm and $I = 1 \cdot 10^8$ W/cm^2. The flat top pulse is shown in the lower panel and consists of 3.5 cycles. The electron momentum distribution is obtained for a) a 3.5 cycle flat top laser pulse, b) interference between trajectories from the first and third half-cycle of the laser pulse, c) interference between trajectories from the first and second half-cycle of the laser pulse d) interference of all trajectories during the first two laser cycles.

interference, namely the interference of wave packets ionized at the opposite maxima of the laser field during the same cycle. This is demonstrated by Figure 2.4c where the trajectories from the first and second field maxima are added. That this interference is responsible for the nodal structure in the ATI pattern becomes even clearer in Figure 2.4d where all trajectories from two laser cycles are added. This is the minimum number of trajectories for the ATI with nodal structure to appear.

A detailed comparison of the SFA with the TDSE calculations and the experimental data is shown in Figure 2.3. Though the parity is always correct, the number of nodes is generally underestimated in SFA. This underestimation has been investigated in reference [61], where it is shown that upon removing the long range Coulomb tail in TDSE, the nodal structure of the TDSE calculation is identical to the SFA structure, implying that the long range Coulomb force is crucial in determining the correct number of nodes.

The foregoing discussion demonstrates that the observed structures in low-order ATI patterns can be explained by a multiphoton absorption process as well as by wave packet interferences. For the latter the long range Coulomb force is crucial for a correct prediction of the number of nodes. This is similar to the fact that in the multiphoton absorption process a bias towards $\Delta\ell = +1$, which

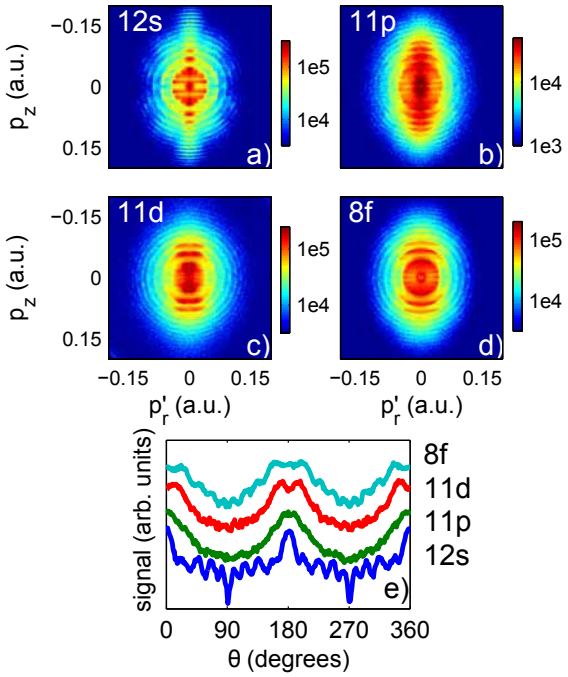

FIGURE 2.5: a-d) non-inverted electron momentum distributions from the ionization of the $12s[3/2]_2$, $11p[3/2]_2$, $11d[7/2]_4$ and $8f[3/2]_2$ Rydberg states with $\lambda = 31.2$ µm. For the values of the intensity and pulse duration, the reader is referred to the discussion in the text. e) angular distributions of the first ATI ring. Because there is no cylindrical symmetry, the momentum maps are not inverted. Due to this, the horizontal axis corresponds to the momentum in the detection plane perpendicular to the laser polarization axis. This momentum is labeled p'_r, and is distinct from the actual momentum perpendicular to the laser polarization axis p_r

depends on the Coulomb potential, is essential.

2.4 Analysis of xenon s, p, d and f state ionization

In our experiment, we have also investigated the influence of different initial atomic orbitals and their orientations on the final photoelectron angular distribution. In Figure 2.5 the electron momentum distributions from the ionization of xenon s, p, d and f-states are compared. A progressive widening of the central lobe (along the laser polarization) is observed. For the s-state, a narrow contribution is observed along the laser polarization, i.e. at 180 degrees. For the p-state this contribution is wider and a very small dip appears. For the d-state, one can clearly distinguished a very prominent dip along the laser polarization and for the f-state an extra oscillation appears within this dip. In our experiment we have observed that this behavior is general for s, p, d and f-states.

To investigate this observation in more detail, we focus on the $11p[3/2]_2$ state.

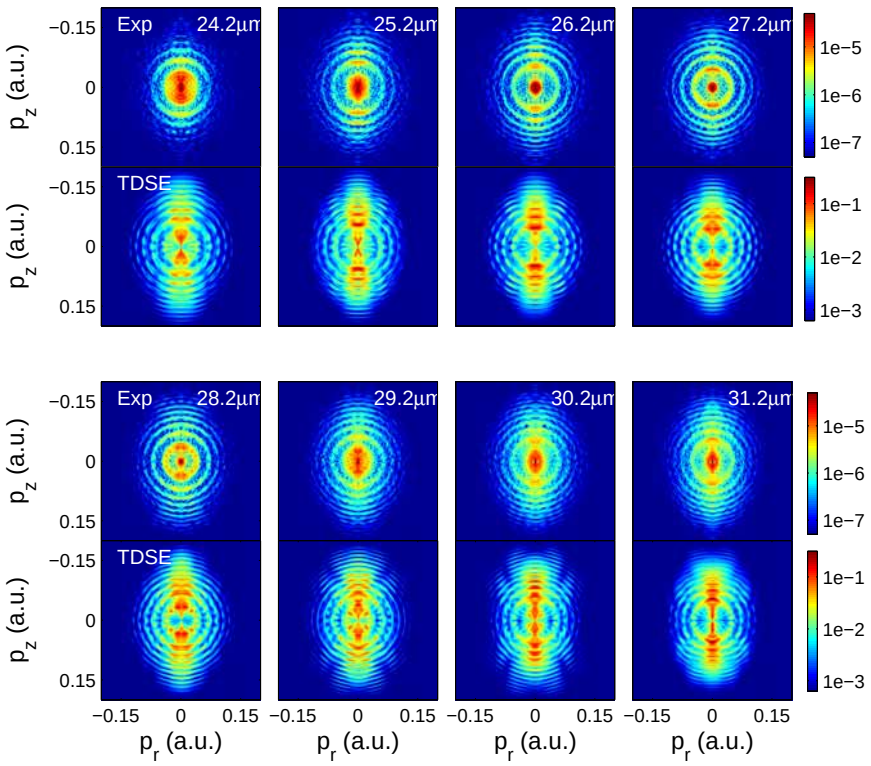

FIGURE 2.6: Momentum maps resulting from the ionization of xenon $11p[3/2]_2$ state as a function of FEL-wavelength. The top rows in each panel are the inverted experimental data and bottom parts the focal volume averaged TDSE calculations with a maximum field strength of $A_{max} = 0.10$ a.u., a pulse duration of 16 full laser cycles and a mixture of $m_\ell = 0$ vs $|m_\ell| = 1$ of 1/3 to 2/3. The laser polarization direction is along the z-axis.

In Figure 2.6 the angular resolved photoelectron signal resulting from the ionization of the xenon 11p state is shown as a function of wavelength. Since the laser polarization of the dye laser and the FELICE laser are orthogonal to each other, we expect to populate only the $|m_\ell| = 1$ state [73]. However, for a reasonable comparison between the experiment and the TDSE-calculations it is necessary that we use a superposition of $m_\ell = 0$ and $|m_\ell| = 1$ states with a statistical distribution over $m_\ell = 0$ and $|m_\ell| = 1$ of 1/3 and 2/3, respectively. A possible explanation for this necessity is the presence of a magnetic field, leading to a Zeeman splitting of the m_ℓ-states. In our experimental setup, a large magnetic field in the vicinity of the interaction region is produced by the coil of the metastable source. Even though the interaction region is shielded with a µ-metal tube, it is expected to not perfectly screen the magnetic field, especially not since there is a substantial hole in the µ-metal to let the gas atoms into the chamber. An induced Zeeman splitting will lift the degeneracy between the m_ℓ-states, and induce wave packet motion between the various m_ℓ-states, with an oscillation period proportional to

the inverse of the energy splitting, $\sim 1/E$. Since the electronic state is coupled to the core state of xenon in a jK coupling scheme, m_J is the good quantum number and the projection of m_J on m_ℓ will lead to a population of the $m_\ell = 0$ state. If the interaction region had not been shielded, the residual magnetic field at the interaction region would have been about $2.3 \cdot 10^{-4} T$, leading to a very small energy splitting of about $2.7 \cdot 10^{-8} eV$ and a corresponding oscillation period on the order of tens of nanoseconds. If due to the shielding only 1% of the magnetic field would have penetrated, the oscillation period is still on the order of a few µs, comparable to the time delay between the dye laser and the FELICE macro pulse, which was a few µs. This is enough to create a mixture of $m_\ell = 0$ and $|m_\ell| = 1$ states.

Using a statistical mixture of m_ℓ states, the TDSE calculations and the experimental data show a similar widening of the central lobe and highly structured ATI rings with the correct parity for most of the cases. The observed deviations are again attributed to a different time structure in the experiment and calculations, but also to the unknown superposition in $m_\ell = 0$ and $|m_\ell| = 1$ states. In the experimental data a smooth angular distribution in the ATI rings is observed for a wavelength of 24.2 µm, which is accompanied by the appearance of a set of rings within the first ATI ring. Upon ionizing rare gas atoms from their ground state, similar substructures have also been observed [44–46]. They are formed when the ionization passes through a set of high lying resonant states, called Freeman resonances [39]. The fact that in our experiment the possible resonant states lie extremely close to the ionization threshold implies that these are strongly coupled to the laser field. As such it is doubtful whether they can still be regarded as individual states, through which a resonance could pass. Furthermore the orbital periods of these states ($T = 2\pi n^3$, in a.u, with $n \sim 20$) are on the same order of the pulse duration, i.e. picoseconds. Further investigations are underway in order to understand this special and unresolved phenomenon for low energy electrons.

With the TDSE calculations, it is possible to disentangle the contributions from the $m_\ell = 0$ and $|m_\ell| = 1$ state, as shown in Figure 2.7. In Figure 2.7a and 2.7b, TDSE calculations for respectively $m_\ell = 0$ and $|m_\ell| = 1$ are shown for $\lambda = 26$ µm and $\mathrm{I} = 1 \cdot 10^8$ W/cm^2. Two major differences are observed. First, the contribution along the laser polarization axis shows a dip for $|m_\ell| = 1$, which explains the observed small dip in the main-lobe of the measured 11p state. The TDSE calculations show that without contribution from $m_\ell = 0$ this dip would even have been larger. The origin of this dip can be explained in two ways and is found in the orientation of the atomic orbitals. For $\ell = 1$, $|m_\ell| = 1$ the orientation of the atomic orbital is such that there is no contribution along the laser polarization axis, as shown in the cartoon in Figure 2.7. Since the quantum number m_ℓ is conserved in the ionization, no photoelectron signal is expected along the z-axis. The same feature can also be explained by the fact that the ionization from the positive and negative halves of the orbital (Cartoon Figure 2.7) destructively interfere along the z-axis. According to the TDSE calculations, a wider region along the laser polarization is suppressed for the $|m_\ell| = 2$ projection of the d-orbital, explaining its even larger dip as observed in Figure 2.5. The second observation is that the nodal structures of the ATI-rings have opposite parity for $m_\ell = 0$ and $|m_\ell| = 1$. According to the Cartoon in Figure 2.7, the $m_\ell = 0$ orbital is aligned along the laser polarization and consequently has an electron distribution with

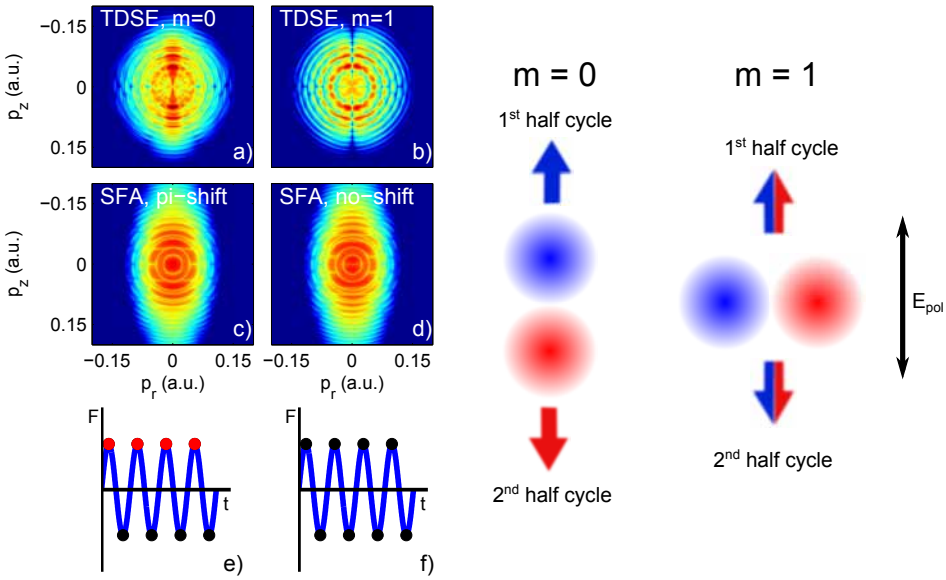

FIGURE 2.7: Momentum maps of photoelectrons from the ionization of 11p with 26 µm radiation and an intensity of $1 \cdot 10^8$ W/cm^2. a) TDSE calculation for $m_\ell = 0$ b) TDSE calculation for $|m_{ell}| = 1$ c) SFA calculation with a π-shift for each positive laser field maximum d) SFA calculation without π-shift. In figures e) and f) the laser field F is plotted in which the π-shifted trajectories are marked by red dots and normal trajectories by black dots. Cartoon: illustration of π-orbitals with $m_\ell = 0$ and $m_\ell = 1$ orientation. The color indicates the phase, where red and blue have opposite phases. The arrows indicate the ionization direction.

opposite parity along the laser polarization. This induces a π-shift between the phase of the electron wave packets that are ionized in opposite directions along the laser polarization during successive half-cycles, as indicated by the blue and red arrows. Due to the different orientation of the $|m_\ell| = 1$ orbital, no asymmetry in the laser polarization direction is present and the π-shift is absent. The π-shift in the $m_\ell = 0$ case leads to an opposite parity with respect to the $|m_\ell| = 1$ case.

Next we analyze the observed angular distribution by applying the random walk model discussed earlier (Table 2.2). Since the random walk model does not include the m_ℓ quantum number, a comparison can only be made to TDSE calculations for $m_\ell = 0$ states. Upon using the same ratio for the $\Delta\ell = -1$ and $\Delta\ell = +1$ transitions, as used for the xenon 10s state, the predicted and observed angular momentum usually agree, except for a wavelength of 31.2 µm. In the table, the angular momentum for the $|m_\ell| = 1$ states are also given. They were obtained from counting the minima in the angular distribution as given by the TDSE calculations. As outlined above, the parity for $|m_\ell| = 1$ is always opposite to $m_\ell = 0$ and more specifically the angular momentum always differs by one.

One can also explain the oscillations in the angular distribution of the ATI

λ (µm)	N	Obs. L (m=0)	Obs. L (m=1)	Pred. L
24.2	5	6/8	7	6
25.2	6	7	8	7
26.2	6	7	6	7
27.2	6	7/9	6	7
28.2	6	7	6	7
29.2	6	7	6	7
30.2	7	8	7	6/8
31.2	7	10	7	6/8

TABLE 2.2: Comparison of the observed dominant angular momentum L (Obs. L) in the first ATI ring from ionization of xenon 11p with predicted angular momentum L (Pred. L) by the biased random walk model with a ratio of the chance for an electron to go to $\Delta\ell = -1$ versus $\Delta\ell = +1$ of 0.12:0.88. N in the table represents the number of photons needed to arrive at the first ATI ring.

rings by wave packet interferences. SFA calculations were performed and compared to TDSE calculations. In Figure 2.7 the result is shown for an ionization potential corresponding to 11p, $\lambda = 26$ µm and an intensity of $I = 1 \cdot 10^8$ W/cm^2. Since the atomic orbital's structure is not included in the SFA-calculation no distinction can be made between $m_\ell = 0$ and $|m_\ell| = 1$. The above given explanation for the observed difference in parity for $m_\ell = 0$ and $|m_\ell| = 1$ implies that the parity of the SFA calculation should match the $|m_\ell| = 1$ parity, because in this case all the trajectories are emitted with the same phase. Indeed, the parity of the nodal structures in the ATI ring for the SFA-momentum map corresponds to the parity of the $|m_\ell| = 1$ state of the TDSE-momentum map (Figure 2.7d). The $m_\ell = 0$ states can be mimicked upon introducing a π-shift for all trajectories emitted in opposite directions, as indicated in Figure 2.7f, where all ionization times for π-shifted trajectories are marked with a red dot. The result is shown in Figure 2.7c and indeed it matches the TDSE $m_\ell = 0$ case.

2.5 Conclusion

We have measured angle-resolved photoelectron spectra for the ionization of selected xenon Rydberg states in the multiphoton ionization regime. The data show highly structured photoelectron angular distributions. The TDSE calculations show similar patterns with in general a higher contrast, which is attributed to a different pulse structure in the experiment. We have successfully explained the observed nodal structures by two complementary view points: by explaining the observed structure in the frequency domain (i.e. by multiphoton absorption) and by explaining them in the time domain (i.e. by electron wave packet interferences). For this, respectively, a random walk model was and an SFA method was applied. For the correct prediction of the number of maxima a bias is required in the random walk model. When analyzing the structures as wave packet interferences, the inclusion of the long range Coulomb force is essential. The SFA method also allowed us to identify that the interference responsible for the nodal structure

in the ATI rings is caused by trajectories that are ionized at opposite maxima of the laser field. Upon selecting specific Rydberg states in the experiment we have furthermore shown that the atomic orbital and its orientation leave a specific imprint on the final photoelectron angular distribution. TDSE calculations gave further insight into the origin of the different imprints. All in all we can conclude that photoelectron spectra carry a rich amount of information on the ionization process and the target structure. This information can be retrieved by applying either a frequency or time domain explanation, which are complementary explanations that are not restricted to either the tunneling regime or the multiphoton regime.

3 Time-resolved holography with photoelectrons

Ionization is the dominant response of atoms and molecules to intense laser fields and is at the basis of several important techniques, such as the generation of attosecond pulses that allow the measurement of electron motion in real time. We present experiments where metastable xenon atoms are ionized by intense 7-micrometer laser pulses from a free-electron laser. Holographic structures are observed that record underlying electron dynamics on a sublaser-cycle time scale, enabling photoelectron spectroscopy with a time resolution almost two orders of magnitude higher than the duration of the ionizing pulse.

3.1 Introduction

After a strong laser field ionizes an atom or molecule, the liberated electron is accelerated by the oscillatory laser electric field and driven back towards the ion [3]. Electron-ion re-collision leads to the emission of XUV radiation with a duration that approaches the atomic unit of time (24.2 as) [74, 75], and encodes detailed structural and dynamical information about the atomic or molecular medium used [15–17, 76]. Alternatively, the returning electron may elastically or inelastically scatter [52, 55]. These processes benefit from the 10^{11} A/cm^2 electron re-collision current incident on the target ion, exceeding current densities used in transmission electron microscopes [54]. The laser-driven electron motion is fully coherent, allowing to put into practice the concept of holography [31], and to extend it to electron-ion collisions involving laser-ionized and -driven photoelectrons [52, 77, 78]. We demonstrate how under suitably chosen experimental conditions a hologram can be recorded that encodes temporal and spatial information both about the ion (the "target") and the re-collision electron (the "source"), opening the way to a new type of ultrafast photoelectron spectroscopy of electron and nuclear dynamics in molecules.

3.2 Concept of photoelectron holography

Key to holographic electron imaging is the observation of an interference pattern between a reference wave, which is emitted from the source and does not interact

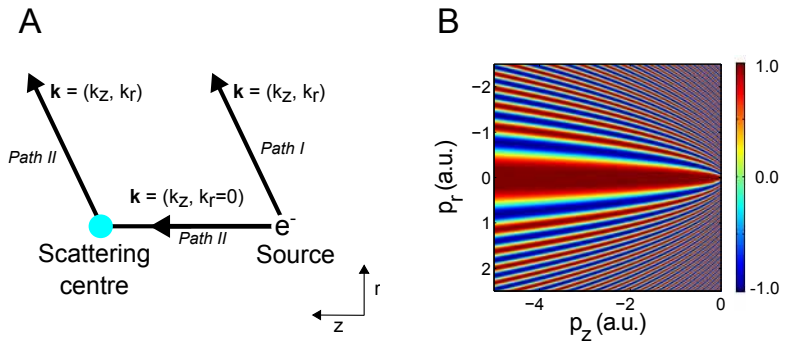

FIGURE 3.1: (A) **Diagram illustrating the concept of electron holography.** Two interfering paths with the same final momentum $\mathbf{k} = (k_z,k_r)$ are indicated. Path I is a reference wave, leaving the source with momentum $\mathbf{k} = (k_z, k_r)$. Path II is a signal wave, incident on the target with $k_r = 0$, $k_z = k = |\mathbf{k}|$ and scattering into $\mathbf{k} = (k_z, k_r)$. The phase difference $\Delta\varphi = (k - k_z)z_0$ that follows from the path length differences leads to interference fringes $\sim cos[(k - k_z)z_0]$ (B) Interference pattern generated by a Gaussian wave packet released at a distance $z_0 = 50$ atomic units (a.u.) from a scattering center, with no laser field present. A hologram is created as a result of interference between a scattering-signal wave packet and a direct-reference wave packet.

with the target, and a signal wave, which scatters off the target and encodes its structure. The encoded information is stored when the signal wave interferes with the reference wave on a detector. A simple analysis borrowed from ray optics (Figure 3.1A), shows that because of path length differences a phase difference $\Delta\varphi = (k - k_z)z_0$ (where k is the total momentum, k_z is the momentum in the z direction and z_0 is the distance to the scattering centre) arises between the reference and scattered waves, resulting in the pattern shown in Figure 3.1B.

To record a clear holographic picture it is desirable that the reference wave is not influenced by the positively charged target and, therefore, that the electron source is located at some distance from the target, z_0. A suitable way to accomplish this is tunnel ionization in a strong low-frequency laser field, in which the electron tunnels through a barrier created by the laser field and appears at some distance from the ion. In the presence of the laser field the electronic wave function can be written as

$$\psi = \psi_{signal} + \psi_{ref} \tag{3.1}$$

where ψ_{signal} represents a signal wave packet that oscillates in the laser field and scatters off the target and ψ_{ref} represents a reference wave packet, which only experiences the laser field and does not interact with the target, as explained in detail in Chapter 4. To calculate the interference pattern produced by these two terms, we used an extension of the strong field approximation (SFA), which includes the laser field fully and the electron-ion scattering in the first Born approximation

[79, 80]. The result of the calculation is shown in Figure 4.2A and predicts that in a strong laser field, the holographic fringes remain visible and that the phase difference between the signal and the reference wave packets is

$$\Delta\varphi \approx p_r^2(t_C - t_0^{ref})/2 \tag{3.2}$$

Here p_r is the momentum perpendicular to the laser polarization axis, t_C the time when the signal wave packet scatters off the ion, and t_0^{ref} the moment of birth of the reference wave packet. Thus, the hologram can be viewed as a pump-probe experiment on the fs to sub-fs timescale (see Figure 4.2B,C), which can encode changes in the scattering potential between t_0^{ref} and t_C, as well as changes in the ionization rate between t_0^{ref} and t_0^{signal}, which is the time-of-birth of the signal wave packet (see Chapter 4). The signal and reference wave packets that produce the holographic pattern originate from the same quarter cycle; thus, sub-cycle time resolution is encoded even when long pulses are used.

A crucial aspect in our holographic imaging approach is the existence of a large electron oscillation amplitude $\alpha \gg 1$Å and a large average oscillation energy $U_p \gg \hbar\omega_{\text{laser}}$, where ω_{laser} is the laser frequency and $\hbar$ is Planck's constant h devided by 2π. In experiments with 800 nm radiation these requirements lead to high laser intensities ($I \sim 10^{14}$ W/cm^2) that can only be applied to ground-state atoms and molecules with a large ionization potential. To make re-collision based imaging possible at lower intensities, the laser wavelength λ_{laser} must be increased because both α and U_p scale as λ_{laser}^2.

3.3 Experimental demonstration

To demonstrate the strong field electron holography experimentally, metastable (6s) xenon atoms were ionized by 7 µm mid-infrared (mid-IR) radiation from the FELICE (Free Electron Laser for Intra-Cavity Experiments) beamline at the FELIX facility [59] as shown in Figure 3.2. The use of a large λ_{laser} in combination with a modest ionization potential (IP = 3.8 eV) allowed the preparation of electron wave packets born at large $z_0 = \text{IP}/F_{\text{laser}}$, where F_{laser} is the laser field strength, displaying a large excursion α_0, without the need for a very high laser intensity ($7 \cdot 10^{11}$ W/cm^2), and remaining in the tunneling regime [$\gamma = (\frac{\omega_{\text{laser}}}{F_{\text{laser}}})\sqrt{2\text{IP}} < 1$]. Angle-resolved photoelectron spectra were recorded with a velocity map imaging spectrometer (VMI) [64] integrated into the FELICE laser cavity. The metastable xenon atoms were exposed to a train of 5000 mid-IR laser pulses separated by 1 ns.

Varying the position of the experimental apparatus along the laser propagation axis allowed the peak intensity to be tuned by approximately a factor five. Figure 3.3, A to F, shows a dominant electron emission along the laser polarization axis, with a high-energy cutoff (Figure 3.3G) that agrees well with the classical expectation $E_{\text{cutoff}} = F_{\text{laser}}^2/2\omega_{\text{laser}}^2$. In Figure 3.4A, side-lobes are observed that extend from low to high momentum and run parallel to the laser polarization axis for high momenta, as indicated by the black dashed lines. These side-lobes qualitatively agree with the patterns calculated in Figure 4.2a and result from a

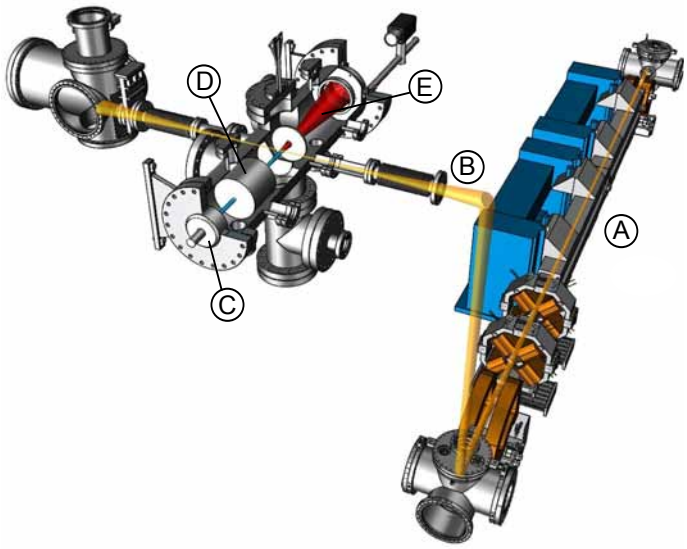

FIGURE 3.2: **Overview of the experimental setup.** A velocity map imaging (VMI) spectrometer [64] was integrated in the Free Electron Laser for Intra-Cavity Experiments (FELICE) at the FELIX facility in the Netherlands [59]. Xenon atoms were injected into the vacuum using a pulsed gas nozzle and excited to the $6s[^2P_{3/2}]_{J=2}$ metastable state by means of electron impact. After transport to the center of the velocity map imaging spectrometer, they were exposed to the FELICE laser. The FELICE radiation consists of an approximately 5 µs long macro-pulse that contains micro-pulses with a repetition rate of 16 MHz or 1 GHz; the latter has been used here. The wavelength of the radiation is tunable between 4 and 100 µm. The pulse duration of the FELICE laser is variable and has for these experiments been estimated to be about 15 optical cycles long. The Rayleigh range of the intra-cavity focus is 55 mm, resulting in a maximal power density of $3 \cdot 10^{13}/\lambda^2$ W/cm^2 with the wavelength λ given in μm [59]. For the central wavelength used in these experiments, 7 µm, this gives an approximate focused intensity of $6 \cdot 10^{11}$ W/cm^2.
Electrons that were formed by strong-field ionization were accelerated perpendicularly to the FELICE laser polarization towards a two-dimensional position-sensitive detector, consisting of a dual microchannel plate (MCP) detector, followed by a phosphor screen and a CCD camera system. 3D velocity and angular distributions were extracted from the measured data using an iterative procedure [81].
Description of labeled components: (A) the accelerator and undulator of the FEL where the infrared radiation was generated; (B) upper arm of the FEL cavity, which is built up from 4 mirrors, two of which are on either side of the undulator and two of which are (one floor higher) in the experimental hall, producing a focus in between; (C) pulsed gas valve used for injecting the xenon atoms into the instrument; (D) electron impact assembly that promoted the xenon atoms to a metastable state; (E) VMI spectrometer where electrons produced by the ionization of metastable atoms by the FEL were detected.

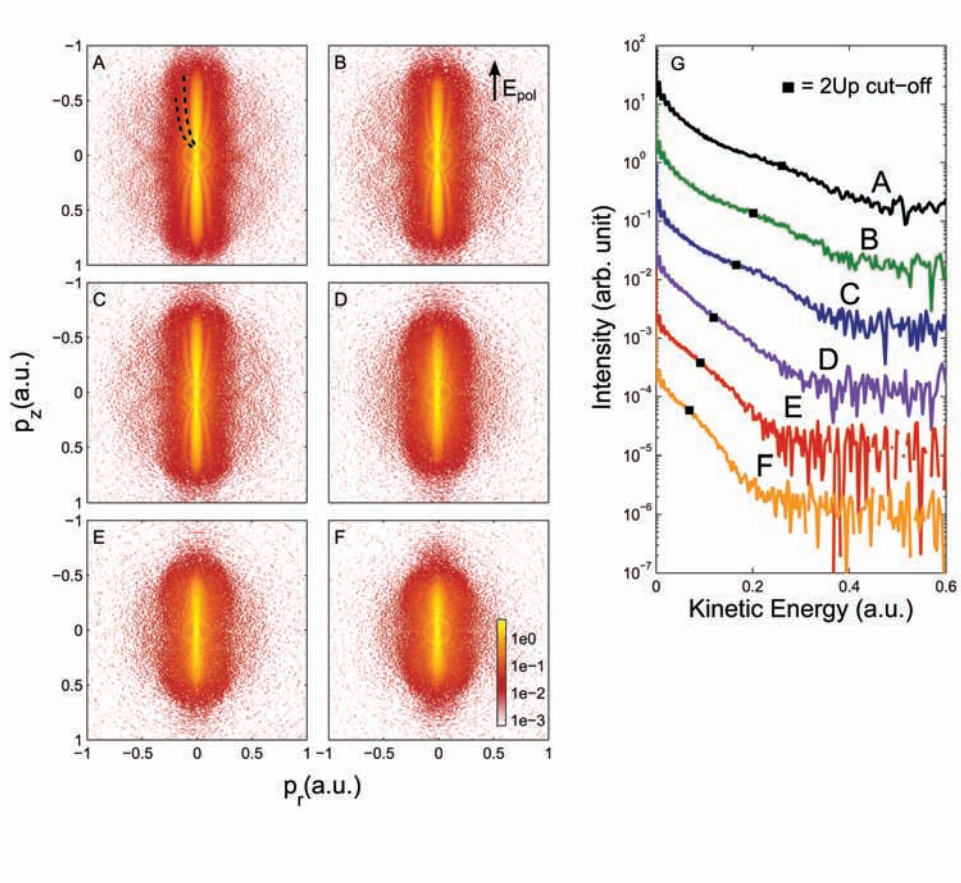

FIGURE 3.3: Intensity dependence of measured velocity map images and the corresponding photoelectron kinetic energy distributions. (A) $7.1 \cdot 10^{11}$ W/cm^2; (B) $5.5 \cdot 10^{11}$ W/cm^2; (C) $4.5 \cdot 10^{11}$ W/cm^2; (D) $3.2 \cdot 10^{11}$ W/cm^2; (E) $2.5 \cdot 10^{11}$ W/cm^2 and (F) $1.9 \cdot 10^{11}$ W/cm^2. (G) Angle-integrated photoelectron spectra. Squares indicate the energy that corresponds to the classical $2U_p$ cutoff energy.

holographic interference. Additionally, a number of weaker transverse structures extend sideways approximately orthogonal to the laser polarization, as indicated by the black dotted lines. Neither of these structures should be confused with the so-called "side-lobes", "wings" or "rings" caused by backscattered electrons that were observed in higher-order above-threshold ionization [82, 83], nor are they related to the interferences observed in recent experiments on ionization of helium by a few-cycle pulse [50].

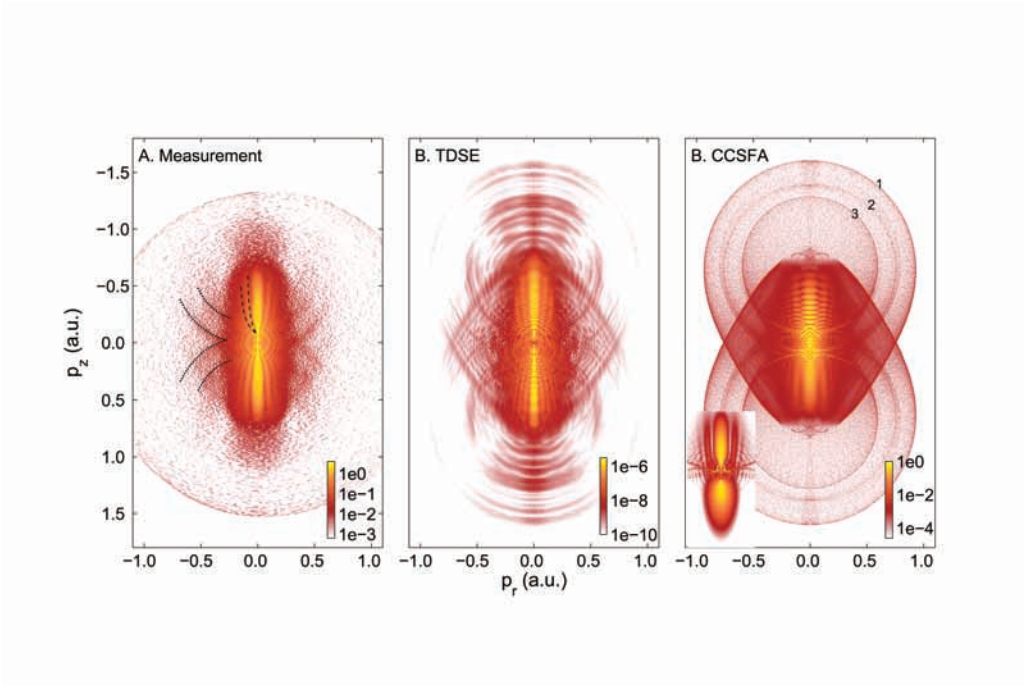

FIGURE 3.4: Comparison of an experimental two-dimensional photoelectron velocity map image with calculations (CCSFA and TDSE) (A) Four-hour-long measurement of the ionization of metastable xenon under conditions similar to those used in the measurements shown in Figure 3.3A. (B) TDSE calculation for ionization of argon (5s) (IP = 0.14 a.u., four-cycle flat-top 7 µm pulse, peak field strength of 0.0045 a.u.). (C) CCSFA calculation for ionization of a model hydrogenic atom (IP = 0.14 a.u., λ_{laser} = 7 µm, peak field strength of 0.0045 a.u.). Inset: CCSFA single half-cycle calculation, illustrating that the side-lobes are due to an interference between two trajectories that leave the atom within the same half-cycle.

3.4 Comparison to numerical models

The experimental observation of holographic interferences is confirmed through full time-dependent Schrödinger equation (TDSE) calculations, which show the same side-lobes (Figure 3.4B) [84]. The fringe spacing of these side-lobes agrees with the experiment and is reduced compared to the SFA-based calculation (Figure 4.2A), in which the long-range Coulomb potential was neglected.

Insight into the role of the Coulomb potential is gained by performing semiclassical calculations with the Coulomb-corrected strong-field approximation (CCSFA), on which more details are given in Chapter 4 and in reference [85]. In these calculations, complex quantum trajectories are calculated that, after tunneling, include the Coulomb interaction of the electron in the classically allowed region. The spectrum is calculated by summing contributions from different trajectories including their phases (Chapter 4). The results (Figure 3.4C) quantitatively reproduce the main features discussed above. Inspection of the trajectories responsible for the

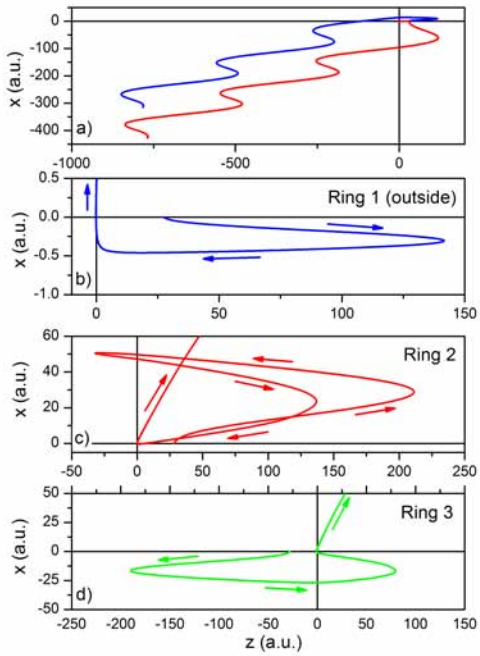

FIGURE 3.5: (A) Two trajectories that lead to the formation of electrons with a final momentum p_r = -0.01 a.u., p_z = -0.46 a.u. The red trajectory corresponds to an electron that only weakly interacts with the ionic core. The blue trajectory corresponds to an electron that strongly interacts with the ionic core and that undergoes Coulomb focusing. (B to D) Recollision trajectories, illustrating the occurrence of a recollision at the first (ring 1), second (ring 3) or third (ring 2) opportunity. The highest kinetic energy of electrons on ring 1 is 1.289 a.u. (10.75 U_p).

side-lobes shows that these trajectories can indeed be considered as a reference and scattered wave packet, creating a hologram (Figure 3.5A).

The efficiency of electron-ion recollision drops dramatically with increasing λ_{laser}, because of spreading of the wave packet between ionization and recollision. Still, a clear hologram can be observed at 7 µm. Two effects make this possible. First, the hologram results from a heterodyne experiment, where a weaker signal is mixed with a stronger signal. Second, to create a clear reference a large impact parameter is needed to limit the interaction with the Coulomb field. For large λ_{laser} a small p_r already leads to large-impact parameters due to the long excursion time between ionization and re-collision.

Inspection of the electron trajectories contributing to the transverse structures (Figure 3.4) reveals that they are due to recollision events where the scattering does not occur on the first opportunity, but on the second or third [83, 86, 87]. Typical examples of these trajectories are shown in Figure 3.5, B to D. One, respectively two glancing electron-ion collisions can be observed before the real recollision takes place. Usually these rare events do not leave an imprint on the

photoelectron spectrum. However, the combination of a long laser wavelength and Coulomb focusing [86] increases the probability because a small deviation introduced by the Coulomb potential can be sufficient to focus the returning wave packet onto the ion.

3.5 Conclusions

In our model study on the ionization of metastable xenon, we have experimentally shown the possibility to record holographic structures. Furthermore, our theoretical exploration shows that the hologram stores spatial and temporal information about the core- and electron dynamics. This offers opportunities to extend strong field holography to more complicated systems and to use it to time-resolve electron-dynamics. As revealed in recent experiments [17, 88], electron-ion recollision phenomena encode hole dynamics that occurs in ions during the first few femtoseconds after strong-field ionization. When properly implemented with the use of a long wavelength driving laser, photoelectron holography appears especially well suited for studying this type of dynamics, in particular in molecules with a low binding energy that cannot easily be studied by other means.

4 Strong field approximation theories for time-resolved photoelectron holography

In this Chapter a detailed description is given of the two semiclassical models that were used to interpret the strong field photoelectron holography pattern as described in Chapter 3. Both the generalized strong field approximation (gSFA) model and the coulomb corrected strong field approximation (CCSFA) model are based on the plain strong field approximation (SFA). In this method an expression for the ionization amplitude is obtained by solving the time-dependent Schrödinger equation with the approximation that in the continuum the photoelectron only experiences the laser field and that therefore the Coulomb force can be neglected. Scattering is however crucial in strong field photoelectron holography, therefore both models include the interaction with the Coulomb force. The gSFA model does this by including the electron-ion scattering in the first Born approximation, i.e. only elastic scattering is included. This model provides good qualitative agreement with the experimental data. Furthermore with this method it can be analytically demonstrated that time-information is stored in the hologram with sub-attosecond resolution for wavelengths of a few µm. The CCSFA model includes also the long range Coulomb force and gives quantitative agreement with the experimental data. Since it is a trajectory based calculation (once in the continuum, the path-integrals of the photoelectron describe their trajectories), it is possible to verify which types of trajectories lead to holographic pattern and which lead to the recollisions rings, of which the onset is observed in the experimental data, as described in Chapter 3.

4.1 gSFA approximation

4.1.1 General idea

A hologram is an interference pattern between two coherent beams of light or electrons that follow a different path; a direct beam that goes straight to a detector and an indirect beam that scatters off an object before going to the detector. In the hologram the shape of the object is encoded. In the previous Chapter (Chapter 3) "strong field photoelectron holography" is described, in which the coherent electron source is created at some distance away from the ion by tunnel-ionization

in the oscillating electric field of a laser pulse. After ionization the electron wave packet oscillates in the laser field and can be driven back to the ion and scatter off before it goes to the detector. It can also go to the detector directly. The interference of these two electron wave packets forms a hologram that stores both the spatial information about the core and time information on the dynamics of both the electrons and the core.

The ability to split the electron wave-function into reference and signal waves is at the heart of strong field electron holography (see also equation (3.1)):

$$\psi = \psi_{\text{signal}} + \psi_{\text{ref}} \tag{4.1}$$

The signal wave packet represents the part that scatters off the ion. The reference wave packet represents the part that goes directly to the detector. Let us identify these terms in the exact solution of the time-dependent Schrödinger equation (TDSE). The full equation for the exact wave-function that satisfies the TDSE reads [89]:

$$\begin{aligned} \psi \quad = \quad & -\int_0^t dt_0 \int_{t_0}^t dt_C U_V(t,t_C) V_C(t_C) U(t_C,t_0) V_L(t_0) U_0(t_0,0)\psi(0) \\ & -i\int_0^t dt_0 U_V(t,t_0) V_L(t_0) U_0(t_0,0)\psi(0) + U_0(t,0)\psi(0) \end{aligned} \tag{4.2}$$

The first term represents the signal wave packet that stays in the bound state until t_0, evolving under the action of the field-free propagator U_0. At t_0, which can be called the ionization time, the initial state is ionized by the laser field $V_L(t_0)$ and starts to propagate in the combined fields of the ionic core and the laser by the full propagator $U(t_C, t_0)$. The time t_C can be associated with the collision time, at which the returning electron scatters off the ion with the scattering potential $V_C(t_C)$. From there, it is propagated towards the detector by the propagator $U_V(t, t_C)$. Note that this latter propagator only includes the interaction with the laser field and not with the potential of the parent ion (the target). The second term represents the reference wave packet. Just as the signal wave packet, it stays in the ground state until the time t_0, when it is ionized by the laser $V_L(t_0)$ and propagated towards the detector by $U_V(t, t_0)$. Note that, once again, the propagator $U_V(t, t_0)$ includes only the laser field. The last term describes the non-ionized system. We stress that the full expression in Equation (4.2) is the exact formal solution of the TDSE.

In the following sections Equation (4.2) will be derived and the derivation of the phase difference between the signal and reference waves will be given. We will also focus on different types of patterns in the photoelectron velocity map images that originate from different types of electron wave packet interferences.

4.1.2 Derivation of the exact expression

In this section we will derive Equation (4.2). We start with the TDSE in atomic units:

$$i\frac{\partial\psi}{\partial t} = H\psi \tag{4.3}$$

Here H is the full Hamiltonian of the system. The time-evolution of the wave function can be obtained by using a time propagator $U(t,0)$, which propagates the wave packet in time from $t = 0$ to t:

$$\psi(t) = U(t,0)\psi(0) \tag{4.4}$$

$U(t,0)$ is formally expressed by the equation:

$$U(t,0) = \exp\left[-i\int_0^t d\tau H(\tau)\right] \tag{4.5}$$

where the time-ordering operator is omitted for brevity. Let us now split the Hamiltonian into two parts: $H = H_0 + V_L$ with the unperturbed Hamiltonian $H_0 = \mathbf{p}^2/2 + V_C$, the scattering potential V_C and the laser field V_L. By using a Dyson series we can write a different exact expression for the propagator $U(t,0)$:

$$U(t,0) = U_0(t,0) - i\int_0^t dt_0 U(t,t_0)V_L(t_0)U_0(t_0,0) \tag{4.6}$$

Here $U_0(t,0) = \exp[-iH_0t]$ is the field-free propagator. The exact solution to the Schrödinger equation can now be written as:

$$\psi(t) = U_0(t,0)\psi(0) - i\int_0^t dt_0 U(t,t_0)V_L(t_0)U_0(t_0,0)\psi(0) \tag{4.7}$$

To describe the electron dynamics in the continuum at $t > t_0$, we apply a different partitioning to the Hamiltonian: $H = H_V + V_C$, with $H_V = \mathbf{p}^2/2 + V_L$ representing the interaction with the laser and V_C representing the scattering potential. The exact expression for the full propagator reads:

$$U(t,t_0) = U_V(t,t_0) - i\int_{t_0}^t dt_C U_V(t,t_C)V_C(t_C)U(t_C,t_0) \tag{4.8}$$

where $U_V(t,t_0) = \exp\left[-i\int_{t_0}^t d\tau H_V(\tau)\right]$ is the so-called Volkov propagator that neglects the interaction with the ion but includes the laser field fully. If we substitute Equation (4.8) into Equation (4.7) we obtain the full solution including ionization

and scattering.

$$\begin{aligned}\psi &= -\int_0^t dt_0 \int_{t_0}^t dt_C U_V(t,t_C)V_C(t_C)U(t_C,t_0)V_L(t_0)U_0(t_0,0)\psi(0) \\ &\quad -i\int_0^t dt_0 U_V(t,t_0)V_L(t_0)U_0(t_0,0)\psi(0) + U_0(t,0)\psi(0) \end{aligned} \tag{4.9}$$

The first term represents the part of the wave packet that scatters - the signal wave packet. The second term is the reference wave packet. The third term represents the part of the wave packet that remains in the bound state, which is irrelevant for the photoelectron spectra. For the amplitude of detecting the electron with the final momentum $\mathbf{p}$ we have:

$$\begin{aligned}a_p &= -\int_0^t dt_0 \int_{t_0}^t dt_C \langle \mathbf{p}|U_V(t,t_C)V_C(t_C)U(t_C,t_0)V_L(t_0)U_0(t_0,0)|\psi(0)\rangle \\ &\quad -i\int_0^t dt_0 \langle \mathbf{p}|U_V(t,t_0)V_L(t_0)U_0(t_0,0)|\psi(0)\rangle \end{aligned} \tag{4.10}$$

Here $\mathbf{p} = (p_r, p_z)$ is the final momentum, z is the direction of the laser polarization and r the direction orthogonal to it. Equations (4.9, 4.10) complete the derivation of Equation (4.2). The two terms in Equation (4.10) can be associated with the signal and the reference wave packets. Note that the second partitioning made ($H = H_V + V_C$), is only valid when $p_r \gg p_r^C$, where p_r^C is the perpendicular momentum acquired due to the interaction with the scattering potential. For $p_r \sim p_r^C$ a different partitioning scheme should be used, which will be described elsewhere. This completes the discussion of the exact formal expressions for the holographic pattern.

4.1.3 Strong Field Approximation

The analysis can be simplified by using the strong-field approximation for the evolution between t_0 and t_C in the first term in Equation (4.10). Using the resolution of identity on momentum states represented by plane waves $\int dk|\mathbf{k}\rangle\langle\mathbf{k}| = 1$ we

obtain:

$$
\begin{aligned}
a_p &= \langle \mathbf{p}|\psi\rangle \\
&= -\int_0^t dt_0 \int_{t_0}^t dt_C \int d\mathbf{k} \langle \mathbf{p}|U_V(t,t_C)V_C(t_C)|\mathbf{k}\rangle \langle \mathbf{k}|U_V(t_C,t_0)V_L(t_0)U_0(t_0,0)|\psi(0)\rangle \\
&\quad -i\int_0^t dt_0 \langle \mathbf{p}|U_V(t,t_0)V_L(t_0)U_0(t_0,0)|\psi(0)\rangle \\
&= -\int_0^t dt_0 \int_{t_0}^t dt_C \int d\mathbf{k} \exp\left[-\frac{i}{2}\int_{t_C}^t d\tau(\mathbf{p}+A(\tau))^2\right] \langle \mathbf{p}(t_C)|V_C(t_C)|\mathbf{k}\rangle \\
&\quad * \exp\left[-\frac{i}{2}\int_{t_0}^{t_C} d\tau(\mathbf{k}+A(\tau))^2\right] \langle \mathbf{k}(t_0)|V_L(t_0)|\psi(t_0)\rangle \exp\left[i\mathrm{IP}t_0\right] \\
&\quad -i\int_0^t dt_0 \exp\left[-\frac{i}{2}\int_{t_0}^{t_C} d\tau(\mathbf{p}+A(\tau))^2\right] \langle \mathbf{p}(t_0)|V_L(t_0)|\psi(t_0)\rangle \exp\left[i\mathrm{IP}t_0\right] \qquad (4.11)
\end{aligned}
$$

Here the application of SFA resulted in the substitution of the full propagator U by U_V. In this equation $A(t) = -A_0 \sin\omega t$ is related to the laser field strength $E(t)$ as $E(t) = -\partial A(t)/\partial t$, $\mathbf{p} = (p_r, p_z)$ is the final momentum, z is the direction of the laser polarization, $\mathbf{k} = (k_r, k_z)$ is the momentum before scattering, and IP is the ionization potential.

Rewriting Equation (4.11) in a simpler form and omitting the pre-exponential term one obtains:

$$
a = \langle p|\psi\rangle \approx -\int_0^t dt_0 \int_{t_0}^t dt_C \int d\mathbf{k} \exp\left[-iS_{\mathrm{signal}}(t,t_C,t_0)\right] - i\int_0^t dt_0 \exp\left[-iS_{\mathrm{ref}}(t,t_0)\right] \qquad (4.12)
$$

where

$$
S_{\mathrm{signal}}(t,t_C,t_0) = \frac{1}{2}\int_{t_C}^t d\tau(\mathbf{p}+A(\tau))^2 + \frac{1}{2}\int_{t_0}^{t_C} d\tau(\mathbf{k}+A(\tau))^2 - \mathrm{IP}t_0
$$

and

$$
S_{\mathrm{ref}}(t,t_0) = \frac{1}{2}\int_{t_0}^t d\tau(\mathbf{p}+A(\tau))^2 - \mathrm{IP}t_0
$$

There are four integrals to evaluate in Equation (4.12). Evaluation of the integrals is done by using the saddle point method, which requires one to find the point at which the derivative of S with respect to the integration variable is zero.

The first saddle point equation is derived by taking the derivative with respect to t_0 (from now on the time arguments in S will be suppressed):

$$\begin{aligned} dS_{\text{ref}}/dt_0 = 0 \quad &\Rightarrow \quad \frac{1}{2}(p_z - A_0\sin(\omega t_0))^2 = -\frac{1}{2}p_r^2 - \text{IP} \\ dS_{\text{signal}}/dt_0 = 0 \quad &\Rightarrow \quad \frac{1}{2}(k_z - A_0\sin(\omega t_0))^2 = -\frac{1}{2}k_r^2 - \text{IP} \end{aligned} \tag{4.13}$$

From these equations it follows that a non-zero initial orthogonal momentum corresponds to a higher effective ionization potential $\text{IP}_{\text{eff}} = \text{IP} + \frac{1}{2}k_r^2$. Note that t_0 is complex: $t_0 = t_0' + it_0''$ .The phase terms in Equation (4.12) include integration in real time from t_0 to t_C. Integration in complex time from t_0 to the real axis yields the following additional phase:

$$\begin{aligned} S_{\text{ref}}^{\text{Im}} &= \frac{1}{2}\int_{t_0''}^{0} d\tau''(\mathbf{p} + A(\tau''))^2 \\ &= \frac{A_0^2}{\omega}\Bigg[\sin(\omega t_B)\cos(\omega t_0')(1-\cosh(\omega t_0'')) \\ &\qquad + \frac{1}{2}\sin(\omega t_0')\cos(\omega t_0')(1-\cosh(2\omega t_0''))\Bigg] \end{aligned} \tag{4.14}$$

The same can be done for the expression representing the signal wave $S_{\text{signal}}^{\text{Im}}$. By making use of Equation (4.13) the following expression for t_0 can be obtained [90]:

$$\begin{aligned} t_0 &= \frac{1}{\omega}\left(\arcsin\sqrt{P} + i\,\text{arccosh}\left(\frac{S}{\sqrt{P}}\right)\right) \\ S &= \sin(\omega t_B) \\ P &= \frac{1}{2}(1+\gamma^2+S^2-\sqrt{D}) \\ D &= (1-\gamma^2)^2 + S^4 + 2S^2(\gamma^2-1) \end{aligned} \tag{4.15}$$

The time t_B is defined as the moment when the velocity on the electron trajectory is equal to zero, formally parameterizing k_z as $k_z = A_0\sin(\omega t_B)$ and linking the quantum analysis, which yields complex ionization times associated with tunneling, to the classical three-step model (see below).

The second saddle-point equation tells us that the signal wave packet ionizes with zero orthogonal momentum:

$$dS_{\text{signal}}/dk_r = 0 \quad \Rightarrow \quad k_r = 0 \tag{4.16}$$

It readily follows from Equations 4.13 and 4.16 that the time of ionization of the reference beam is not the same as the time of ionization of the signal beam, i.e. $t_0^{\text{ref}} \neq t_0^{\text{signal}}$.

The third saddle-point equation leads to the following expression:

$$dS_{\text{signal}}/dk_z = 0 \quad \Rightarrow \quad \int_{t_0}^{t_C} \frac{\partial}{\partial k_z}[k_z - A_0\sin(\omega\tau)]^2 d\tau = 0 \tag{4.17}$$

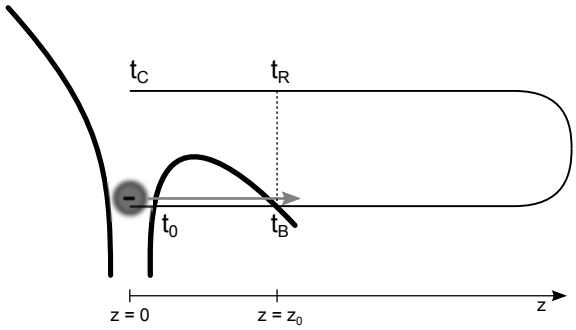

FIGURE 4.1: **Schematic drawing of the path that an electron follows in a strong laser field under the barrier and in the continuum.** The thick black line represents the combined laser and Coulomb field that the electron experiences. The path followed by the electron is indicated by the thin black line. Tunneling starts at complex time t_0. At "birth time" t_B the instantaneous electron velocity is equal to zero. In the classical three-step model this moment corresponds to the instant when the electron comes out of the barrier at a distance z_0. Once in the continuum, the electron makes an excursion in the laser field before coming back to z_0 at the return time t_R. At t_C the electron is back at the origin where it scatters.

It is convenient to evaluate this integral via splitting it into three parts:

$$\int_{t_0}^{t_C} d\tau = \int_{t_R}^{t_C} d\tau + \int_{t_B}^{t_R} d\tau + \int_{t_0}^{t_B} d\tau$$

As introduced before, t_0 is the starting time for tunneling, t_B is the moment when the electron velocity is equal to zero, which within the classical three-step model can be associated with the moment when the wave packet exits the barrier at a distance z_0 from the origin, and t_C is the moment of recollision, see Figure 4.1. The return time t_R is the moment at which the electron returns to the position it had at t_B, associated with the tunnel exit point z_0. This analysis explicitly neglects the possible tunneling of the electron back into the classically forbidden region, upon returning to the origin.

It follows that

$$\int_{t_B}^{t_R} \frac{\partial}{\partial k_z}[k_z - A_0 \sin(\omega\tau)]^2 dt_C = 0$$

$$\Rightarrow \sin(\omega t_B) \cdot (\omega t_R - \omega t_B) + \cos(\omega t_R) - \cos(\omega t_B) = 0 \tag{4.18}$$

where again we have used the parameterization, $k_z = A_0 \sin(\omega t_B)$. From this equation we can obtain the relation between t_B and t_R numerically, e.g. by using Newton's method. From splitting the integrals it also follows that:

$$\int_{t_R}^{t_C} \frac{\partial}{\partial k_z}[k_z - A_0 \sin(\omega\tau)]^2 d\tau = -\int_{t_0}^{t_B} \frac{\partial}{\partial k_z}[k_z - A_0 \sin(\omega\tau)]^2 d\tau = z_0 \tag{4.19}$$

Neglecting the small imaginary component of z_0, we obtain the relation between t_R and t_C, while the relation between t_0 and t_B is given by Equation 4.15.

The fourth and last saddle-point equation gives the relation between p_z and p_r.

$$\begin{aligned} dS_{signal}/dt_C = 0 \Rightarrow \\ p_z = -A_0\sin(\omega t_C) \pm \sqrt{(-A_0\sin(\omega t_B) + A_0\sin(\omega t_C))^2 - p_r^2} \end{aligned} \tag{4.20}$$

By applying all the saddle-point equations and including the complex integration Equation 4.11 reduces to:

$$\begin{aligned} \langle p|\psi(t)\rangle \approx \exp\Bigg[-\frac{i}{2}\int_{t_C}^{t} d\tau (p_z + A(\tau))^2 - \frac{i}{2}p_r^2(t - t_C) \\ - \frac{i}{2}\int_{t_0^{\text{signal}}}^{t_C} d\tau (k_z + A(\tau))^2 + i\text{IP}t_0^{\text{signal}} + iS_{\text{signal}}^{\text{Im}} \Bigg] \\ + \exp\Bigg[-\frac{i}{2}\int_{t_0^{\text{ref}}}^{t} d\tau (p_z + A(\tau))^2 - \frac{i}{2}p_r^2(t - t_0^{\text{ref}}) + i\text{IP}t_0^{\text{ref}} + iS_{\text{ref}}^{\text{Im}} \Bigg] \end{aligned} \tag{4.21}$$

Since we are interested in the interference we need to calculate the acquired phase difference between the reference and signal wave packet.

$$\begin{aligned} \Delta\phi &= \phi_{\text{signal}} - \phi_{\text{ref}} \\ &= -\frac{1}{2}\int_{t_0^{\text{signal}}}^{t_C} d\tau (k_z + A(\tau))^2 - \frac{1}{2}p_r^2(t_C - t_0^{\text{ref}}) + \frac{1}{2}\int_{t_0^{\text{ref}}}^{t_C} d\tau (p_z + A(\tau))^2 \\ &\quad + \text{IP}(t_0^{\text{signal}} - t_0^{\text{ref}}) + S_{\text{signal}}^{\text{Im}} - S_{\text{ref}}^{\text{Im}} \end{aligned} \tag{4.22}$$

Here the second term is identified as the dominant term accounting for the phase difference in holographic structures. The resulting holographic structures are shown in Figure 4.2a. Here we also include the amplitude factor reflecting the shape of the electron wave packet in transversal direction [58]:

$$\psi(p_r) = \psi(0)\exp\left[-\frac{p_r^2}{2}\tau\right] \tag{4.23}$$

Where τ is the imaginary part of t_0.

4.1.4 Time information in the Hologram

Since the second term in Equation 4.22 is identified as the dominant term accounting for the phase difference in the holographic structures, we can write:

$$\Delta\phi \approx -p_r^2(t_C - t_0^{\text{ref}})/2$$

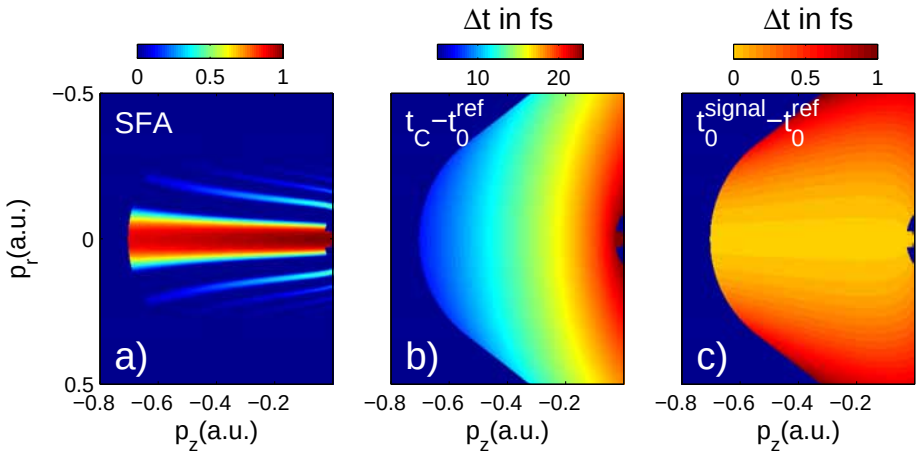

FIGURE 4.2: **SFA calculation on Holography.** (a) gSFA calculation of a hologram, where a coherent electron source is created at distance z_0 from the ion by tunnel ionization and where the subsequent propagation of the electron wave packet under the influence of the laser field leads to the creation of a reference and signal beam. The calculation is performed with the experimental values for F_{laser}, λ_{laser} and IP as given in Chapter 3 and shows the cosine of the phase difference between the signal and reference wave packet (Equation 4.22), including the amplitude factor (Equation 4.23). (b) Relation between (p_z, p_r) and the time difference $t_C - t_0^{\text{ref}}$, suggesting that the hologram can be thought of as a pump-probe experiment that records dynamics of the ionic core. (c) Relation between (p_z, p_r) and the time difference $t_0^{\text{signal}} - t_0^{\text{ref}}$, suggesting that the hologram can measure the time evolution of the ionization process.

Thus, the hologram can be viewed as a pump-probe experiment, where the moment of birth of the reference wave packet t_0^{ref} starts an experiment, while at a later time t_C the scattering potential is probed. If the scattering potential changes between t_0^{ref} and t_C, this will be encoded in the hologram. In Figure 4.2b the relation between (p_z, p_r) and the time differences $t_C - t_0^{\text{ref}}$ is shown. In addition, t_C, is directly related to the time-of-birth of the signal wave packet t_0^{signal}. Therefore, changes in the ionization between t_0^{ref} and t_0^{signal} are recorded as well. In Figure 4.2c the relation between (p_z, p_r) and the time differences $t_0^{\text{signal}} - t_0^{\text{ref}}$ is shown. The interfering trajectories that produce the characteristic fringe pattern in Figure 4.2a originate from the same quarter cycle. Thus, sub-cycle time resolution is obtained even when long pulses are used.

4.1.5 Different wave packet interferences

The saddle point method allows one to identify different types of trajectories leading to interference structures in the photoelectron spectrum. In Figure 4.3 these different types of interferences and the corresponding ionization times are shown. Figure 4.3a shows the well-known ATI structure. The ATI rings originate from the interference between electron wave packets that are ionized exactly one

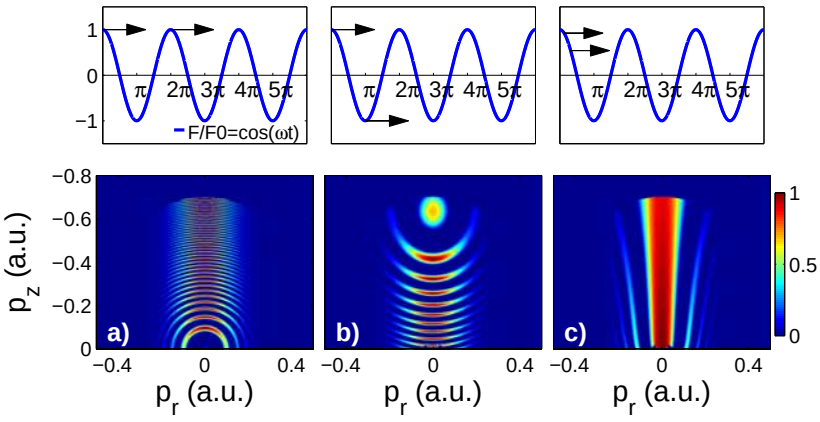

FIGURE 4.3: **Wavepacket interferences.** Three different types of interferometric structures in photoelectron spectra accompanying strong field ionization (lower panel), corresponding to different types of interfering electron trajectories originating either from different quarter-cycles of the laser field (upper panel (a,b) or the same quarter-cycle (upper panel (c)). All spectra have been calculated with F = 0.0045 a.u. IP = 0.14 a.u. ω = 0.00641 a.u. and are based on Equations 4.22 and 4.23. (a) Two wave packets ionized with exactly one cycle relative delay (cosine of the phase difference of two reference wave packets that are ionized exactly one cycle from each other). The resulting pattern consists of rings that are spaced by the energy of one photon. This behavior is usually described by the term Above Threshold Ionization (ATI). (b) Interference between two wave packets that are ionized within the same cycle but appear on opposite sides of the ion (cosine of the phase difference of two reference wave packets that are ionized within the same cycle with the same value for the vector potential). This type of interference has been experimentally observed [49],[50] and described theoretically [47]. (c) Holographic pattern that arises from the interference between two electron wave packets that are emitted during the same quarter cycle of the laser field. One wave packet goes to the detector without scattering from the short-range part of the target potential, while the other wave packet scatters off this potential before reaching the detector (cosine of the phase difference of a reference and scattered wave packet that are ionized within a quarter cycle)

full cycle apart from each other. Figure 4.3b shows another type of the interference pattern which arises from the interference of two wave packets ionized at instants t_1 and t_2 within the same laser cycle, for which $A(t_1) = A(t_2)$ and consequently the laser electric field has opposite values, $E(t_1) = -E(t_2)$. As a result, the two wave packets appear on the *opposite* sides of the ion, but have the *same* drift momentum. Before reaching the detector, the first wave packet is turned around by the laser field while the second wave packet drifts directly to the detector without revisiting the parent ion. Both types of interference cause a pattern in the radial direction. Completely different patterns are caused by the interference of electron wave packets originating from the same quarter of the laser cycle. This is the type of interference responsible for the hologram as shown in Figure 4.3c.

4.2 CCSFA algorithm

To be able to include the Coulomb force properly, we turn to another method, the coulomb corrected strong field approximation (CCSFA), which is the basis for the calculation of the momentum distribution displayed in Figure 3.4. For a full understanding of this method an introduction into the standard strong field approximation (referred to as plain SFA below) is essential. Within the standard strong field approximation the transition amplitude from an initial bound atomic state $|\Psi_i\rangle$ into a state with asymptotic momentum $\mathbf{p}$ is given by the matrix element:

$$M_{\mathrm{SFA}}(\mathbf{p}) = -i \int_{-\infty}^{+\infty} \langle \Psi_{\mathbf{p}}^{V} | V_F(t) | \Psi_i \rangle dt \tag{4.24}$$

where $|\Psi_{\mathbf{p}}^{V}\rangle$ is a Volkov state, i.e. the exact solution to the Schrödinger (Dirac) equation for an electron in the field of a plane electromagnetic wave. In the nonrelativistic dipole approximation, which is sufficient for our purposes, the respective wave function has the form (in the length gauge):

$$\Psi_{\mathbf{p}}^{V}(\mathbf{r}, t) = (2\pi)^{-3/2} \exp\left\{ i\mathbf{v}_{\mathbf{p}} \cdot \mathbf{p} - \frac{i}{2} \int_{-\infty}^{t} \mathbf{v}_{\mathbf{p}}^{2}(t')dt' \right\} \tag{4.25}$$

Here $\mathbf{v}_{\mathbf{p}} = \mathbf{p} + \mathbf{A}(t)$ is the time-dependent electron velocity in the field described by the vector potential $\mathbf{A}(t)$ and $\mathbf{p}$ is the asymptotic (drift) momentum. The electric field of the wave is $\mathbf{E}(t) = -\partial\mathbf{A}/\partial t$. In the same gauge the interaction operator is given by:

$$V_F(t) = \mathbf{r} \cdot \mathbf{E}(\mathbf{t}) \tag{4.26}$$

When the photon energy is much less than the ionization potential of the bound state, $\hbar\omega \ll \mathrm{IP}$, the ionization may only proceed via multiphoton absorption, i.e. in a highly nonlinear interaction with the field. In this case the integral over time in Equation 4.24 can be carried out by a saddle point method as also used in the previous section. Using saddle-points means that the amplitude is calculated as a sum of saddle-point contributions:

$$M_{\mathrm{SFA}}(\mathbf{p}) \approx \sum_{n} \mathcal{P}(\mathbf{p}, t_{sn}) \exp\left\{ iS(\mathbf{p}, t_{sn}) \right\}, \tag{4.27}$$

where $S(\mathbf{p}, t_{sn})$ is the classical action for a particle in the field of a plane electromagnetic wave, for saddle point times t_s and the number of contributing saddle points n:

$$S(\mathbf{p}, t) = \int_{-\infty}^{t} \left[\mathbf{v}_{\mathbf{p}}^{2}(\tau)/2 + \mathrm{IP} \right] d\tau. \tag{4.28}$$

The pre-factor $\mathcal{P}(\mathbf{p}, t)$ contains the spatial matrix element and the second time derivative of the action. Usually the pre-factor is a smooth function of the final

momentum and laser and atom parameters, so that the shape of the momentum distribution is mostly determined by the exponential part of Equation 4.27, and hence by the classical dynamics of the particle in the laser field.

The equation for the saddles $t_s(\mathbf{p})$ is obtained from the requirement that $\partial S/\partial t = 0$ and reads as (see also Equation 4.13 above)

$$(\mathbf{p} + \mathbf{A}(t_s))^2 + 2\mathrm{IP} = 0 \tag{4.29}$$

For a given final momentum $\mathbf{p}$ this equation has several roots. All of them are complex, and only those with positive imaginary parts should be accounted for in the sum of Equation 4.27. For a linearly polarized pulse there are two such solutions per optical cycle. Equations 4.27 and 4.29 represent the standard approach for calculations of the strong field ionization amplitude within the plain SFA.

This result can be equivalently reformulated in terms of complex classical trajectories also known as quantum orbits. To this end we rewrite the action in the exponential of Equation 4.27 as

$$S(\mathbf{p}, t_s) = \int_{-\infty}^{+\infty} \left[\mathbf{v}_{\mathbf{p}}^2(\tau)/2 + \mathrm{IP}\right] d\tau - \int_{t_s}^{+\infty} \left[\mathbf{v}_{\mathbf{p}}^2(\tau)/2 + \mathrm{IP}\right] d\tau \equiv \Phi(\mathbf{p}) - S_0(\mathbf{p}, t_s) \tag{4.30}$$

The phase factor $\exp(i\Phi(\mathbf{p}, t))$ can be safely omitted, so that the ionization amplitude is given by Equation 4.27 with S replaced by $-S_0$. This allows for a useful interpretation, namely, that the action $S_0(\mathbf{p}, t_s)$ is evaluated along a trajectory which started at a complex time instant $t_s(\mathbf{p})$ at the origin, $\mathbf{r}(t_s) = 0$, where the electron was trapped in its bound state, and then goes to infinity, where it is detected in real time having an asymptotic momentum $\mathbf{p}$.

The saddle-point action $S_0(\mathbf{p}, t_s)$ can be separated into an integral from the complex saddle-point time $t_s(\mathbf{p})$ down to the real axis where $t = Re(t_s) \equiv t_0$ and then along the real axis from t_0 to infinity, i.e., $S_0(\mathbf{p}, t_s) = S_0^{\downarrow} + S_0^{\rightarrow}$. In the plain SFA both contributions can be calculated analytically for a given (analytical) vector potential. Indeed, consider the equations of motion

$$\dot{\mathbf{r}} = \mathbf{v} = \mathbf{p} + \mathbf{A}(t), \qquad \dot{\mathbf{p}} = 0 \tag{4.31}$$

Clearly,

$$\mathbf{p} = \mathrm{const}, \qquad \mathbf{r}(t) = \mathbf{p}(t - t_s) + \int_{t_s}^{t} \mathbf{A}(\tau) d\tau \tag{4.32}$$

In the tunneling limit the value $\mathbf{r}(t_0) = (z_0, 0, 0)$ can be identified with the geometrical tunnel exit, $z_0 \approx \mathrm{IP}/E(t_0)$. Substituting this solution into the action $S_0(\mathbf{p}, t_s)$ one obtains exactly the standard SFA amplitude (Equation 4.27). Notice that in the Coulomb-free case the trajectory $\mathbf{r}(\mathbf{p}, t)$ itself does not enter the action.

In our CCSFA the equation of motion 4.31 is replaced by

$$\dot{\mathbf{r}} = \mathbf{v} = \mathbf{p} + \mathbf{A}(\mathbf{t}), \qquad \dot{\mathbf{p}} = -Z\mathbf{r}/r^3 \tag{4.33}$$

where Z is the ionic charge (below Z is take to be one, $Z = 1$, as we consider neutral atoms), and simultaneously the final momentum $\mathbf{p}$ is replaced by some value $\mathbf{p}_0$ in Equation 4.27, such that with the new initial time $\tilde{t}_s(\mathbf{p}) = t_s(\mathbf{p}_0)$ and the new initial conditions for motion in real time

$$\mathbf{r}(\tilde{t}_0) = \mathbf{p}_0(\tilde{t}_0 - \tilde{t}_s) + \int_{\tilde{t}_s}^{\tilde{t}_0} \mathbf{A}(\tau)d\tau, \qquad \dot{\mathbf{r}}(\tilde{t}_0) = \mathbf{p} + \mathbf{A}(\tilde{t}_0) \tag{4.34}$$

the asymptotic momentum is again $\mathbf{p}$.

The CCSFA action reads as

$$S_C(\mathbf{p}, t_s) = \int_{\tilde{t}_s}^{+\infty} [{\mathbf{v}_\mathbf{p}}^2(\tau)/2 + \mathrm{IP} - Z/r]d\tau \tag{4.35}$$

It can also be separated in two parts, $S_C(\mathbf{p}, t_s) = S_C^{\downarrow} + S_C^{\rightarrow}$, i.e. a sub-barrier part and a real-time contribution. The action of the Coulomb potential on the imaginary dynamics during the tunneling process strongly affects the ionization probability but hardly changes the shape of the photoelectron spectra so that in the present study we neglect this contribution. However, note that due to the replacement of $\mathbf{p}$ by $\mathbf{p}_0$ and the Coulomb modified saddle-point times $S_C^{\downarrow} \neq S_0^{\downarrow}$.

Summarizing this part, to calculate the amplitude of ionization into a final state with momentum $\mathbf{p}$ one has to solve Equation 4.33 with initial conditions given by Equation 4.34 together with the saddle point Equation 4.29, one has to evaluate the action (Equation 4.35) and then substitute it into Equation 4.27. Since, however, the initial conditions defining a particular trajectory depend on this trajectory themselves (via the saddle-point equation), the evaluation of Coulomb-corrected trajectories and respective saddle-points turns to become quite a cumbersome ***inverse*** problem. To avoid difficulties inherent to inverse problems, we implement a "shooting" method: instead of calculating new saddle-points $\tilde{t}_s$ and new "initial" drift momenta $\mathbf{p}_0$, we assign some momentum $\mathbf{p}_0$ (it can be arbitrary), calculate the respective saddle-point time t_s, derive the respective initial conditions from Equation 4.34 and calculate the final momentum according to Equation 4.33. Then

$$S_C^{\downarrow}(\mathbf{p}, \tilde{t}_s) = S_0^{\downarrow}(\mathbf{p}_0, \tilde{t}_s) \;\text{ and }\; S_C^{\rightarrow}(\mathbf{p}, t_s) \;=\; \int_{t_0}^{+\infty} [{\mathbf{v}_\mathbf{p}}^2(\tau)/2 + \mathrm{IP} - 1/r]d\tau \tag{4.36}$$

and the amplitude is given by Equation 4.27 with S replaced by $-S_C$. This procedure is simple and straightforward, but a certain difficulty arises. As is known, several different trajectories can lead to the same final state. This generates interference structures in the spectra. In the method of shooting we described above different $\mathbf{p}_0$ would never lead into ***exactly*** the same final state unless we scan the space of $\mathbf{p}_0$ continuously. Therefore, to take into account the effect of interference we introduce a fine grid in the final momentum space $\mathbf{p}$ and identify all trajectories which end up in a given bin of the grid.

This algorithm is implemented as follows. Two loops run over $p_{0z} \in [-p_{0z}^{\max}, p_{0z}^{\max}]$ and $p_{0r} \in [-p_{0r}^{\max}, p_{0r}^{\max}]$. For each initial momentum Equation 4.29 is solved for t_s using a complex-root-finding routine. Each t_s corresponds to a trajectory. Hence, there is another loop over all t_s found. The complex part of the action S_C is given by Equation 4.36, neglecting the effect of the Coulomb potential. The trajectory corresponding to a saddle-point t_s is calculated from t_0 up to the end of the pulse $t = T$ according to the equations of motion (all time-arguments suppressed)

$$\dot{z} = p_z + A,\ \dot{r} = p_r, \qquad \dot{p}_z = -z/(r^2+z^2)^{3/2},\ \dot{p}_r = -r/(r^2+z^2)^{3/2} \quad (4.37)$$

for the initial conditions

$$z(t_0) = Re\left[p_z(t_0 - t_s) + \int_{t_s}^{t_0} A(\tau)d\tau\right],\ p_z(t_0) = p_{0z},\quad r(t_0) = 0,\quad p_r(t_0) = p_{0r} \quad (4.38)$$

using a Runge-Kutta solver. If the energy $\epsilon(T) = p^2(T)/2 - 1/r(T)$ is negative, the trajectory does not correspond to a free electron and thus does not contribute to the photoelectron spectrum. If the energy is positive the asymptotic momentum $\mathbf{p}$ can be calculated from $\mathbf{p}(T)$ and $\mathbf{r}(T)$ using Kepler's laws, avoiding unnecessary explicit propagation up to large times. Finally, the result for the t_s under consideration is stored in a table of the form p_{0z}, p_{0r}, p_z, p_r, S_C. Once the loops over the initial momenta are completed, the table with the trajectory data can be post-processed. The trajectories are binned according to their asymptotic momentum, and the CCSFA matrix element

$$M_{\mathrm{CCSFA}}(\mathbf{p}) \approx \sum_n P(\mathbf{p}, t_{sn}) \exp\left[-iS_C(\mathbf{p}, t_{sn})\right] \quad (4.39)$$

is calculated, where the sum is over all trajectories ending up in the final momentum bin centered at $\mathbf{p}$.

5 Scaling laws for photoelectron holography in the mid-infrared wavelength regime

Mid-infrared strong field laser ionization allows to measure holograms of atoms and molecules, which contain both spatial and temporal information of the ion and the photoelectron with sub-femtosecond temporal and Ångström spatial resolution. We report on the scaling of photoelectron holographic interference patterns with the laser pulse duration, wavelength and intensity. High-resolution holograms for the ionization of metastable xenon atoms by 7-16 µm light from the FELICE free electron laser are presented and compared to semi-classical calculations that provide analytical insight.

5.1 Introduction

The concept of holography [31] can be applied to strong field laser ionization to record both temporal and spatial information on the atomic or molecular scale [56]. In conventional holography, a coherent beam of light or electrons is split into a signal and a reference beam. The signal beam scatters off the target and, upon recombination with the reference beam, creates an interference pattern that stores spatial information about the target. In photoelectron holography the electron beam is created by laser-induced tunnel ionization. After tunneling, the electron wave packet moves in the oscillatory laser electric field and can follow two paths en route to the detector. When the electron starts off with a relatively small lateral velocity with respect to the laser polarization, it will be driven back to the ion and scatter, generating a signal wave. For large lateral velocities, the electron will make a wide turn around the ion and form a reference wave. The interference of the signal and reference electron wave packets on a detector creates the photoelectron hologram.

The benefit of using laser-generated electrons for holography is two-fold. Firstly, very high electron densities can be obtained at the ionic target [54]. Secondly, both spatial and temporal information is encoded [52], which includes information on the dynamics of both the target ion and the electron. When using mid-infrared (mid-IR) laser sources, the sub-cycle timescales involved yield femtosecond and attosecond resolution for, respectively, the target ion and electron dynamics.

5.2 Experimental and Theoretical Methods

In this paper we explore how the holographic interference patterns scale with laser intensity, pulse duration and wavelength. To this end, experiments were carried out at the Free Electron Laser for Intra-Cavity Experiments (FELICE), where metastable xenon atoms in the $5p^5(2P3/2)6s[3/2]_2$ state were ionized using short (typ. 5-20 cycles) mid-IR laser pulses with wavelengths ranging from 7 to 16 µm. The experimental setup used is the same as presented in Chapter 3 (Figure 3.2). Xenon atoms were introduced by means of a pulsed valve into an experimental apparatus that was integrated into the FELICE laser cavity, and were excited to the metastable state by electron impact excitation [63]. In the interaction region, the metastable atoms were ionized by the Free Electron Laser (FEL). In the Velocity Map Imaging (VMI) detector, electrodes were used to drive photoelectrons towards a position-sensitive detector [64] that consisted of two micro-channel plates, a phosphor screen and a CCD camera. The laser polarization was parallel to the plane of the imaging detector, allowing a reconstruction of the 3D velocity distribution, which in this Chapter has been done for all data with an iterative procedure [81]. The wavelength and pulse duration were controlled by changes to the FEL operation, whereas the intensity was varied by bringing the experimental apparatus in or out of focus by moving it along the laser propagation direction.

The experimental results will be compared to two semi-classical methods that are based on the Strong Field Approximation (SFA) [34, 91, 92]. In standard SFA, the assumption is made that after tunnel ionization the Coulomb forces on the electron are negligibly small compared to the laser forces that are present. This assumption rules out scattering of the electron wave packet upon returning to the target ion. In photoelectron holography, however, electron-ion scattering is crucial, and therefore in the generalized SFA (gSFA) method scattering is included in the following way: when the electron returns to the core with momentum $\mathbf{k}$, it is assumed to elastically scatter to a momentum $\mathbf{p}$ (with $|\mathbf{p}| = |\mathbf{k}|$).

Within this model, the final wave packet that reaches the detector can be expressed as:

$$\psi = \psi_{\text{signal}} + \psi_{\text{ref}} \tag{5.1}$$

Whereas the signal wave packet ψ_{signal} scatters off the target, the reference wave packet ψ_{ref} is not influenced at all by the Coulomb force and only experiences the influence of the laser field. The phase-difference between the two wave packets that gives rise to the hologram is (see Equation (4.22)):

$$\Delta\phi = \phi_{\text{signal}} - \phi_{\text{ref}} = -\frac{1}{2}\int_{t_o^{\text{signal}}}^{t_C} \nu_z^2 d\tau + \frac{1}{2}\int_{t_o^{\text{ref}}}^{t_C} \nu_z^2 d\tau - \frac{1}{2}p_r^2(t_C - t_0^{\text{ref}}) + \text{IP}\Delta t_0 + \Delta S^{\text{Im}} \tag{5.2}$$

with the phase of the signal and reference wave packet defined as ϕ_{signal} and ϕ_{ref}. On the right side of this equation the first and second term represent the phase evolution of, respectively, the signal and reference wave packet in the direction

parallel to the laser polarization and the third term is the phase difference acquired in the orthogonal direction. The fourth term is the phase difference caused by a difference in the ionization times of the reference and signal waves and the last term is the phase difference acquired during propagation in imaginary time (i.e. during the tunnel-ionization). The third term in expression 5.2 has been identified as the key term responsible for the holographic sidelobe pattern [56], allowing to approximate:

$$\Delta\phi \approx -\frac{1}{2}p_r^2(t_C - t_0^{\text{ref}}) \tag{5.3}$$

where p_r is the momentum orthogonal to the laser polarization axis, t_C is the moment of electron-ion re-collision and t_0^{ref} is the time the reference wave packet starts tunneling through the barrier. These ionization times (t_0) are determined via the saddle-point method [93]. A more detailed description is given in Chapter 4.

Whereas the gSFA method assumes short-range scattering, the Coulomb Corrected Strong Field Approximation (CCSFA) method [43, 56, 85] corrects both the signal and reference electron trajectories for the long range Coulomb force. In the CCSFA, a grid of final momenta $\mathbf{p}_0$ is selected. The saddle point times corresponding to these final momenta are calculated according to the standard SFA method [93], i.e. neglecting the Coulomb force. Next, these saddle points provide the initial conditions for complex electron trajectories that are propagated under the influence of both the Coulomb and the laser field. The final momenta $\mathbf{p}$ are collected with a binning method. A detailed description of this method is given in references [56, 85]. Unless mentioned otherwise, the CCSFA calculations presented below are results for ionization from a single cycle out of a flat-top laser pulse.

5.3 Scaling with Intensity, Wavelength and Pulse duration

Figure 5.1 reports a series of measurements that were obtained for ionization of the metastable xenon atoms by 7 µm FEL radiation. By varying the position of the spectrometer along the propagation direction of the laser beam, the intensity could be varied between $1.9 \cdot 10^{11}$ W/cm^2 and $7.1 \cdot 10^{11}$ W/cm^2. The intensity was retrieved from the value of the $2U_p$ cut-off, where $U_p = I/\omega^2$ is the energy of an electron oscillating in the laser-electric field, with intensity I and frequency ω. The maximum energy an electron can acquire without scattering is $2U_p$ [36]. In Figure 5.1a, the experimentally obtained momentum map is shown for the highest intensity. The image shows a dominant photoelectron emission along the laser polarization, accompanied by a series of well-resolved side-lobes, marked by white dashed lines. These side-lobes are identified as holographic interference structures and are well reproduced by the CCSFA and gSFA calculations (Figures 5.1b and c). Without including the long range Coulomb interaction (gSFA), the fringe spacing is overestimated by a factor of two, while including the long range Coulomb interaction (CCSFA) this is reduced to about 10% for this case. Furthermore, in

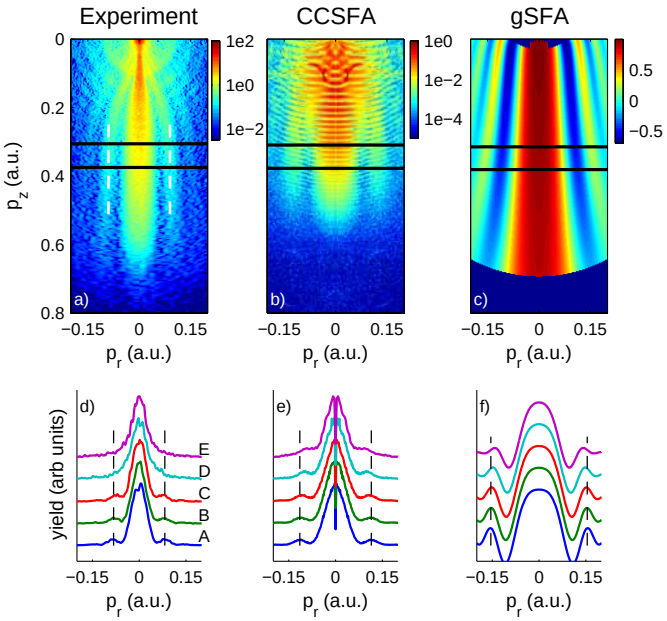

FIGURE 5.1: **Scaling of photoelectron holography with intensity.** The top panel gives momentum maps for respectively the experimental data, CCSFA and gSFA calculations at $\lambda = 7$ µm and $I = 7.1 \cdot 10^{11}$ W/cm^2, which corresponds to the measurement presented in Figures 3.3a and 3.4a. The bottom panel shows line-outs taken at constant p_z for different intensities: A. $I = 7.1 \cdot 10^{11}$ W/cm^2, B. $I = 5.5 \cdot 10^{11}$ W/cm^2, C. $I = 4.5 \cdot 10^{11}$ W/cm^2, D. $I = 3.2 \cdot 10^{11}$ W/cm^2, E. $I = 1.9 \cdot 10^{11}$ W/cm^2. The line-outs are marked by black lines in the figures in the top panel, and are taken at $[0.5p_z^{\text{cut-off}}]$, where the $p_z^{\text{cut-off}}$ corresponds to the $2U_p$ cut-off in energy. For the conditions shown in the top-panel, $2U_p$ is at a momentum of approximately 0.7 a.u.

the gSFA calculations the fringes widen towards higher parallel momenta, while in the experiment and in the CCSFA calculation the fringes are parallel to the polarization axis at high momentum. The black lines in the momentum maps mark areas over which a series of line-outs are taken, which are shown in Figure 5.1d. Upon decreasing the intensity from $7.1 \cdot 10^{11}$ W/cm^2 to $4.5 \cdot 10^{11}$ W/cm^2, the fringe spacing remains virtually unchanged. At lower intensities the fringes are not resolved anymore in the experimental data, though the CCSFA and gSFA calculations show that for the lower intensities the fringe spacing starts narrowing.

A wavelength scan is presented in Figure 5.2. In Figure 5.2a a momentum map is shown for the ionization of the metastable xenon atoms by 16 µm light. Again the overestimation of the fringe spacing is less for the CCSFA method (shown in Figure 5.2b), than for the gSFA method (shown in Figure 5.2c). As the line-outs in Figures 5.2d-f show, upon changing the wavelength from 16 µm to 8 µm, the fringe spacing clearly increases.

In the experiment it was not straightforward to change the laser pulse duration while maintaining the other laser parameters constant. Therefore the evolution of

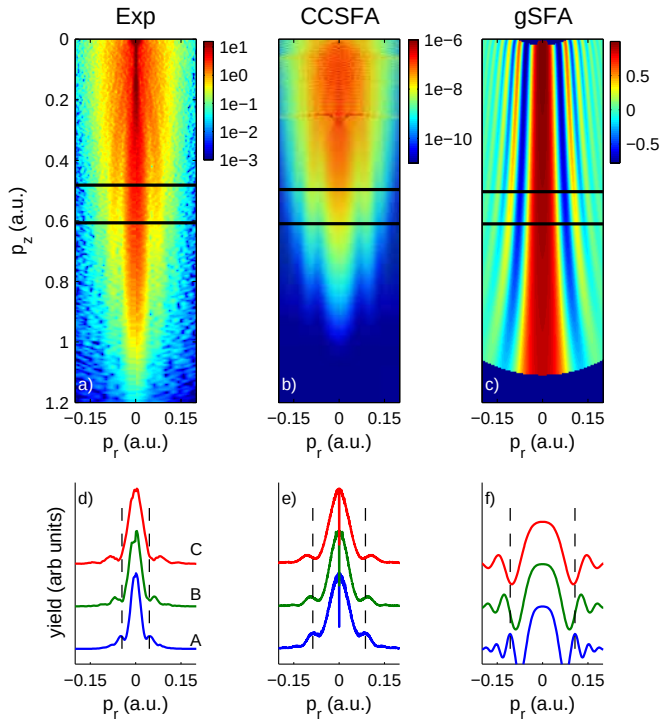

FIGURE 5.2: **Scaling of photoelectron holography with wavelength.** The top panel gives momentum maps for respectively the experimental data, CCSFA and gSFA calculations at $\lambda = 16$ µm and $I = 3.4 \cdot 10^{11}$ W/cm^2. The bottom panel shows line-outs taken at constant p_z for A. $\lambda = 16$ µm and $I = 3.4 \cdot 10^{11}$ W/cm^2, B. $\lambda = 11$ µm and $I = 4.4 \cdot 10^{11}$ W/cm^2 and C. $\lambda = 8$ µm and $I = 5.4 \cdot 10^{11}$ W/cm^2. The line-outs are taken at $[0.5p_z^{\text{cut-off}}]$.

the interference fringes with pulse duration is only investigated numerically using the CCSFA method. For insight into the scaling of the fringe patterns with pulse duration it is preferable to use realistic pulses. Results presented in Figure 5.3, for sine-squared laser pulses, show that the fringe spacing does not change with the pulse duration.

5.4 Analytical Interpretation of the Fringe Scaling

According to Figures 5.1, 5.2 and 5.3, the fringe-spacing is independent on the laser pulse duration, changes slightly with intensity, and changes significantly as a function of wavelength. We analyze this behavior by using the analytic expression obtained from the gSFA method. According to Equation 5.3 the interference pattern scales with $\Delta t = t_C - t_0^{\text{ref}}$. This time difference is largely caused by the time the electron spends in the continuum (Figure 5.4a). In the high intensity regime

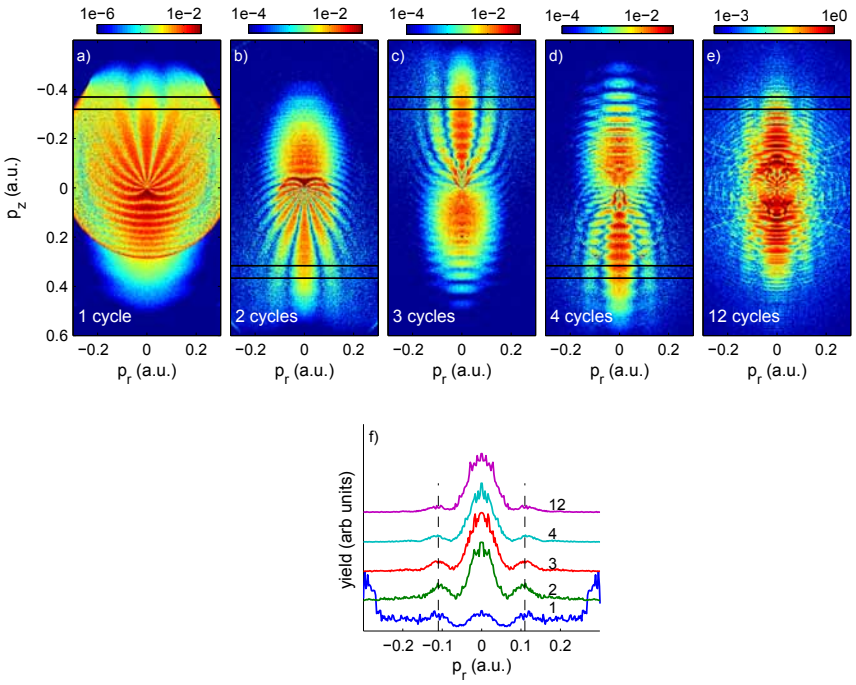

FIGURE 5.3: **Scaling of photoelectron holography with pulse duration.** The five momentum maps are CCSFA calculations for $\lambda = 7$ µm, $I = 7.1 \cdot 10^{11}$ W/cm^2 and a different number of laser cycles with a sine-square envelope of the laser-pulse. The line-outs are displayed in the bottom right figure and are taken at $[p_z^{\text{cut-off}}]$.

Δt is expected to be almost independent of the intensity since the birth (t_B) and return times (t_R) stay the same. The intensity-dependent effect is associated with the relatively small (compared to the oscillation amplitude) displacement of the electron from the origin upon tunneling, Δx. This displacement increases the time difference from t_R to t_C as $t_C - t_R = \Delta x / v(t_R)$. In the high intensity regime ($\gamma < 1$) one can easily check that this extra time scales as γ^2, while in the low intensity regime ($\gamma > 1$) it scales with $\gamma ln(2\gamma)$ where $\gamma = \sqrt{\text{IP}/2U_p}$ is the Keldysh parameter and IP the ionization potential. Consequently, the contribution associated with tunneling is low for high intensities ($\gamma < 1$) and no substantial scaling with intensity is expected in this regime. For lower intensities the extra time becomes substantial and due to the increased value for the phase term, a modest narrowing of the fringe spacing is expected (Figure 5.4b).

To support these conclusions, the cosine of the approximate reference-versus-signal phase difference, as given by equation 5.3 and of the full phase difference as given by Equation 5.2 are compared for different intensities, $I = 3.5 \cdot 10^{11}$ W/cm^2 and $I = 7.1 \cdot 10^{11}$ W/cm^2 at a wavelength of 7 µm (Figure 5.4c). This comparison shows that the approximation made in equation 5.3 is indeed valid and confirms

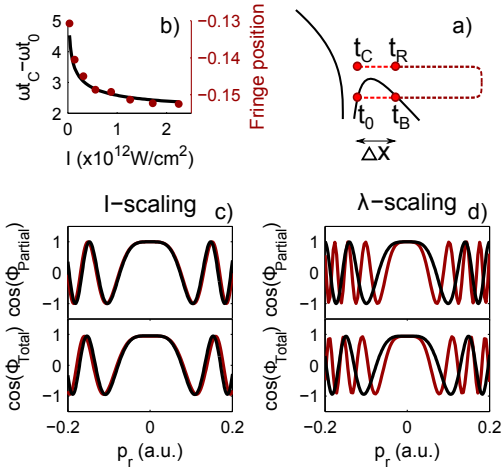

FIGURE 5.4: **gSFA calculations for photoelectron holography.** a) Tunneling and evolution of an electron wave packet in a laser field, illustrating the time the electron enters the barrier (t_0), exits the barrier (t_B), returns to the exit point (t_R) and scatters (t_C). b) Scaling with intensity of the difference $\omega\Delta t = \omega(t_C - t_0)$ for $\omega = 0.0065 a.u.$ ($\lambda =$ 7 µm) (black line). The phase difference $\omega\Delta t$ is taken for a birth time of the electron at a phase of 0.3π in $A = A_0 sin(\omega t_B)$. With increasing intensity, $\omega\Delta t$ reaches an asymptotic value. In blue dots the fringe positions are shown, which depend on $\omega\Delta t$. c) The cosine of the approximated phase difference ($\phi_{Partial}$) and the total phase difference (ϕ_{Total}) as described by equations 5.3 and 5.2 in the text, for intensities of $7.1 \cdot 10^{11}$ W/cm^2 (blue) and $3.6 \cdot 10^{11}$ W/cm^2 (black). d) Same as figure c), but now for different wavelengths; 8 µm (black) and 16 µm (blue).

that in this intensity regime the fringe spacing barely changes with the laser intensity. The weak dependence of the fringe spacing with intensity agrees well with the observations in Figure 5.1 and explains why the hologram is visible in experiments where a range of intensities in the focus are sampled.

If instead the wavelength is varied, Δt does change. When the wavelength is doubled, the time between ionization and re-collision is doubled and consequently the cosine of the phase difference changes twice as fast. With this, the fringe spacing narrows, as shown in Figure 5.4d, where the cosine of the approximate phase difference and of the total phase difference is shown for wavelengths of 8 µm and 16 µm and an intensity of $7.1 \cdot 10^{11}$ W/cm^2. Again the approximate phase difference deviates marginally from the full phase difference, justifying the approximation made. The evolution with wavelength shown is in agreement with the experimental and theoretical observations in Figure 5.2.

No significant changes are observed when the pulse duration is varied, except for other interference structures that become more prominent when the number of cycles increases. Since the electron wave packets that form the holographic pattern are generated within one and the same quarter-cycle, indeed no changes in the fringe spacing are expected.

5.5 Conclusion

In conclusion, we have demonstrated that the photoelectron holograms that result from strong-field ionization are clearly visible for a wide range of parameters in the mid-IR wavelength regime. With both the CCSFA and gSFA method the fringes of the holograms could be reproduced as well as the observed scaling of fringes with intensity, wavelength and pulse duration. Furthermore it is possible to explain the origin of this scaling with the simple and fast gSFA method. The more sophisticated CCSFA method improves on gSFA by including the long range Coulomb force, which results in a better agreement of the fringe spacing and shape with the experimental data.

The spatial and temporal information stored in the hologram is potentially very valuable, and may allow the development of novel probes of atomic and molecular dynamics. The next challenge is to retrieve this information. This should be tackled in a combined theoretical and experimental approach. Since the present gSFA gives good analytical insight it can be used as a first step. More sophisticated models, like CCSFA or an improved gSFA model that includes the long-range tail of the scattering potential could be used to fine tune this investigation. Experimentally, the next goal would be to adapt the conditions under which the holograms are obtained to the temporal and spatial structures of interest. For example, in applying strong field photoelectron holography to time-resolve molecular dynamics, it will be of interest to scale the laser intensity and wavelength to approximately 10^{14} W/cm^2 and 3 µm, respectively, so that (i) the ionization of ground-state orbitals of small molecules becomes possible, and (ii) photoelectrons with several hundred eV of kinetic energy are produced, which can diffract off and encode the molecular structure.

6 Criteria for the observation of strong field photoelectron holography

Photoelectron holography is studied experimentally and computationally using the ionization of ground-state xenon atoms by intense near-infrared radiation. A strong dependence of the occurrence of the holographic pattern on the laser wavelength and intensity is observed, and it is shown that the observation of the hologram requires that the ponderomotive energy U_p is substantially larger than the photon energy. The holographic interference is therefore favored by longer wavelengths and higher laser intensities. Our results indicate that the tunneling regime is not a necessary condition for the observation of the holographic pattern, which can be observed under the conditions formally attributed to the multiphoton regime.

6.1 Introduction

Ionization of atoms or molecules in a strong laser field leads to the emission of coherent electron wave packets that propagate in the combined Coulomb and laser field. Electrons that are ionized at different times within the laser pulse and that eventually acquire the same final momentum, give rise to interference. The first observation of photoelectron interference was in the well-known phenomenon of above-threshold ionization (ATI) [33]. In the time domain, ATI originates from the interference of electron wave packets emitted from the atom at time intervals separated by the optical period of the laser. In the energy domain ATI is commonly considered as a result of the absorption by the atom of a number of photons in excess of the minimum required to reach the ionization threshold, with a corresponding photoelectron spectrum containing peaks separated by the energy of a single photon.

Another type of photoelectron interference was observed with few-cycle carrier-envelope phase stabilized laser pulses [49, 50]. The propagation of electron wave packets launched in adjacent half-cycles at the same, but opposite value of the laser electric field (and, hence, at the same value of the vector potential $[A(t) = \int E(t)dt]$) leads to the emergence of pairs of electron trajectories that start on opposite sides of the ion and that either go to the detector directly or after turning around under the influence of the laser field. This interference can be considered as a time double-slit interference [47], which produces structures in the photoelectron energy spectrum that are qualitatively different from the regular ATI peaks

observed with longer pulses. Ionization at the positive or negative peak of the laser electric field (where the ionization rate is maximal, and where the $A(t) = 0$) leads to the creation of electrons that acquire only a very small momentum under the influence of the laser field. Influenced by the long-range Coulomb interaction, the interference of these electron wave packets, which are ionized at time-intervals corresponding to half the optical period of the laser, leads to a radial pattern in the electron momentum distribution below the first ATI order [41, 60, 94], which persists also for long pulses containing many cycles.

Recently, another type of photoelectron interference was reported, which originates from the interference of electron wave packets born within the same quarter-cycle of the laser pulse [56]. In this case the interference arises from two trajectories that start on the same side of the ion and that interact with the ionic potential, however in a quantitatively drastically different way. One trajectory undergoes strong Coulomb focusing and passes close to the ion, whereas the other trajectory is only weakly affected by the Coulomb field and makes a wide turn around the ion. The resulting interference pattern contains fringes in the electron angular distributions and can be considered as a hologram of the scattering potential. The first results reported on the observation of these holographic patterns in photoelectron imaging spectroscopy were obtained under very specific conditions. The experiment was performed on metastable (6s) xenon atoms that were ionized with 7 µm mid-infrared free-electron laser (FEL) radiation. The combination of long-wavelength radiation with the low binding energy of the ionized atom provided very favorable conditions for the observation of the hologram. Furthermore, the importance of ionization in the tunneling regime for the appearance of the holographic pattern was assumed. The required and sufficient conditions for the observation of a photoelectron hologram were not yet investigated in this work.

Here we explore photoelectron holography over a broad range of laser parameters, by varying the laser intensity and wavelength and thereby encompassing both the tunneling and multiphoton regimes of ionization. We present experimental observations for the strong-field ionization of xenon atoms in the ground state with near-infrared radiation in the wavelength range between 600 and 800 nm and between 1200 and 1600 nm. These experimental results are quantitatively compared with the results of calculations solving the time-dependent Schrödinger equation (TDSE), with a full integration over the laser focal volume. Extending our calculations over a significantly broader range of parameters than available in the experiments, we explore the dependence of the holographic pattern on the laser wavelength and intensity, and show that the possibility to observe the hologram exists both in the tunneling and the multiphoton regimes. An empirical criterion for the laser parameters that allow the observation of a hologram is established.

6.2 Experimental and Theoretical Methods

In the experiment, a commercial laser system consisting of an optical parametric amplifier (OPA, Coherent Opera) pumped by 1 mJ from a 1 kHz Ti:sapphire amplifier system (800 nm, 50 fs) was used. The OPA signal output provided pulses with a wavelength in the range from 1200 to 1600 nm with a FWHM of

10-15 nm. Frequency doubling of the OPA output using a BBO crystal provided pulses with a wavelength in the range from 600 to 800 nm. The central wavelength was determined with an accuracy of 2 nm using a spectrometer. The linearly polarized laser beam was focused onto a pulsed atomic beam (25 Hz) using a spherical normal-incidence silver mirror ($f = 75$ mm). The ejected electrons were detected using a velocity map imaging (VMI) spectrometer [64], consisting of a set of acceleration electrodes, a flight tube, a dual multichannel plate (MCP), and a phosphor screen. Images were recorded using a computer-controlled CCD camera. Retrieval of the velocity and angular distribution of the measured photoelectrons was performed by using an iterative inverse Abel transform procedure of [81]. Slices through the three-dimensional (3D) velocity and angular distribution of the ionized electrons are referred to in the following as momentum maps.

Experimental images were obtained by summing the electron yield over 5 min of acquisition time. In order to explore the evolution of the momentum maps with the laser wavelength, photoelectron momentum maps were recorded in xenon over a range of wavelengths from 1200-1600 nm, and from 600-800 nm, while attempting to keep the laser intensity constant using the observation of the ratio of double-to-single ionization in an ion time-of-flight measurement as a rough indicator. In the analysis the experimental intensities were deduced by comparing the measured results to numerical solutions of the 3D TDSE within the single-active electron (SAE) approximation [95], i.e., considering only the response of the outermost valence electron to the laser field. In order to solve the TDSE for xenon we used a code based on the method outlined in [66, 69] with a pseudo-potential described in [67]. The code provides energy-resolved electron angular distributions [68], which can be converted into a two-dimensional (2D) momentum map that allows comparison with the experimentally recorded images. For an adequate comparison to the experiment, the results of the TDSE calculations were integrated over the laser focal volume with the assumption of a Gaussian beam profile and a width of the target beam much smaller than the Rayleigh range [71]. The temporal profile of the laser pulse was modeled with a sine-squared envelope typically containing 20 optical cycles. In our discussion, atomic units ($e = m_e = \hbar = 1$) will be used throughout, unless mentioned otherwise.

6.3 Results and Discussion

Figures 6.1 and 6.2 show a series of momentum maps at wavelengths from 1200-1600 nm and from 600-800 nm, where experimental images presented on the left are compared to TDSE results on the right. The peak laser intensity used in the calculations was chosen to provide the best agreement with the experimental data (based on visual inspection) and remained on average around 3-6$\cdot 10^{13}$ W/cm^2 with an estimated error of less than 5% in the individual intensities. These experimental conditions are in the multiphoton regime for the 600-800 nm results and correspond to the transition region between the multiphoton and the tunneling regime for the 1200-1600 nm results, where we make use of the convention to define the transition between the multiphoton and tunneling regimes as the point where the Keldysh parameter $\gamma = \sqrt{\mathrm{IP}/2U_p} \approx 1$, where IP is the ionization po-

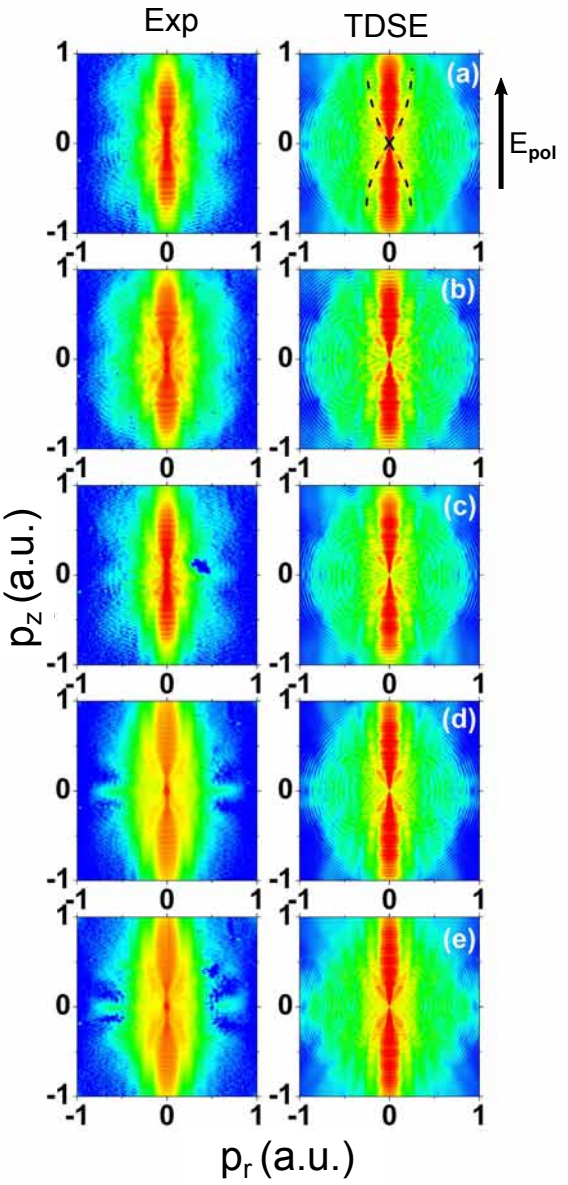

FIGURE 6.1: Experimental (left column) and calculated (right column) momentum maps for ionization of xenon at various wavelengths and intensities: (a) 1200 nm, $4.3 \cdot 10^{13}$ W/cm^2, $\gamma = 1.03$; (b) 1300 nm, $4.2 \cdot 10^{13}$ W/cm^2, $\gamma = 0.96$; (c) 1375 nm, $3.1 \cdot 10^{13}$ W/cm^2, $\gamma = 1.05$; (d) 1475 nm, $3.3 \cdot 10^{13}$ W/cm^2, $\gamma = 0.94$; and (e) 1575 nm, $3.4 \cdot 10^{13}$ W/cm^2, $\gamma = 0.87$. The logarithmic false-color scale covers three orders of magnitude. The holographic pattern is marked in (a) with a black dashed line.

tential and $U_p = F_0^2/4\omega^2$ is the electron ponderomotive energy in a laser field with the amplitude F_0 and frequency ω. The dominant contribution peaking along the laser polarization axis in the momentum maps presented in Figures 6.1 and 6.2 corresponds to ATI [33]. Away from the laser polarization axis the photoelectron momentum maps in Figures 6.1 and 6.2 show a significant qualitative difference. At the infrared wavelengths between 1200 and 1600 nm (Figure 6.1), the momentum maps are dominated by crosslike side-lobes extending from the center of the image and marked with a black dashed line in Figure 6.1a. These side-lobes are qualitatively similar to the holographic patterns observed in [56] and can be attributed to the interference of electron wave packets originating from the same quarter-cycle of the laser pulse. In contrast, the holographic pattern is absent in the momentum maps at the visible wavelengths between 600 and 800 nm (Figure 6.2). The qualitative difference between the photoelectron momentum maps at the visible and the infrared wavelengths raises the question what the criteria are for the observation of strong-field photoelectron holography. In order to explore this question the evolution of the holographic pattern with the laser wavelength and intensity will be analyzed on the basis of computational results that are in good agreement with the experiment, but that can be studied over a wider range of parameters than is accessible in the experiment.

Extending the experimentally available wavelength range, Figure 6.3 shows a series of calculated momentum maps at various laser wavelengths between 4560 and 400 nm and at a constant value of the ponderomotive energy $U_p = 0.2$ a.u. (5.44 eV), corresponding to a Keldysh parameter $\gamma \approx 1$. In order to quantify the visibility of the holographic pattern, we introduce a parameter $R = I_{\min}/I_{\max}$, where $I_{\min}$ and $I_{\max}$ are the first minimum and maximum encountered in the p_r momentum distribution when going away from the laser polarization at a constant $p_z = \frac{1}{2}p_{y_{\text{cut-off}}}$, with $p_{z_{\text{cut-off}}} = 2\sqrt{U_p}$ being the momentum corresponding to the $2U_p$ cut-off in energy. In the following a holographic pattern is considered visible when $R < 0.85$. The holographic pattern is clearly visible at the long laser wavelengths (Figures 6.3a, b) and gradually washes out towards the shorter wavelengths. In this intensity regime a hint of the holographic pattern can still be identified at wavelengths as short as 650 nm.

Our results indicate that the appearance of the holographic interference is strongly dependent on the laser wavelength range considered. On the other hand, the range of wavelengths where the holographic interference can be observed depends on the intensity regime. This is demonstrated in Figure 6.4, which shows a series of calculated photoelectron momentum maps at a fixed wavelength of 1840 nm and at various peak intensities spanning the range of the Keldysh parameter $0.8 < \gamma < 3$. The holographic pattern is not present in the momentum maps at the lowest intensity of $0.2 \cdot 10^{13}$ W/cm^2 (Figure 6.4a), but dominates the spectra at the higher intensities (Figures 6.4b-d). The appearance of the holographic pattern at reduced laser intensities (or at reduced ponderomotive energies) requires the involvement of increasingly longer wavelengths. Note that the holographic interference reported in [56] was observed at laser intensities of $10^{11} - 10^{12}$ W/cm^2 and a wavelength of 7 µm.

Interestingly, the onset of the holographic pattern in Figure 6.4 occurs at a peak laser intensity of $1.1 \cdot 10^{13}$ W/cm^2, where the Keldysh parameter $\gamma = 1.3$,

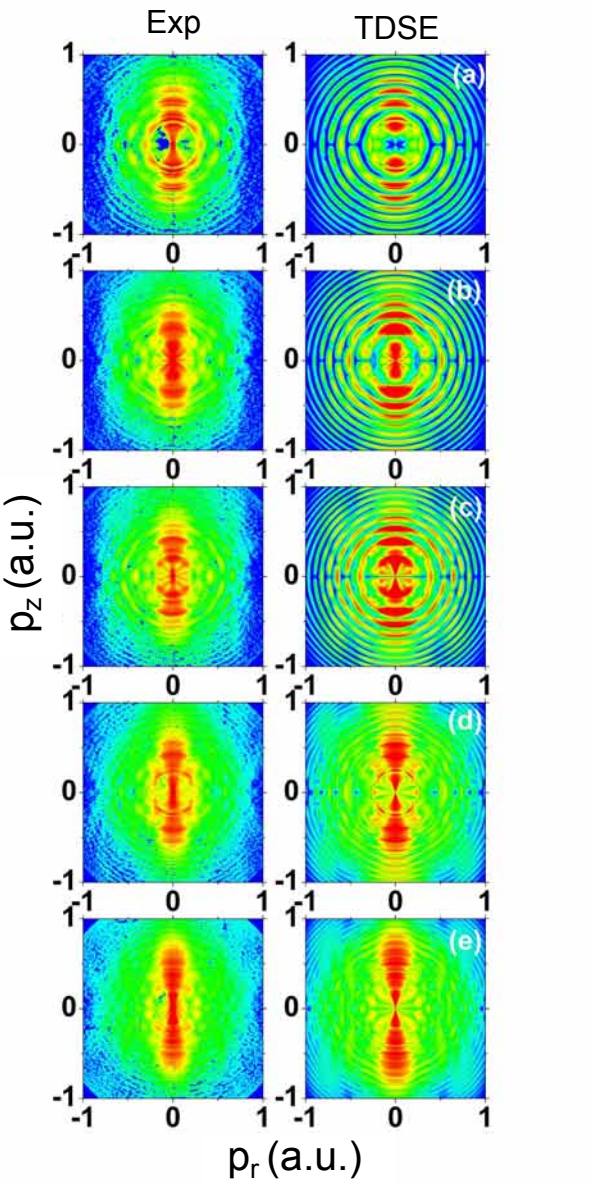

FIGURE 6.2: Experimental (left column) and calculated (right column) momentum maps for ionization of xenon at various wavelengths and intensities: (a) 600 nm, $5.7 \cdot 10^{13}$ W/cm^2, $\gamma = 1.78$; (b) 650 nm, $4.6 \cdot 10^{13}$ W/cm^2, $\gamma = 1.83$; (c) 700 nm, $4.5 \cdot 10^{13}$ W/cm^2, $\gamma = 1.72$; (d) 740 nm, $6.4 \cdot 10^{13}$ W/cm^2, $\gamma = 1.36$; and (e) 800 nm, $6.7 \cdot 10^{13}$ W/cm^2, $\gamma = 1.23$. The logarithmic false-color scale covers four orders of magnitude.

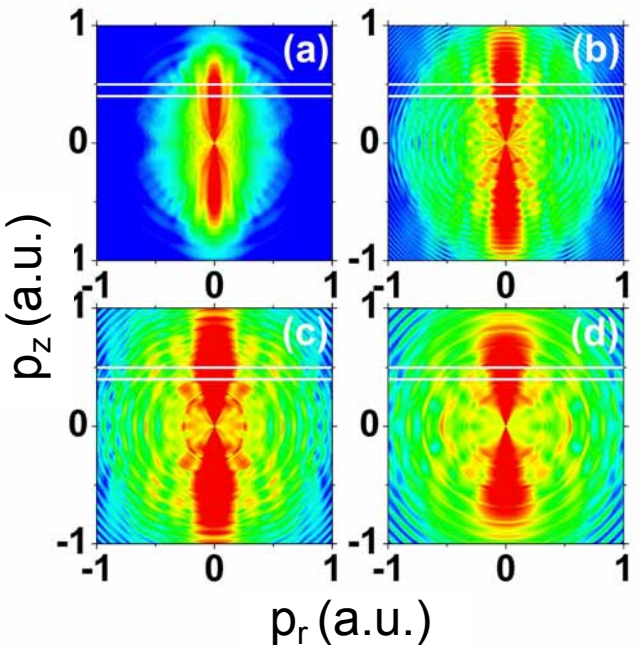

FIGURE 6.3: Calculated momentum maps for ionization of xenon at $U_p = 5.44$ eV and various wavelengths: (a) 4560 nm, $0.3 \cdot 10^{13}$ W/cm^2, R = 0.78; (b) 1140 nm, $4.5 \cdot 10^{13}$ W/cm^2, R = 0.76; (c) 650 nm, $1.4 \cdot 10^{14}$ W/cm^2, R = 0.86; and (d) 460 nm, $2.8 \cdot 10^{14}$ W/cm^2, R = 0.91. The logarithmic false-color scale covers three orders of magnitude. The horizontal white lines mark the momentum p_z where the parameter R is calculated.

i.e., at an intensity that would typically still be considered to be part of the multiphoton regime. The transition to the tunneling regime ($\gamma = 1$) at the intensity of $1.9 \cdot 10^{13}$ W/cm^2, does not cause any qualitative change to the holographic pattern. These calculations show that the holographic interference can be clearly observed in the multiphoton regime, before the formal transition to the tunneling regime. The coexistence of multiphoton and tunneling ionization mechanisms in the parameter region near $\gamma = 1$ has been discussed by Ivanov *et al.* [58]. Near $\gamma = 1$ the barrier in the combined Coulomb and laser field potential through which the electron tunnels, changes significantly during tunneling. Therefore one cannot determine unambiguously, whether multiphoton or tunneling ionization is responsible for the holographic pattern at the region where $\gamma \sim 1$.

A diagram in Figure 6.5 provides an overview of the laser parameters explored in our present experimental and computational study including computational data not shown in Figures 6.1-6.4. The filled symbols in the diagram correspond to photoelectron momentum maps where the holographic pattern can be observed, whereas open symbols indicate the absence of the pattern. A solid horizontal line

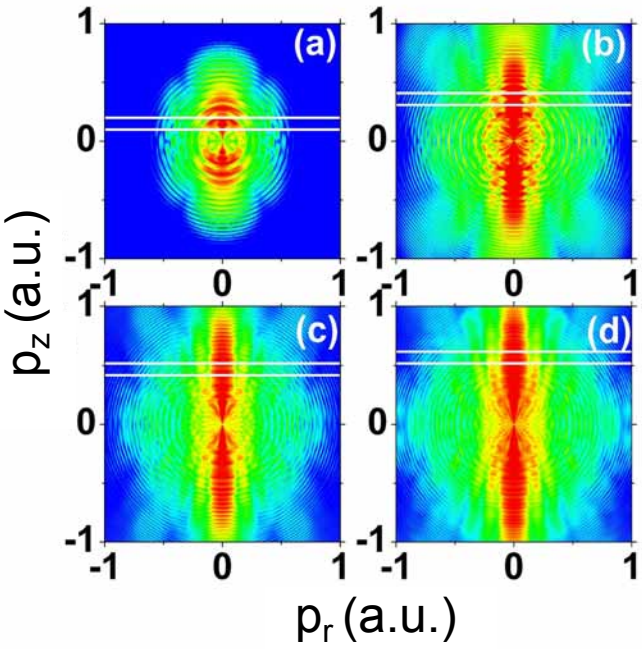

FIGURE 6.4: Calculated momentum maps for ionization of xenon at $\lambda = 1840$ nm and various intensities: (a) $0.2 \cdot 10^{13}$ W/cm^2, $\gamma = 3.1$, R = 0.89; (b) $1.1 \cdot 10^{13}$ W/cm^2, $\gamma = 1.3$, R = 0.71; (c) $1.9 \cdot 10^{13}$ W/cm^2, $\gamma = 1$, R = 0.63; and (d) $2.8 \cdot 10^{13}$ W/cm^2, $\gamma = 0.8$, R = 0.51. The logarithmic false-color scale covers three orders of magnitude. The horizontal white lines mark the momentum p_z where the parameter R is calculated.

at $U_p = 6$ eV marks the formal transition from the multiphoton to the tunneling regime, when the Keldysh parameter goes through unity. One can observe that the holographic pattern can be predominantly observed at long wavelengths in the near- to mid-infrared range (filled symbols in Figure 6.5). In this wavelength range the observation of the holographic interference requires moderate laser intensities (and moderate ponderomotive electron energies) close to the transition from the multiphoton to the tunneling regime. However, shortening of the laser wavelength leads to a gradual vanishing of the holographic pattern from the momentum maps (empty symbols).

As indicated earlier in [56] and demonstrated in the diagram in Figure 6.5 a large ponderomotive energy of the ionized electron with respect to the photon energy (i.e. $U_p/\omega \gg 1$) is a crucial requirement for the holographic interference. Consequently, the laser parameters favorable for the observation of the holographic interference tend favorably towards longer wavelengths and higher intensities. Our results confirm that generally a hologram can be clearly observed when $U_p/\omega > 4$. On one hand the dimensionless parameter U_p/ω defines the applicability of per-

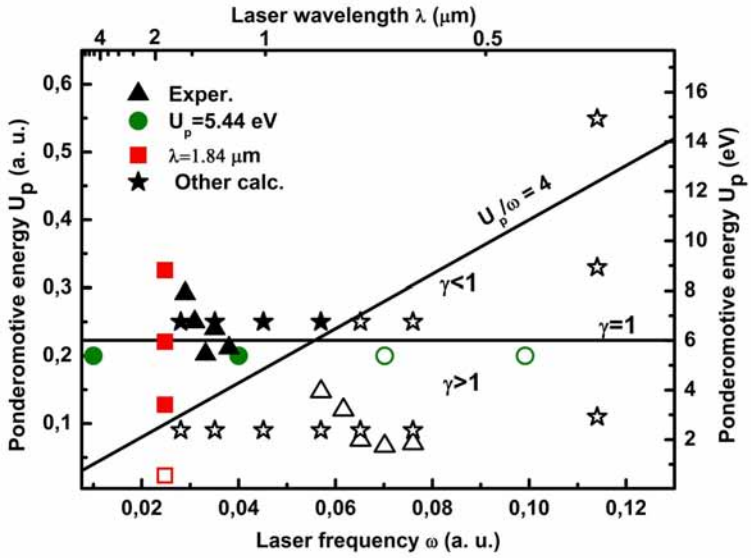

FIGURE 6.5: A diagram showing the range of laser parameters explored in this paper. The filled and empty symbols correspond, respectively, to the presence and absence of the holographic pattern in the momentum maps, shown in the previous figures. A solid horizontal line at $U_p = 6$ eV marks the formal transition from the multiphoton to the tunneling regime, when the Keldysh parameter goes through unity. Note that care must be taken with the interpretation of the results at short wavelengths and high intensity, since enhancement of intensity above the saturation of singly charged xenon ion yield may lead to depletion of the ground state before the tunneling regime can be reached.

turbation theory [92], i.e., the holograms are not observed under perturbative conditions. On the other hand U_p/ω is the number of photons required to allow an electron to be a free particle in the presence of a strong laser field [96]. Both aspects point towards the important role of the strong laser field in establishing the conditions for the observation of the hologram, which is, after all, caused by the interference between electrons that rescatter (under the influence of the laser field) and electrons that do not rescatter but that are also turned around by the laser field.

6.4 Conclusion

In conclusion, we have experimentally demonstrated photoelectron holography in ground-state xenon ionized by intense near-infrared radiation. Our calculations demonstrate a strong dependence of the holographic pattern on the laser wavelength and intensity and show that the condition $U_p/\omega \gg 1$ is crucial for the holographic interference, which therefore can be favorably observed at longer

wavelengths and higher laser intensities. Our results indicate that the tunneling regime is not a necessary condition for the observation of the holographic pattern. The signature of the holographic interference can be observed under the conditions formally attributed to the multiphoton regime ($\gamma > 1$).

7 Subcycle interference dynamics of time-resolved photoelectron holography with mid-infrared laser pulses

Time-resolved photoelectron holography from atoms using mid-infrared laser pulses is investigated by solving the corresponding time-dependent Schrödinger equation (TDSE) and a classical model, respectively. The numerical simulation of the photoelectron angular distribution of xenon irradiated by a low-frequency free-electron laser (FEL) source agrees well with the experimental results. Different types of sub-cycle interferometric structures are predicted by the classical model. Furthermore with the TDSE model it is demonstrated that the holographic pattern is sensitive to the shape of the atomic orbitals. This is a new step towards imaging by means of photoelectron holography.

7.1 Introduction

The study of electronic dynamics with long-wavelength (low-frequency) laser pulses has received increasing attention recently due to the possibility of controlling ionized electrons at high intensities, inducing control of laser-induced recollision [3, 43, 97]. Some unexpected features have been observed, such as a characteristic spike-like structure at low energy in the photoelectron energy distribution [42, 98] and a giant resonance from inner-shell electrons of xenon in HHG [99]. It has also been shown that a photoelectron holography [52, 56] pattern that contains extensive time-resolved information can be clearly recorded with mid-infrared laser fields. As illustrated in Figure 7.1, the photoelectron holography pattern comes from the interference between scattered and unscattered electron trajectories [77]. The holography encodes temporal and spatial information about both the core and the recollision electrons [56]. It is a sub-cycle interference phenomenon [47, 49, 50, 52, 56] due to the sub-cycle timescale of recollision event [3, 97]. The unscattered electrons can be viewed as a reference, which encodes the information of the initial state, whereas the scattered electrons can be seen as a signal, which contains the information of the scattering core. For short-wavelength laser fields, this holography pattern may be less clear due to the influence of the core on the reference wave. Huismans *et al.* [56] have recently recorded clear holographic pictures by using a mid-infrared free electron laser (FEL) source. When the electron is tunnel ionized by the low-frequency laser field [3], it will appear at some distance from the core. Thus the influence of the core on the reference wave will be greatly reduced. In this paper, we explore the dynamics of photoelec-

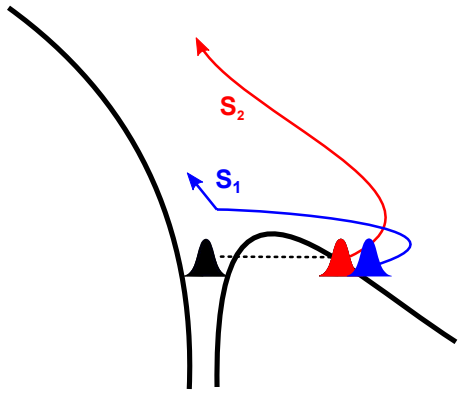

FIGURE 7.1: Schematic illustration of interference trajectories in photoelectron holography. Trajectory S_1: after tunnel ionization, the electron is accelerated in the laser field, then driven back and scattered by the core. Trajectory S_2: the ionized electron oscillates in the laser field without being scattered.

tron holography by investigating the above-threshold ionization (ATI) of xenon and hydrogen atoms in mid-infrared laser pulses numerically. A simulation that is based on solving the corresponding time-dependent Schrödinger equation (TDSE) agrees well with the experimental results. The sub-cycle dynamics of interference in ATI is further studied by a classical model which reproduces the observed interference patterns well. In addition, the possible observation of several sub-cycle interference patterns is predicted. Furthermore, based on comparing TDSE calculations for different initial orbitals, we conclude that photoelectron holography can give information on atomic orbitals [16]. This Chapter is organized as follows. We briefly introduce the numerical method for solving the TDSE in section 7.2; the classical model to investigate the sub-cycle dynamics is presented in section 7.3. The state dependent holography of hydrogen is shown in section 7.4. The conclusion is in section 7.5.

7.2 Holography by full quantum simulations

7.2.1 Theoretical method for TDSE

For numerically solving the TDSE, it was shown previously that the velocity gauge is the preferred gauge as it greatly reduces the total angular momentum number $L_{\max}$ compared to the length gauge [100]. Thus we solve the TDSE in the velocity gauge (atomic units (a.u.) $e = m = \hbar = 1$ are used throughout unless otherwise stated),

$$i\frac{\partial}{\partial t}\Psi(\mathbf{r},t) = \left[-\frac{1}{2}\mathbf{p}^2 + V_e(\mathbf{r}) - \mathbf{A}(t)\cdot\mathbf{p}\right]\Psi(\mathbf{r},t). \tag{7.1}$$

For the hydrogen atom, the potential $V_e(r) = -1/r$. For xenon, we use the form of an effective model potential $V_e(r)$ [101][102] in the single-active-electron (SAE)

approximation to describe both the atomic structure of the bare atom and the rescattering properties of the ion core:

$$V_e(r) = -(1 + a_1 \exp^{-a_2 r} + a_3 r \exp^{-a_4 r} + a_5 \exp^{-a_6 r})/r, \tag{7.2}$$

with $a_1 = 51.356$, $a_2 = 2.112$, $a_3 = -99.927$, $a_4 = 3.737$, $a_5 = 1.644$, and $a_6 = 0.431$. Spin-orbit coupling is neglected. The calculated ionization potential energies I_p from the ground state $5p$ and the first excited state $6s$ are 12.1 eV and 3.9 eV, respectively, and agree well with the ionization energies of $5p[^1S]_{J=0}$ (12.1 eV) and $6s[^2P_{3/2}]_{J=2}$ (3.8 eV) [103].

We use a cosine square function to represent the temporal profile of the laser pulse. Assuming that the polarization of the laser field is along the z axis, the field vector potential reads:

$$\mathbf{A}(t) = \frac{E_0}{\omega} \cos^2(\frac{\pi t}{\tau}) \sin(\omega t + \delta)\mathbf{e}_z, \tag{7.3}$$

where τ is the total duration of the pulse, ω is the angular frequency, E_0 is the amplitude, and δ is the carrier-envelop phase (CEP). The resulting electric field $E(t) = -\frac{\partial \mathbf{A}}{\partial t}$ satisfies the total zero area $\int E(t)dt = 0$.

For the accurate calculation of ATI, direct TDSE simulation is still a challenging problem. The kinetic energy of a scattered electron can be as high as $10U_p$, where U_p is known as the ponderomotive energy $U_p = E_0^2/4\omega^2$. In mid-infrared laser pulses, U_p (which scales with λ^2) can reach appreciable values. In addition, the total time duration $\tau \propto \lambda$, and high angular momenta l must be included. An ATI spectrum converged up to $10U_p$ requires a radius $r_{max} = 0.55\tau\sqrt{2 \times 10U_p}$ [104]. As a result, for the same number of laser cycles and laser intensities, the computation demand for a 8 μm laser field is at least 100 times larger than for a 800 nm laser field. Thus it is important to choose a flexible basis expansion in the radial direction, rather than equally distributed grid points to accurately represent the electronic wavefunction in intense mid-infrared laser fields. As described in References [104, 105], a B-spline basis is a localized basis, resulting in a sparse Hamiltonian matrix, which greatly reduces the required memory on the computer. In addition, a B-spline basis is efficient to describe the continuum states [104]. Thus we expand the time-dependent wavefunction by a radial basis of B splines and an angular basis of spherical harmonics as:

$$\Psi(\mathbf{r}, t) = \sum_{l=0}^{Lmax} \sum_{i=1}^{N} C_i^l(t) \frac{B_i^k(r)}{r} Y_l^0(\theta, \phi), \tag{7.4}$$

where N is the number of B splines for each angular momentum l, k is the order of the B-spline basis, and $C_i^l(t)$ are time-dependent coefficients. For a linearly polarized laser field, the magnetic quantum number is conserved, which sets $m_l = 0$ in this chapter. Inserting Equation (7.4) in Equation (7.1) leads to

$$i\mathbf{S}\frac{\partial \mathbf{C}}{\partial t} = \mathbf{H}\mathbf{C}, \tag{7.5}$$

where $\mathbf{C}$ is a vector of coefficients with dimension $N_{max} = (L_{max} + 1)N$, $\mathbf{S}$ and $\mathbf{H}$ are the overlap and Hamiltonian matrices, respectively. Due to the localized B-spline basis and the orthonormality of spherical harmonics, the matrices $\mathbf{S}$ and $\mathbf{H}$

are block-banded matrices. The corresponding expressions can be found in Refs. [106, 107].

For the propagation of the time-dependent wave function $\Psi(\mathbf{r},t)$, we use the Arnoldi-Lanczos scheme [108, 109]. Defining $\mathbf{H'} = \mathbf{S}^{-1}\mathbf{H}$, the essential idea of the Arnoldi-Lanczos method is to construct the Krylov space of $\mathbf{H'}$,

$$\mathcal{K}_m(\mathbf{H'},\mathbf{C}) = \text{span}\{\mathbf{C},\mathbf{H'C},\ldots,(\mathbf{H'})^{(m-1)}\mathbf{C}\}, \tag{7.6}$$

which is generated by the Lanczos iteration. The procedure yields a matrix $\mathbf{V}$ with dimension $N_{max}\times m$, which transforms the matrix $\mathbf{H'}$ into a tridiagonal symmetric matrix $\mathbf{h}$ with a small order m. The time-dependent coefficients $\mathbf{C}(t+\Delta t)$ are obtained by the relation,

$$\mathbf{C}(t+\Delta t) = \mathbf{V}\exp(-i\Delta t\mathbf{h})\mathbf{V}^{\dagger}\mathbf{C}(t). \tag{7.7}$$

The ATI spectrum $P(E)$ can be extracted from the total time-dependent wave function $\Psi(\mathbf{r},t)$, Equation (7.4), at the end of the pulse by projection on the discretized continuum wave function $\Phi^{l}_{E_k}(r)$ obtained by diagonalization of the field-free Hamiltonian,

$$\frac{dP(E)}{dE} = \sum_{l=0}^{Lmax} |\langle\Phi^{l}_{E_k}(\mathbf{r})|\Psi(\mathbf{r},\tau)\rangle|^2, \tag{7.8}$$

where $\Phi^{l}_{E_k}(\mathbf{r})$ is normalized on the energy scale [104].

To calculate the photoelectron angular distribution (PAD), we compute the differential spectrum:

$$\frac{\partial P(E_k,\theta_k)}{\partial E_k \partial\theta_k} = |\langle\psi^{-}_{\mathbf{k}}(\mathbf{r})|\Psi(\mathbf{r},\tau)\rangle|^2, \tag{7.9}$$

where the Coulomb continuum wave function $\psi^{-}_{\mathbf{k}}(\mathbf{r})$ is expanded in terms of spherical harmonics:

$$\psi^{-}_{\mathbf{k}}(\mathbf{r}) = \sum_{l=0}^{Lmax} (i)^l \exp^{-i\eta_l}\Phi^{l}_{E_k}(\mathbf{r})Y^0_l(\theta_k,0), \tag{7.10}$$

where η_l is the Coulombic phase.

7.2.2 Comparison of the theoretical and experimental photoelectron momentum distribution of xenon

For the solution of the TDSE, Equation(7.1), we use the parameters: $\lambda = 7\ \mu$m and a 10-cycle time duration τ to match the experimental FEL parameters in Reference [56]. It is expected that CEP effects can be neglected for long multicycle pulses, thus we set $\delta = 0$. The maximum total angular momentum number is $L_{max} = 39$, the number of B splines for each partial wave is $N = 5000$, and the box of the radial direction is confined to $r_{max} = 4500$ a.u. The integration time step is Δt =0.048 a.u., and the dimension of the reduced Krylov space is $m = 16$.

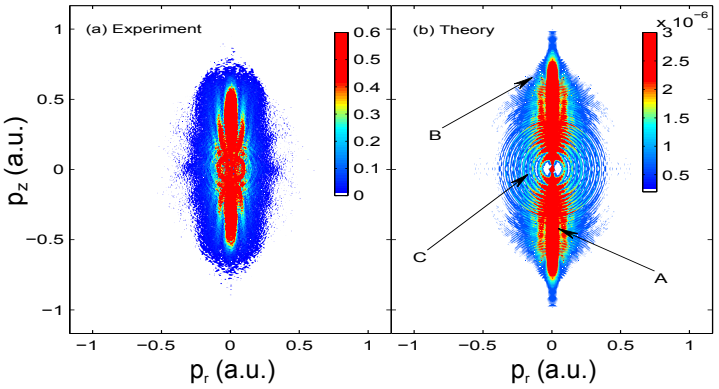

FIGURE 7.2: Comparison of experimental (a) and theoretical (b) photoelectron momentum distribution of xenon. The initial state is the metastable $6s$ state, the laser intensity is $I = 7.1 \times 10^{11}\mathrm{W/cm^2}$, and the wavelength is 7 μm, the same as shown in Figures 3.3a and 3.4a

.

In Reference [56], Huismans *et al.* measured 3D photoelectron velocity map images experimentally at different laser intensities. The initial state was the metastable $6s$ state and was prepared by means of electron impact. Figure 7.2(a) shows a slice through the experimental 3D photoelectron momentum distribution for a peak laser intensity $I = 7.1 \times 10^{11}\mathrm{W/cm^2}$. For comparison, our theoretical result is presented in Figure 7.2(b), from which we can clearly identify three different kinds of interference patterns in the momentum distribution spectrum. As illustrated in Figure 7.2(b), the interference pattern A resembles a "fork". It can be clearly identified in both theoretical simulation and experimental measurement. The interference pattern B is a set of semi-rings centered on a point in momentum space around momentum $p_z = \pm 0.7$ a.u. It is weak and therefore not possible to be identified in the experimental results. The pattern C is merely a set of outgoing rings from the center around $\mathbf{p} = 0$ a.u., which can be well resolved in both Figs. 7.2(a) and 7.2(b). It is the familiar ATI structure, corresponding to the absorption of photons in excess of the minimum number needed to reach the ionization threshold.

In Reference [56], the observed interference patterns were interpreted by using a number of theoretical approaches, which included numerical solution of the TDSE for an Ar atom, a Coulomb-corrected SFA treatment (where the influence of the Coulomb field on the signal and reference trajectories was considered) and a semi-analytical treatment that rationalized the holographic interferences in terms of the geometrical difference between the signal and reference trajectories and the interaction of the electrons with the laser electric field. Since the simulations by TDSE for argon in Chapter 3, Figure 3.4b, and xenon in this chapter agree well with the experimental results, the holography is not too much dependent on the atomic target. To further rationalize interference patterns A-C that were discussed above, in what follows we will use a simple classical model [3, 83, 97] to identify the sub-cycle interference dynamics.

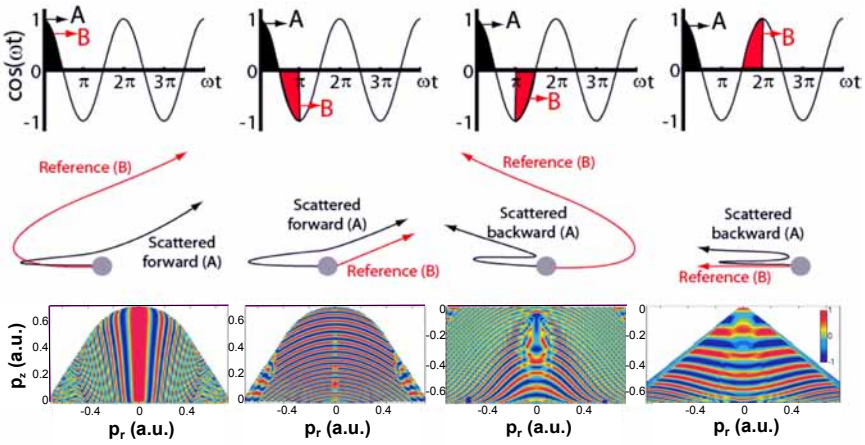

FIGURE 7.3: Sketch of different sub-cycle interference trajectories and the corresponding interferometric structures (i.e. $cos(\Delta\Phi)$). The laser parameters are the same as in Figure 7.2. In the upper panel, A stands for the signal electron, B represents the reference electron.

7.3 Holography by a classical model

The analysis of holographic structures in angular resolved ATI spectra based on application of the saddle point approach to the standard S-matrix expressions in the strong-field approximation has been performed in Chapter 4. Here we consider a simplified picture based on the classical recollision 3-step model [3, 97]. It is based on the following assumptions [3, 97]:

i)The free electron is born at distance $z_0 = \mathrm{IP}/E_0$ from the core by tunneling ionization. After ionization, we neglect the influence of the Coulomb potential due to the large z_0 and α (where $\alpha = E_0/\omega^2$ is the maximum excursion of a free electron in the laser field) for the current laser parameters. When the electron comes back to the core, it is elastically scattered.

ii)The initial velocity of the scattered electron is $v_z^{signal} = v_r^{signal} = 0$ (i.e. between ionization and re-collision the signal trajectory is along the polarization axis), while the initial velocity of the unscattered electron is $v_z^{ref} = 0, v_r^{ref} \neq 0$ (i.e. the reference electron acquires its transverse velocity during the ionization process). Due to the long excursion time between ionization and recollision, if $v_r^{signal} \neq 0$, the electron will not return to the core [3].

iii)After scattering, the velocity of the signal electron is the same as that of the reference electron. This is a condition for the observation of the interference pattern.

iv)We neglect the phase changes during the tunnel ionization and the scattering process. We further neglect multiple scattering of the signal electron by the core.

Since the laser field is polarized along the z direction, the motion of the electrons along the perpendicular direction is conserved in the laser field. In the following, we only consider the motion of electrons along the z direction. If the electron is ionized at a particular phase φ of the electric field $E(t) = E_0 \cos(\omega t + \varphi)$,

the velocity and the position of the electron can be obtained as:

$$v(t,\varphi) = \int_0^t -E(t')dt' = -\frac{E_0}{\omega}[\sin(\omega t+\varphi) - \sin(\varphi)], \tag{7.11}$$

$$z(t,\varphi) = \int_0^t v(t')dt' = \frac{E_0}{\omega^2}[\cos(\omega t+\varphi) - \cos(\varphi) + \omega\sin(\varphi)t] - z_0. \tag{7.12}$$

When the electron is driven back to the core after traveling time t_c, $z(t_c,\varphi) = 0$, and we will have a relation between t_c and φ as:

$$\cos(\omega t_c+\varphi) - \cos(\varphi) + \omega\sin(\varphi)t_c = \gamma^2/2, \tag{7.13}$$

where $\gamma = \sqrt{2\mathrm{IP}}\omega/E_0$ is the Keldysh parameter.

Next we assume that the signal electron is elastically scattered by the core at an angle θ_c. After that, the velocity in the perpendicular direction is constant as $v_r = v(t_c,\varphi)\sin(\theta_c)$. The final velocity along the z direction is:

$$v_z(t) = \int_{t_c}^t E(t')dt' = -\frac{E_0}{\omega}[\sin(\omega t) - \sin(\omega t_c)] + v(t_c,\varphi)\cos(\theta_c). \tag{7.14}$$

Here we take into account that the vector potential $A(t) = 0$ after the end of the pulse. Thus, the momentum measured at the detector is:

$$p_z = \frac{E_0}{\omega}\sin(\omega t_c) + v(t_c,\varphi)\cos(\theta_c). \tag{7.15}$$

The phase accumulated between the reference (with ionization phase φ') and scattered signal waves does not change after the recollision of the signal electron. Therefore, the time t^{ref} up to which the phase accumulation of the reference wave packet needs to be calculated is the time interval between the collision time of the signal wave packet and the ionization time for the reference wave packet. Thus in our notation $\varphi + \omega t_c = \varphi' + \omega t^{ref}$ (t_c is calculated from the ionization time of the signal wave, t^{ref} is calculated from the given formula). In addition, $v_z^{ref}(t^{ref},\varphi') = v(t_c,\varphi)\cos(\theta_c)$, $v_r^{ref} = v(t_c,\varphi)\sin(\theta_c)$.

From the above discussions, we can get the phase difference between the reference electron and the signal electron as:

$$\Delta\Phi = \int_0^{t_c}\frac{v^2(t',\varphi)}{2}dt' - \int_0^{t^{ref}}\frac{v^2(t',\varphi')}{2}dt' - \frac{v_r^2 t^{ref}}{2} - \mathrm{IP}\frac{(\varphi-\varphi')}{\omega}. \tag{7.16}$$

We discuss next the sub-cycle interference dynamics. As shown in Figure 7.3, we fix the ionization of the signal electron in the first quarter cycle with $\varphi \in [0,\pi/2]$. This electron is first ionized in the negative z-direction, and is then turned around by the laser field, so that the velocity of the signal electron arriving at the core is positive before being scattered. Next we consider the interference patterns that are generated by the interference of this signal electron in combination with a reference electron that is ejected during the same quarter cycle or one of the first three quarter cycles after this one. Though it may not be possible to

separate all these interference patterns experimentally, separate evaluation of different interfering contributions to the overall spectrum is useful, since it provides insight in the experimental results and in the TDSE calculations.

We first consider the case where the reference electron is generated in the same quarter cycle $\varphi' \in [0, \pi/2]$. The interference pattern for this case is presented in Figure 7.3(a) and agrees well with the pattern observed in Figure 7.2(b) marked as A. In Figure 7.3(b) the interference pattern is shown for a reference electron generated in the next quarter cycle with $\varphi' \in [\pi/2, \pi]$. This is a ring pattern centered at $\mathbf{p} = 0$ a.u. The velocity of the reference electron generated with $\varphi' \in [0, \pi]$ is positive when the signal electron arrives at the core, which implies that the interference patterns in Figs. 7.3(a) and 7.3(b) correspond to forward scattering interference. Although somewhat similar in appearance, the interference pattern in Figure 7.3(b) is not the usual ATI pattern (denoted C) spaced by one photon energy in Figure 7.2(b) which is produced by multiple-cycle laser pulses. Nor does it correspond to the time double-slit interference reported by Gopal *et al.* [50], which corresponds to the interference between two non-rescattering reference electrons, rather than the interference between a rescattering signal electron and a non-rescattering reference electron. A calculation of the time double-slit interference trajectories and the corresponding interferometric structures within the framework of the classical model is presented in Figure 7.4. This interference is particularly easy to understand; it arises from the interference of two wave packets ionized at instants t_1 and t_2 within the same laser cycle, for which $A(t_1) = A(t_2)$ where the laser electric field has opposite values, $E(t_1) = -E(t_2)$. That is, the two wave packets appear on the opposite sides of the ion but have the same drift momentum. In other words, the signal electron goes across the core without being rescattered. It is interesting to note that the holographic interference pattern shown in Figure 7.3(b) is a set of outgoing rings (i.e. rings with an upward curvature), while the time double-slit interference pattern presented in Figure 7.4(c) is a set of incoming rings (downward curvature).

So far we have considered the sub-cycle interference pattern in forward scattering. Now we turn to the holographic structures that appear in backward scattering. If the reference electron is generated in the third quarter cycle with $\varphi' \in [\pi, 3\pi/2]$, the interference pattern shown in Figure 7.3(c) is obtained. This pattern is a semi-ring structure centered around $p_z = -0.7$ a.u., which agrees with the pattern marked B in Figure 7.2(b). However, we cannot definitely say that the pattern B in Figure 7.2(b) is caused by the interference in Figure 7.3(c) since the time double-slit interference pattern illustrated in Figure 7.4(c) has a somewhat similar structure [47, 49, 50, 56].

If the reference electron is ionized in the fourth quarter cycle with $\varphi' \in [3\pi/2, 2\pi]$, the interference structure is presented in Figure 7.3(d). It is difficult to resolve these structures in the experimental and theoretical spectra in Figure 7.2. In the results shown in Figs. 7.3(c) and 7.3(d), the reference electron has a negative velocity whereas the signal electron arrives at the core with positive velocity. Therefore both the results in Fig 7.3(c) and Figure 7.3(d) involve backward scattering of the signal wave, which usually is weaker than the forward scattering. This is the reason why the interference patterns in Figs. 7.3(c) and 7.3(d) are difficult to be identified in the experimental results in Figure 7.2(a).

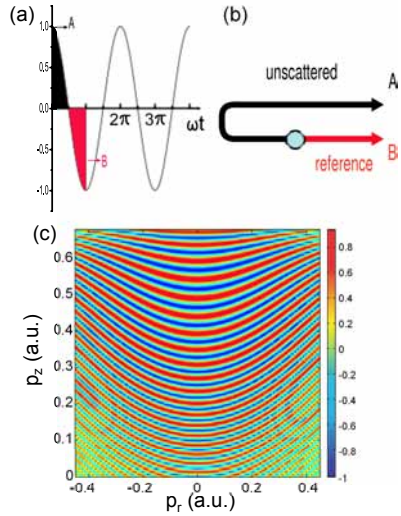

FIGURE 7.4: Sketch of time double-slit interference trajectories and the corresponding interferometric structures by the classical model. The laser parameters are the same as in Figure 7.2. A stands for the signal electron, B represents the reference electron.

7.4 Imprint of degenerate orbitals of hydrogen atom in holography

Photoelectron holographic patterns contain both time and spatial information [56]. In this light it would be interesting to investigate the possibility of resolving the shape of the atomic orbital with photoelectron holography. As described in the previous section, there are four different types of holographic interference structures, that all should carry valuable information. Realistically, however, only the interference structure described in Figure 7.3(a) will be resolvable, since it is the only interference pattern in the angular direction. All other interference patterns, including the non-holographic ones, have a pattern in the radial direction and will be hard to disentangle. From now on we therefore focus on the first interference structure and explore to what extent these interference patterns depend on the choice of initial orbital.

To reduce the influence of the tunneling time and the ionization rate of the different initial states we choose the degenerate $3s$, $3p$ and $3d$ states of hydrogen as initial states. The photoelectron momentum distributions, calculated with TDSE, are presented in Figure 7.5. Different initial orbitals indeed give rise to different holographic patterns and three types of differences can be observed; the width of the pattern, the cut-off of the pattern and the shape of the fringes. Concerning the first, for both the $3s$ and $3d$ state multiple fringes can be observed, while for the $3p$ state the second fringe is already barely visible. This can be explained by the initial distribution of the photoelectrons; the more the photoelectrons initially ionize with an orthogonal component p_r the wider the final pattern. The perpendicular momentum distribution of the unscattered photoelectrons is closely related to the initial state $\Psi(0)$ [58, 110]:

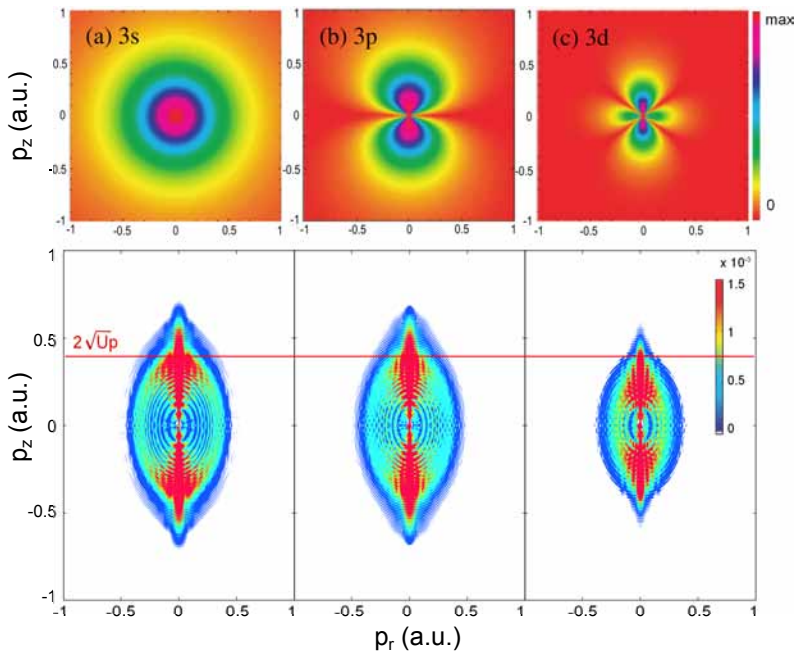

FIGURE 7.5: Atomic orbitals of hydrogen in momentum space ($|\Psi|^2$) and the corresponding photoelectron momentum distribution in a laser field with intensity $I = 1.775 \times 10^{11}\mathrm{W/cm}^2$, and wavelength 7 μm. The initial state is: (a) $3s$, (b) $3p$, (c) $3d$, respectively (all with $m = 0$). The red line corresponds to the cutoff momentum of the directly ionized electrons.

$$\Psi(p_r) = \Psi(0) \exp\left[-\frac{p_r^2 \tau_0}{2}\right], \tag{7.17}$$

where $\tau_0 = \sqrt{2\mathrm{IP}}/E_0$ in the static limit. The shapes of the atomic orbitals in momentum space are presented in the top panel of Figure 7.5. Both the s and d state have a substantial distribution in the orthogonal direction, while for the $3p$ state there is a nodal plane perpendicular to the z-axis with $p_z = 0$ a.u. Consequently the reference photoelectrons ionized in the perpendicular direction are suppressed giving rise to a narrower distribution of the holographic pattern.

The second observation is the lower momentum cutoff in the interference pattern for the $3d$ orbital as compared to $3s$ and $3p$ orbitals. The cutoff energy of the directly ionized electron is $2U_p$, which restricts the holographic pattern below $2\sqrt{U_p}$ in momentum space. Photoelectrons with higher energy up to $10U_p$ can also be obtained by backscattering [83]. A possible explanation for the lower cutoff of $3d$ orbitals could be related to the effective potential $\frac{l(l+1)}{2r^2} - \frac{1}{r}$, which is strongly dependent on l. High angular momentum changes the shape of the tunneling wave packet and the tunneling rate [111]. The ionization rate of electrons from $3d$ orbitals with higher energy decreases compared to electrons from $3s$ and $3p$ orbitals. The momentum distribution of electrons from $3s$ and $3p$ states

extends beyond $2\sqrt{U_p}$, which corresponds to a stronger recollision signal. However, the recollision is suppressed for the $3d$ state due to the centrifugal potential (preventing the return).

The third and maybe most important observation is the shape of the fringes itself. While for $3s$ they are parallel to the main lobe, for $3p$ they bend together at higher momenta and for $3d$ they diverge. A possible explanation is the different short range potentials altering the phase of the scattering wave packets in a different way for the three atomic orbitals. This would imply that it is possible to map the atomic orbital [16, 53] with photoelectron holography.

The observation and analysis so far are qualitative, but the TDSE calculations do show that the atomic orbitals have an imprint on the final pattern. It would be very interesting to investigate the possibility to (time-resolve) atomic orbitals with photoelectron holography.

7.5 Conclusion

In summary, we present and compare accurate numerical methods to calculate ATI spectra of atoms in mid-infrared laser pulses. The simulations agree well with current experimental results performed with a FEL source. A simple classical model is proposed to interpret the sub-cycle interference patterns obtained. To our knowledge, the sub-cycle interference patterns shown in Figure 7.3(b-d) are not reported previously. We have demonstrated that all sub-cycle interferences give a pattern in the radial direction except for the holographic pattern created by electron wave packets generated in the same quarter cycle. This allows to disentangle this holographic pattern from other interference structures and investigate the time and spatial information stored in the hologram. TDSE-calculations show that this holographic pattern is sensitive to the degenerate $3s$, $3p$ and $3d$ state of the hydrogen atom, which implies that the shape of the original orbital is imprinted in the photoelectron hologram. This opens the way to investigating the possibility to do time-resolved studies of atomic and molecular orbitals with photoelectron holography. Further research may benefit from sculpting and tailoring these new pulses using control algorithms [112].

8 Macro-atom vs many-electron effects in strong field ionization of C_{60}

Ionization mechanisms of C_{60} molecules irradiated by a short intense 800 nm laser pulse are studied. Angle-resolved photoelectron spectra show above-threshold ionization (ATI) patterns with a low peak contrast and a remarkably smooth angular distribution. The results are interpreted by combining two theoretical models. A time-dependent Schrödinger equation (TDSE) calculation based on the B-spline method that explicitly takes into account the molecular potential mimics the single active electron response while a statistical model accounts for the multi-electron effects. We show that the latter are responsible for the loss of contrast in the ATI peaks. The smooth angular distribution arises in the TDSE calculation as a result of the high angular momentum of the C_{60} ground electronic state and therefore is a manifestation of the atomic behavior of the molecule.

8.1 Introduction

The interaction between an intense light pulse and a complex polyatomic molecule is an archetype of many-body problems where the light electric field interacts with the electronic degrees of freedom inducing different types of dynamics where both electrons and nuclei may play a role. Ionization is one of the possible responses and may, due to the various degrees of freedom involved, occur on different timescales. Recent progress in light sources offers the possibility to investigate this dynamics down to the attosecond timescale and to observe the electronic motions in real time [113]. This motivates current work on electronic processes in complex systems.

In atomic species, ionization by an intense laser field typically leads to above-threshold ionization (ATI), in which the atom absorbs more than the minimum number of photons required to reach the ionization threshold. Extensive work on atomic ATI, largely based on photoelectron spectroscopy, has been focused on the distinction between tunneling and multiphoton ionization [70], the role of resonances and the importance of electron interferences. This kind of information is directly encoded in the photoelectron angular distribution [56]. The case of molecules is far less investigated, but in a recent paper, Milosevic *et al.* [114] have shown that information on molecular orbitals can be obtained from angle-resolved high-order ATI of diatomic molecules. Corkum and co-workers also revealed the

importance of diffractive effects during the recollision process resulting from the structure of the molecule [55]. In the more general case of complex polyatomic species, it is unclear whether the photoelectron energy and angular distribution can provide insight into the ionization dynamics and whether such processes can be adequately described in the single active electron (SAE) picture or require one to account for the multi-electron dynamics. C_{60} can be considered as a perfect "laboratory" to investigate these questions. A large variety of dissociation and ionization processes have already been experimentally observed [115]. In a seminal article, Campbell *et al.* [116] observed the modification of the C_{60} photoelectron spectrum as a function of the laser pulse duration. These changes were attributed to the gradually increasing influence of electronic and nuclear degrees of freedom on the multiphoton excitation process when the pulse duration was varied from 25 fs to 5 ps. When using longer laser pulses, multiphoton excitation leads to an efficient delayed electron emission driven by vibrational autoionization mechanisms, as revealed by the observation of an isotropic electron angular distribution that emphasizes the stochastic nature of the emission process [117]. In the case of short (9 fs) laser pulses, measurements of the ionization yield have shown that the excitation is driven by single active electron processes [118]. However, a multi-active-electron (MAE) mechanism has been invoked to explain the observation of Rydberg excitation [119] and recent experiments [120] have shown the importance of recollision processes and doorway states when the light intensity reaches 10^{14} W/cm^2. This demonstrates that the role played by multi-electronic effects remains a central question in the understanding of the ionization of C_{60} [121, 122].

In this paper, we present an experiment in which C_{60} was ionized by a short 30 fs IR pulse, with intensities ranging from 10^{12} W/cm^2 up to 10^{14} W/cm^2 where for intensities below $5 \cdot 10^{13}$ W/cm^2 multiphoton processes dominate, while recollision induced ionization and field ionization (i.e. tunneling and/or over-the-barrier ionization) is known to be unexpected. The full three-dimensional momentum distribution of the electron was recorded with a velocity map imaging spectrometer. The measurements disentangle both novel aspects of the atomic-like ionization process that can be modeled using TDSE calculations and contributions involving electron-electron interactions that can be described by a statistical model for finite size systems.

8.2 Experimental Observation

Our experimental set-up combined a molecular beam, a velocity map imaging spectrometer and a focused, moderately intense femtosecond (fs) laser beam. The C_{60} molecular beam was produced with a ceramic oven operated at a temperature of 500 °C. The molecular beam was collimated by a 1 mm skimmer and crossed the infrared (IR) femtosecond laser beam (30 fs, 800 nm, 4 kHz) that was focused with a 20 cm lens. The two beams crossed on the axis of a velocity map imaging spectrometer designed according to the standard geometry proposed by Eppink and Parker [64]. Using this spectrometer, particles ejected with the same velocity vector are found on the same position of a position sensitive detector, which was

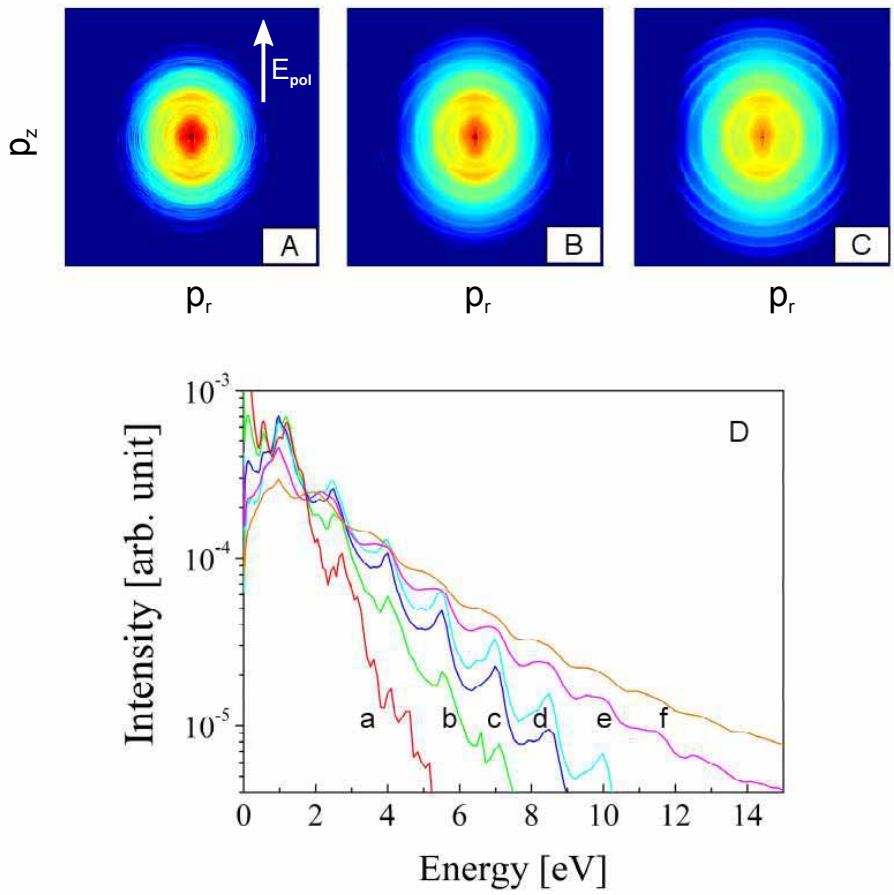

FIGURE 8.1: (A-C) Experimental photoelectron momentum maps from the ionization of C_{60} with a 30 fs, 800 nm laser pulse. The three images shown were obtained for peak intensities of $9 \cdot 10^{12}$ W/cm^2 (A), $2 \cdot 10^{13}$ W/cm^2 (B), and $2.8 \cdot 10^{13}$ W/cm^2 (C). The logarithmic color scale covers three orders of magnitude. A typical ATI pattern is observed. When the light intensity increases, the peak-to-valley contrast of the ATI peaks is reduced, as observed in the angle-integrated photoelectron spectra shown in (D). The angle-integrated photoelectron spectra are shown for intensities of a) $1.1 \cdot 10^{12}$ W/cm^2 b) $9 \cdot 10^{12}$ W/cm^2, c) $2 \cdot 10^{13}$ W/cm^2, d) $2.8 \cdot 10^{13}$ W/cm^2, e) $6.7 \cdot 10^{13}$ W/cm^2 and f) $1.0 \cdot 10^{14}$ W/cm^2.

made of a pair of 70 mm diameter micro-channel-plates (MCP) followed by a phosphor screen and a charge-coupled device (CCD) camera. The three-dimensional momentum distributions where retrieved via an iterative inverse Abel transform procedure [81]. Slices through these three-dimensional momentum distributions are referred to as momentum maps.

Typical images obtained in our experiment for peak intensities of $9 \cdot 10^{12}$ W/cm^2 to $2.8 \cdot 10^{13}$ W/cm^2 are shown in Figure 8.1A-C, along with a series of angle-

integrated photoelectron kinetic energy distributions spanning peak intensities from 10^{12} to 10^{14} W/cm^2 (Figure 8.1D). In these momentum maps, concentric rings spaced by the energy of one IR photon are observed, which is the usual signature of ATI. A smooth angular distribution is observed for every ATI ring, which becomes more peaked along the laser polarization axis when the ATI order increases. Usually, in atomic ATI, the photoelectron angular distribution is highly structured, due to the existence of Freeman resonances with high angular momentum and due to interferences between electron wave packets that are ionized at different times within a laser cycle [77]. For a complex system such as C_{60}, one might expect the high electronic density of states to be responsible for the observed smooth angular distribution. However, in the following, we will present 3D TDSE calculations adapted for C_{60} that show that the smooth angular distributions can be understood in terms of a purely atomic, single-active electron effect. Besides the ATI structure, additional structures below 1eV are observed in the angle-integrated photoelectron spectra in Figure 8.1D. These structures were previously observed and interpreted as one-photon ionization out of high-lying Rydberg states that are populated by multiphoton non-adiabatic excitation [119].

In non-resonant ATI experiments with short laser pulses, peaks are expected at energies $E_n = n\omega_{laser} - \mathrm{IP} - U_p$ (in atomic units), where ω_{laser} laser is the laser frequency, IP is the ionization potential and $Up = I_{laser}/4\omega^2_{laser}$ is the ponderomotive energy, with I_{laser} the laser intensity. Consequently, with increasing laser intensity, the ATI peaks shift towards lower energy. Beside the shift, we also observe a progressive lowering of the ATI peak energies with intensity, as well as a disappearance of the ATI structure at intensities close to 10^{14} W/cm^2. This trend is partially explained by the role of focal volume averaging, but is mostly attributed to the onset of multiple ionization at higher intensities. Neither mechanism can explain the low ATI peak contrast observed at low intensities such as $2 \cdot 10^{13}$ W/cm^2. For this intensity regime the ponderomotive peak shifts are too low to cause any significant blurring of the peaks. Below we will argue that the loss of contrast in this intensity range is due to the coexistence of direct and indirect (thermoelectronic-like) emission.

8.3 Theoretical Methods

The interaction of C_{60} with an ultra intense laser field requires consideration of the following issues. First of all, the coupling between the molecule and the laser beam occurs through the dipole interaction on a microscopic scale. This can be modeled in the SAE approximation by a TDSE calculation. However, the many-electron structure of the molecule results in a collective behavior where energy is transferred to the electronic cloud with the consequence of smearing out the single active electron aspects. This is modeled by applying statistical theory. Though negligible in our experiment, the coupling of the electrons to phonons, which leads to vibrational auto-ionization on longer time scales, is also taken into account. To account for the fact that the C_{60} molecules experience different laser intensities depending on their location in the laser beam, focal volume averaging is required in the modeling. (In the following, atomic units are used unless otherwise specified).

For each single molecule, the response to the incident laser field is calculated in the SAE approximation by solving the 3D TDSE.

$$i\frac{\partial}{\partial t}\Psi(\mathbf{r},t) = \left\{-\frac{1}{2}\nabla^2 + V_{\text{eff}}(r) - \mathbf{A}(t)\cdot\mathbf{p}\right\}\Psi(\mathbf{r},t) \tag{8.1}$$

This equation describes the spatiotemporal evolution of the electronic wavefunction experiencing an effective, spherically symmetric, one electron molecular potential $V_{\text{eff}}(r)$ and interacting with the laser field within the dipole approximation (expressed in the velocity gauge via the term $\mathbf{A}\cdot\mathbf{p}$). A B-spline method is used to solve Equation 8.1 [104]. The momentum distribution of the emitted electrons is calculated by projecting the final electronic wavefunction onto an incoming continuum wavefunction.

$$\frac{\partial^2 P}{\partial k \partial\theta_k} = \int |\langle f_k^-(\mathbf{r})|\Psi(t=\infty)\rangle|^2 d\varphi_k \tag{8.2}$$

with:

$$\langle \mathbf{r}|f_{\mathbf{k}}^-\rangle \equiv f_{\mathbf{k}}^-(\mathbf{r}) = \sum_{l,m}(i^l e^{-i\Delta_l}\phi_k^l(r)Y_{l,m}(\hat{r})Y_{l,m}^*(\theta_k,\varphi_k)) \tag{8.3}$$

where l and m denote, respectively, the angular and magnetic quantum numbers of the partial waves, $\phi_k^l(r)$ is the radial wavefunction of momentum k and $Y_{l,m}^*(\theta_k,\varphi_k)$ is the angular part. The phase shift $\Delta_l = \eta_l + \delta_l$ is the sum of the Coulomb phase $\eta_l = \arg\Gamma(l+1+iz/k)$ with $z=1$ the asymptotic charge seen by the ejected electron and δ_l, a short-range scattering phase shift. The molecular potential $V_{\text{eff}}(r)$ appearing in Equation 8.1 was obtained by a Local Density Approximation (LDA) calculation within the framework of density functional theory (DFT)[123] and the spherical jellium model. In the Kohn-Sham formulation of DFT [124], the ground-state electron density $n_e(\mathbf{r})$ of an N-electron system is written, in terms of single-particle orbitals ψ_k and energies ϵ_k, as

$$n_e(\mathbf{r}) = \sum_{k=1}^{occ}|\psi_k(\mathbf{r})|^2 \tag{8.4}$$

where *occ* is the number of occupied orbitals. These orbitals and energies obey the Schrödinger equation:

$$\left\{-\frac{1}{2}\nabla^2 + V_{\text{eff}}(r)\right\}\psi_i(\mathbf{r}) = \epsilon_i\psi_i(\mathbf{r}) \tag{8.5}$$

Where $V_{\text{eff}}(r)$ is an effective single-particle potential which is found in an iterative way following the usual DFT approach. The effective potential is given by $V_{\text{eff}}(r) = V_{\text{ext}}(r) + V_H(r) + V_{\text{xc}}(r)$, where $V_{\text{ext}}(r)$ is an external potential (e.g. due to the ionic background), $V_H(r)$ is the Hartree potential solution of Poisson's equation and $V_{\text{xc}}(r)$ is the exchange-correlation potential. Following Perdew and Zunger [125] we have added a self-interaction correction that restores the correct asymptotic behavior of the effective potential. V_{ext} was treated in the jellium approximation following the model developed by Bauer *et al.* [124]. In the latter,

the charge of the real ionic cores is replaced by a constant positive background uniformly distributed over a spherical shell. Previous studies have demonstrated [126–132] that this model is able to mimic the relevant features that are obtained by using much more sophisticated first-principle calculations [133]. The electronic states are labeled by the (l, n_r, m) quantum states standing for the angular momentum, the radial and the magnetic quantum number.

The statistical model that we use [134] was successfully applied to thermoelectronic emission from highly excited sodium clusters. In the following we briefly describe how this approach is adapted to C_{60} molecules irradiated by an intense and short laser pulse. The kinetic energy distribution of electrons emitted from $C_{60}^{i+}(i = 0, 1, ...)$ species is given by:

$$P_i(\epsilon) \propto \int_{t=0}^{\infty} N_i(t) k_i(E_i(t), \epsilon) dt \tag{8.6}$$

where ϵ is the electron kinetic energy, $N_i(t)$ is the population of C_{60}^{i+} at time t determined by solving a system of coupled first-order differential equations, $k_i(E_i(t), \epsilon)$ is the differential electron emission rate for the production of electrons with a kinetic energy ϵ from C_{60}^{i+} ions with a time dependent internal energy $E_i(t)$, and is evaluated within the framework of the statistical model proposed by Weisskopf [135]

$$k_i(E_i(t), \epsilon) = \frac{2}{\pi^2} \sigma_i(\epsilon) \epsilon \frac{\rho(E_i(t) - \mathrm{IP}_i - \epsilon)}{\rho(E_i(t))} \tag{8.7}$$

where $\sigma_i(\epsilon)$ is the classical capture cross-section of a Coulomb plus hard sphere interaction potential, IP_i the ionization potential [136], $\rho(E_i(t))$ the electronic level density which is approximated by that of an ideal Fermi gas and $E_i(t)$ the internal energy of C_{60}^{i+}.

8.4 Single Active Electron Responds

We first discuss the result of the TDSE calculation. Calculations of the ionization rates show that for $I = 2 \cdot 10^{13}$ W/cm^2 the ($l = 5$, $n_r = 1$, m) state dominates the ionization yield by several orders of magnitude over the other near-threshold orbitals ($l = 4$,$n_r = 1$, m) and ($l = 9$, $n_r = 1$, m). Therefore, we will only consider ionization of this most probable channel. Figure 8.2A shows the computed ionization rate of various $|m|$ components of the $l = 5$ state as a function of the laser intensity. Interestingly, the ionization efficiency is very similar for $|m| = 0$ and 1. Because of the two-fold m-degeneracy, the largest contribution to the ionization rate is therefore given by the $|m| = 1$ states rather than $m = 0$. This is a direct consequence of the fact that the C_{60} highest occupied molecular orbitals (HOMO) are high angular momentum states for which the wavefunction corresponding to the lowest projection of l (i.e. $|m| \ll l$) are very similar. Therefore, these states have nearly identical light-induced dipoles and display very similar ionization behavior, in contrast to the usual atomic situation, where the ground state has a low angular momentum state and $m = 0$ often dominates. Note also that contrary to

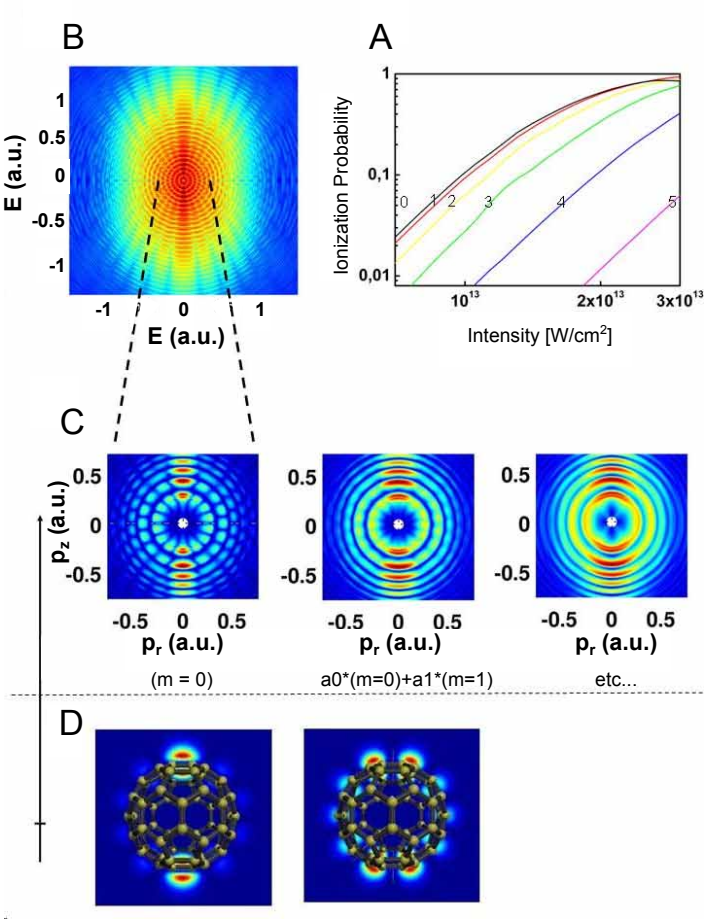

FIGURE 8.2: (A) Calculated ionization rate for (5,1,m) states showing the importance of the first m states. (B) TDSE calculation of the momentum distribution, side lobes are observed that could correspond to the interference between electron wave packets emitted within a single quarter cycle of the light pulse. (C) The electron momentum distributions for the individual ($l = 5$, m) π states, where we have successively added the contribution of all m states. The last depicted picture shows that after adding all m-state contributions, the total momentum signal where the nodal pattern completely disappeared leading to a smooth, structureless aligned angular distribution in agreement with the experimental results. (D) Calculated first individual ($l = 5$, m) π states. The dotted line between figure (C) and (D) represents the ionization threshold and the arrow the binding energy.

the atomic case the electronic structure of C_{60} is extremely dense and the plethora of excited states reached via multiphoton transitions prevents the appearance of given isolated resonances in the ATI electron spectrum.

Let us now discuss the angular distributions. In Figure 8.2B, a calculated 2D momentum distribution over a large electron kinetic energy range is presented

for a laser intensity of $2 \cdot 10^{13}$ W/cm^2 ionizing the $m = 0$ state. This momentum distribution is peaked along the polarization axis, and contains a series of side-lobes. Similar patterns were recently observed in strong-field ionization of metastable xenon atoms at mid-IR wavelengths [56], and interpreted in terms of a holographic interference between electrons that leave the atom without a strong interaction with the ion left behind and electrons that re-collide with their parent ion. The lobes that we observe persist in a single laser cycle calculation and might originate from this holographic process. Therefore, they would carry information on the molecular potential.

In figure 8.2C and 8.2D, we present the calculated 2D photoelectron momentum distributions resulting from ionization by a $2 \cdot 10^{13}$ W/cm^2 laser field and the ($l = 5$, $n_r = 1$, m) initial orbitals. The 2D momentum distribution is highly structured for each m, but the angular distributions for the different m-states are different from each other. As a result the incoherent addition of the first two m-states, taking into account the relative ionization rate, already leads to an almost structureless angular distribution (Figure 8.2C). The momentum distribution summed over all the m-projections is very smooth and becomes narrower for the high order ATI peaks, in very good agreement with the experiment. We conclude that the remarkably simple angular distributions observed in the strong field ionization of C_{60} can be modeled as atomic-like SAE ionization processes. They are caused by the accumulation of highly-structured but slightly different angular distributions from the various m-components of a single high angular momentum electronic ground state. No other effect related to the complexity of the molecule needs to be invoked.

8.5 Electron Correlation Effects

A SAE calculation does not fully describe the measurements shown in Figure 8.1. This becomes readily apparent when we compare the measured angle-integrated photoelectron spectrum and the SAE calculation in figure 8.3. While the position of the ATI peaks and their relative amplitude is relatively well reproduced by the TDSE calculation, a large difference in the peak-to-valley contrast is observed. This was previously shown by Campbell *et al.* [116, 137], and points to the presence of an electron background in the images. The origin of this background lies in a thermoelectronic emission process, where the ionization occurs from a hot electron gas. It is known that this process becomes dominant when the pulse duration reaches a few hundred femtoseconds and signifies the importance of electron-electron interactions. Statistical theories for finite size systems can be used to describe this mechanism as presented in the preceding theory section. The calculated thermal contribution to the photoelectron spectrum shows a smooth, near exponential-like, decay from which an apparent temperature can be derived. In order to disentangle the ATI and thermal emission, we use the fact that the ATI process is mostly aligned along the laser polarization axis while the purely thermal emission is isotropic. Therefore, the thermal contribution can be obtained by considering the photoemission that occurs at ninety degrees with respect to the laser polarization where the ATI contribution is expected to be

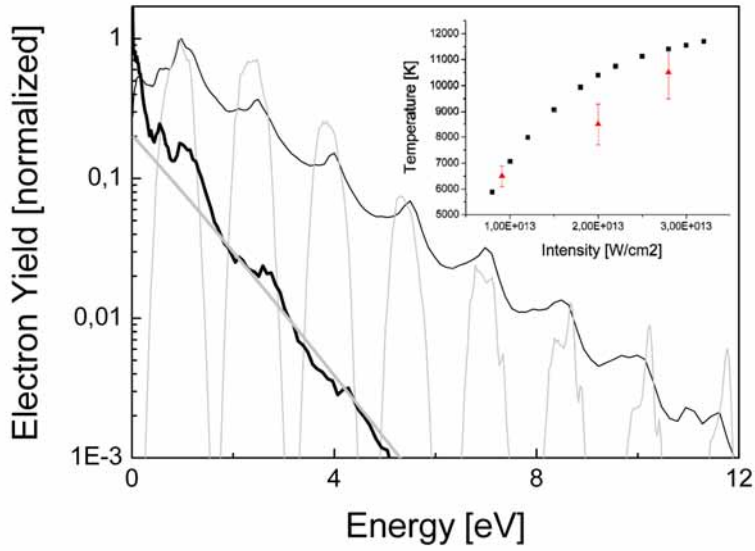

FIGURE 8.3: **Comparison between experimental and calculated electron spectra.** The TDSE calculation predicts a high contrast of the ATI peaks (thin grey curve). The loss of contrast observed in the experimental data (thin black curve) is attributed to electron-electron interaction. A thermal calculation (solid grey curve) leads to good agreement with the experimental background measured at ninety degrees with respect to the laser polarization (solid black curve). In the Inset the comparison between calculated temperature (black square) and temperature extracted at 90 degrees from the velocity distribution (red triangles) is shown.

minimal. Experimental temperatures were then obtained by a fitting procedure, which can be compared to theoretical values following from the statistical model. This comparison is shown in the inset of Figure 8.3 for several laser intensities. In previous experiments [116, 138] the temperature extracted from the angle integrated electron kinetic energy spectra was substantially higher than the one that can be predicted by Weisskopf theory. In our experiment, the angular resolved measurements allow to disentangle the ATI and thermal processes. This leads to a more accurate experimental estimation of the temperature and to a much better agreement with Weisskopf theory, especially if focal volume averaging effects are taken into account (as shown in the inset of Figure 8.3).
In Figure 8.3 the experimental photoelectron spectra recorded at $2 \cdot 10^{13}$ W/cm^2 and the ninety degree contribution are compared to respectively, the focal volume averaged TDSE and statistical model. The major difference that remains between the experiment and our calculations originates from the effect of the light electric field on the thermal contribution [137]. The light electric field induces an increase of the electron kinetic energy along the laser polarization which considerably increases the apparent temperature along this axis. Using angle-resolved

measurements allows an accurate determination of the effective thermal contribution.

8.6 Conclusion

We have measured the velocity distribution of photoelectrons emitted from C_{60} molecules irradiated by an intense short IR femtosecond laser pulse. TDSE calculations starting from individual molecular states show a very structured angular distribution assigned to the high angular momentum of the continuum wavefunction and to possible holographic effects. By contrast, the experimental angular distribution of the ATI peaks is structureless. As demonstrated, this is not a signature of the complexity of the molecule. On the contrary, C_{60} behaves as a "macro-atom" for which single electron ionization from a one-electron orbital produces the observed effect. Unlike the usual atomic situation, the $|m| = 1$ states dominate the ionization and the contribution of all m-states leads to a smooth angular distribution. Beyond this atomic-like effect, we have identified a loss of contrast in the ATI peaks that cannot be reproduced by SAE processes. This effect is related to the influence of electron-electron interactions and can be satisfactorily calculated using a statistical approach if the focal volume averaging is taken into account. This demonstrates that important information on the ionization dynamics can be obtained in ATI measurements for complex systems. Our work has allowed disentangling the various mechanisms at play in the C_{60} ionization while a fully satisfactory theoretical description would require a complete "ab-initio" calculation. Such calculation is under development but beyond the scope of this chapter.

References

[1] H. R. Hertz. *Ueber einen Einfluss des ultravioletten Lichtes auf die electrische Entladung.* Annalen der Physik, **57**, 983–1000 (1887).

[2] A. Einstein. *Ueber einen die Erzeugung und Verwandlung des Lichtes betreffenden heuristischen Gesichtspunkt.* Annalen der Physik, **322**, 132–148 (1905).

[3] P. B. Corkum. *Plasma Perspective on Strong-Field Multiphoton Ionization.* Phys. Rev. Lett., **71**, 1994–1997 (1993).

[4] P. M. Paul, E. S. Toma, P. Breger, G. Mullot, F. Auge, P. Balcou, H. G. Muller and P. Agostini. *Observation of a train of attosecond pulses from high harmonic generation.* Science, **292**, 1689–1692 (2001).

[5] E. Goulielmakis *et al. Single-cycle nonlinear optics.* Science, **320**, 1614–1617 (2008).

[6] A. H. Zewail. *Femtochemistry: Atomic-scale dynamics of the chemical bond.* J. Phys. Chem. A, **104**, 5660–5694 (2000).

[7] J. Itatani, F. Quere, G. L. Yudin, M. Y. Ivanov, F. Krausz and P. B. Corkum. *Attosecond streak camera.* Phys. Rev. Lett., **88**, 173903 (2002).

[8] M. Kitzler, N. Milošević, A. Scrinzi, F. Krausz and T. Brabec. *Quantum theory of attosecond XUV pulse measurement by laser dressed photoionization.* Phys. Rev. Lett., **88**, 173904 (2002).

[9] R. Kienberger *et al. Atomic transient recorder.* Nature, **427**, 817–821 (2004).

[10] M. Schultze *et al. Delay in Photoemission.* Science, **328**, 1658–1662 (2010).

[11] M. Uiberacker *et al. Attosecond real-time observation of electron tunnelling in atoms.* Nature, **446**, 627–632 (2007).

[12] M. Drescher, M. Hentschel, R. Kienberger, M. Uiberacker, V. Yakovlev, A. Scrinzi, T. Westerwalbesloh, U. Kleineberg, U. Heinzmann and F. Krausz. *Time-resolved atomic inner-shell spectroscopy.* Nature, **419**, 803–807 (2002).

[13] A. L. Cavalieri *et al. Attosecond spectroscopy in condensed matter.* Nature, **449**, 1029–1032 (2007).

[14] G. Sansone *et al. Electron Localization following Attosecond Molecular Photoionization.* Nature, 763–766 (2010).

[15] S. Baker, J. S. Robinson, C. A. Haworth, H. Teng, R. A. Smith, C. C. Chirila, M. Lein, J. W. G. Tisch and J. P. Marangos. *Probing proton dynamics in molecules on an attosecond time scale.* Science, **312**, 424–427 (2006).

[16] J. Itatani, J. Levesque, D. Zeidler, H. Niikura, H. Pepin, J. C. Kieffer, P. B. Corkum and D. M. Villeneuve. *Tomographic imaging of molecular orbitals.* Nature, **432**, 867–871 (2004).

[17] O. Smirnova, Y. Mairesse, S. Patchkovskii, N. Dudovich, D. Villeneuve, P. Corkum and M. Y. Ivanov. *High harmonic interferometry of multi-electron dynamics in molecules.* Nature, **460**, 972–977 (2009).

[18] C. S. Fadley. *Angle-resolved x-ray photoelectron spectroscopy.* Progress in Surface Science, **16**, 275 – 388 (1984).

[19] A. Szöke. *Ultrashort Laser Pulse Phenomena.* AIP Conference Proceedings No. 147, American Institute of Physics, New York ((1986)).

[20] J. J. Barton. *Photoelectron Holography.* Phys. Rev. Lett., **61**, 1356–1359 (1988).

[21] S. H. Xu, M. Keeffe, Y. Yang, C. Chen, M. Yu, G. J. Lapeyre, E. Rotenberg, J. Denlinger and J. T. Yates. *Photoelectron Diffraction Imaging for C_2H_2 and C_2H_4 Chemisorbed on Si(100) Reveals a New Bonding Configuration.* Phys. Rev. Lett., **84**, 939–942 (2000).

[22] J. Wider, F. Baumberger, M. Sambi, R. Gotter, A. Verdini, F. Bruno, D. Cvetko, A. Morgante, T. Greber and J. Osterwalder. *Atomically Resolved Images from Near Node Photoelectron Holography Experiments on Al(111).* Phys. Rev. Lett., **86**, 2337–2340 (2001).

[23] T. Greber. *Exploiting the photoelectron source wave with near-node photoelectron holography.* Journal of Physics: Condensed Matter, **13**, 10561 (2001).

[24] T. Matsushita, F. Z. Guo, M. Suzuki, F. Matsui, H. Daimon and K. Hayashi. *Reconstruction algorithm for atomic-resolution holography using translational symmetry.* Phys. Rev. B, **78**, 144111 (2008).

[25] A. Landers *et al. Photoelectron diffraction mapping: Molecules illuminated from within.* Phys. Rev. Lett., **8701**, 013002 (2001).

[26] S. X. Hu, L. A. Collins and B. I. Schneider. *Attosecond photoelectron microscopy of H-2(+).* Phys. Rev. A, **80**, 023426 (2009).

[27] F. Krasniqi, B. Najjari, L. Struder, D. Rolles, A. Voitkiv and J. Ullrich. *Imaging molecules from within: Ultrafast angstrom-scale structure determination of molecules via photoelectron holography using free-electron lasers.* Phys. Rev. A, **81**, 033411 (2010).

[28] B. McNeil. *First light from hard X-ray laser.* Nat. Photonics, **3**, 375–377 (2009).

[29] H. N. Chapman *et al. Femtosecond X-ray protein nanocrystallography.* Nature, **470**, 73–77 (2011).

[30] M. M. Seibert *et al. Single mimivirus particles intercepted and imaged with an X-ray laser.* Nature, **470**, 78–81 (2011).

[31] D. Gabor. *Nobel Lectures, Physics 1971-1980.* World Scientific, Singapore (1992).

[32] R. R. Freeman, T. J. McIlrath, P. H. Bucksbaum and M. Bashkansky. *Pondermotive effects on angular distributions of photoelectrons.* Phys. Rev. Lett., **57**, 3156–3159 (1986).

[33] P. Agostini, F. Fabre, G. Mainfray, G. Petite and N. K. Rahman. *Free-Free Transitions Following Six-Photon Ionization of Xenon Atoms.* Phys. Rev. Lett., **42**, 1127–1130 (1979).

[34] L. V. Keldysh. Zh. Eksp. Teor. Fiz., **47**, 1945 (1964). [Sov. Phys. JETP **20**, 1307 (1965)].

[35] G. G. Paulus, W. Nicklich, H. Xu, P. Lambropoulos and H. Walther. *Plateau in above threshold ionization spectra.* Phys. Rev. Lett., **72**, 2851–2854 (1994).

[36] H. B. van Linden van den Heuvel and H. G. Muller. *Multiphoton Processes.* Vol. 8 of Camebridge Studies in Modern Optics Camebridge University Press, Camebridge, pg 25 (1988).

[37] P. B. Corkum, N. H. Burnett and F. Brunel. *Above-Threshold Ionization in the Long-Wavelength Limit.* Phys. Rev. Lett., **62**, 1259–1262 (1989).

[38] K. C. Kulander, K. J. Schafer and J. L. Krause. *Super-Intense Laser-Atom Physics, NATO ASI Series B.* Plenium Press, New York, p. 95 (1992).

[39] R. R. Freeman, P. H. Bucksbaum, H. Milchberg, S. Darack, D. Schumacher and M. E. Geusic. *Above-threshold ionization with subpicosecond laser pulses.* Phys. Rev. Lett., **59**, 1092–1095 (1987).

[40] D. G. Arbó, S. Yoshida, E. Persson, K. I. Dimitriou and J. Burgdörfer. *Interference oscillations in the angular distribution of laser-ionized electrons near ionization threshold.* Phys. Rev. Lett., **96**, 143003 (2006).

[41] A. Rudenko, K. Zrost, C. D. Schröter, V. L. B. de Jesus, B. Feuerstein, R. Moshammer and J. Ullrich. *Resonant structures in the low-energy electron continuum for single ionization of atoms in the tunnelling regime.* J. Phys. B-At. Mol. Opt., **37**, L407–L413 (2004).

[42] C. I. Blaga, F. Catoire, P. Colosimo, G. G. Paulus, H. G. Muller, P. Agostini and L. F. DiMauro. *Strong-field photoionization revisited.* Nat. Phys., **5**, 335–338 (2009).

[43] T.-M. Yan, S. V. Popruzhenko, M. J. J. Vrakking and D. Bauer. *Low-Energy Structures in Strong Field Ionization Revealed by Quantum Orbits.* Phys. Rev. Lett., **105**, 253002 (2010).

[44] R. Wiehle, B. Witzel, H. Helm and E. Cormier. *Dynamics of strong-field above-threshold ionization of argon: Comparison between experiment and theory.* Phys. Rev. A, **67**, 063405 (2003).

[45] M. J. Nandor, M. A. Walker and L. D. Van Woerkom. *Angular distributions of high-intensity ATI and the onset of the plateau.* J. Phys. B-At. Mol. Opt., **31**, 4617–4629 (1998).

[46] V. Schyja, T. Lang and H. Helm. *Channel switching in above-threshold ionization of xenon.* Phys. Rev. A, **57**, 3692–3697 (1998).

[47] D. G. Arbó, E. Persson and J. Burgdörfer. *Time double-slit interferences in strong-field tunneling ionization.* Phys. Rev. A, **74**, 063407 (2006).

[48] D. G. Arbó, K. L. Ishikawa, K. Schiessl, E. Persson and J. Burgdörfer. *Intracycle and intercycle interferences in above-threshold ionization: The time grating.* Phys. Rev. A, **81**, 021403 (2010).

[49] F. Lindner, M. G. Schätzel, H. Walther, A. Baltuška, E. Goulielmakis, F. Krausz, D. B. Milošević, D. Bauer, W. Becker and G. G. Paulus. *Attosecond double-slit experiment.* Phys. Rev. Lett., **95**, 040401 (2005).

[50] R. Gopal *et al. Three-Dimensional Momentum Imaging of Electron Wave Packet Interference in Few-Cycle Laser Pulses.* Phys. Rev. Lett., **103**, 053001 (2009).

[51] T. Remetter *et al. Attosecond electron wave packet interferometry.* Nat. Phys., **2**, 323–326 (2006).

[52] M. Spanner, O. Smirnova, P. B. Corkum and M. Y. Ivanov. *Reading diffraction images in strong field ionization of diatomic molecules.* Journal of Physics B: Atomic and Molecular Physics, **37**, L243–L250 (2004).

[53] T. Zuo, A. D. Bandrauk and P. B. Corkum. *Laser-induced electron diffraction: A new tool for probing ultrafast molecular dynamics.* Chem. Phys. Lett., **259**, 313–320 (1996).

[54] H. Niikura, F. Legare, R. Hasbani, A. D. Bandrauk, M. Y. Ivanov, D. M. Villeneuve and P. B. Corkum. *Sub-laser-cycle electron pulses for probing molecular dynamics.* Nature, **417**, 917–922 (2002).

[55] M. Meckel *et al. Laser-induced electron tunneling and diffraction.* Science, **320**, 1478–1482 (2008).

[56] Y. Huismans *et al. Time-Resolved Holography with Photoelectrons.* Science, **331**, 61–64 (2011).

[57] X.-B. Bian, Y. Huismans, O. Smirnova, K.-J. Yuan, M. J. J. Vrakking and A. D. Bandrauk. *Subcycle interference dynamics of time-resolved photoelectron holography with midinfrared laser pulses.* Phys. Rev. A, **84**, 043420 (2011).

[58] M. Y. Ivanov, M. Spanner and O. Smirnova. *Anatomy of strong field ionization.* J. Mod. Opt., **52**, 165–184 (2005).

[59] M. J. Bakker, V. J. F. Lapoutre, B. Redlich, J. Oomens, B. G. Sartakov, A. Fielicke, G. von Helden, G. Meijer and A. F. G. van der Meer. *Intensity-resolved IR multiple photon ionization and fragmentation of C_{60}.* J. Chem. Phys., **132**, 074305 (2010).

[60] D. G. Arbó, K. I. Dimitriou, E. Persson and J. Burgdörfer. *Sub-Poissonian angular momentum distribution near threshold in atomic ionization by short laser pulses.* Phys. Rev. A, **78**, 013406 (2008).

[61] Z. Chen, T. Morishita, A.-T. Le, M. Wickenhauser, X. M. Tong and C. D. Lin. *Analysis of two-dimensional photoelectron momentum spectra and the effect of the long-range Coulomb potential in single ionization of atoms by intense lasers.* Phys. Rev. A, **74**, 053405 (2006).

[62] U. Fano. *Propensity rules: An analytical approach.* Phys. Rev. A, **32**, 617–618 (1985).

[63] A. Kohlhase and S. Kita. *Pulsed metastable atomic beam source for time-of-flight applications.* Rev. Sci. Instrum., **57**, 2925–2928 (1986).

[64] A. T. J. B. Eppink and D. H. Parker. *Velocity map imaging of ions and electrons using electrostatic lenses: Application in photoelectron and photofragment ion imaging of molecular oxygen.* Rev. Sci. Instrum., **68**, 3477–3484 (1997).

[65] G. A. Garcia, L. Nahon and I. Powis. *Two-dimensional charged particle image inversion using a polar basis function expansion.* Rev. Sci. Instrum., **75**, 4989–4996 (2004).

[66] K. J. Schafer and K. C. Kulander. *Energy analysis of time-dependent wave functions: Application to above-threshold ionization.* Phys. Rev. A, **42**, 5794–5797 (1990).

[67] K. C. Kulander and T. N. Rescigno. *Effective potentials for time-dependent calculations of multiphoton processes in atoms.* Comput. Phys. Commun., **63**, 523 (1991).

[68] K. J. Schafer. *The energy-analysis of time-dependent numerical wave functions.* Comput. Phys. Commun., **63**, 427–434 (1991).

[69] K. J. Schafer. *Strong Field Laser Physics.* Springer, New York (2008).

[70] W. Becker, F. Grasbon, R. Kopold, D. B. Milošević, G. G. Paulus and H. Walther. *Above-threshold ionization: From classical features to quantum effects.* Adv. At. Mol. Opt. Phys., **48**, 35–98 (2002).

[71] J. H. Posthumus. *The dynamics of small molecules in intense laser fields.* Rep. Prog. Phys., **67**, 623–665 (2004).

[72] H. A. Bethe and E. E. Sapleter. *Quantum Mechanics of One- and Two-Electron Atoms.* Springer-Verlag, Berlin (1957).

[73] J. J. Sakurai. *Modern Quantum Mechanics.* Addison Wesley, New York (1994).

[74] F. Krausz and M. Ivanov. *Attosecond physics.* Rev. Mod. Phys., **81**, 163–234 (2009).

[75] M. F. Kling and M. J. J. Vrakking. *Attosecond electron dynamics.* Annu. Rev. Phys. Chem., **59**, 463–492 (2008).

[76] D. Shafir, Y. Mairesse, D. M. Villeneuve, P. B. Corkum and N. Dudovich. *Atomic wavefunctions probed through strong-field light-matter interaction.* Nat. Phys., **5**, 412–416 (2009).

[77] G. G. Paulus, F. Grasbon, A. Dreischuh, H. Walther, R. Kopold and W. Becker. *Above-threshold ionization by an elliptically polarized field: Interplay between electronic quantum trajectories.* Phys. Rev. Lett., **84**, 3791–3794 (2000).

[78] J. Mauritsson, P. Johnsson, E. Mansten, M. Swoboda, T. Ruchon, A. L'Huillier and K. J. Schafer. *Coherent Electron Scattering Captured by an Attosecond Quantum Stroboscope.* Phys. Rev. Lett., **100**, 073003 (2008).

[79] W. Becker, A. Lohr and M. Kleber. *Effects of rescattering on above-threshold ionization.* Journal of Physics B: Atomic, Molecular and Optical Physics, **27**, L325 (1994).

[80] M. Lewenstein, K. C. Kulander, K. J. Schafer and P. H. Bucksbaum. *Rings in above-Threshold Ionization - a Quasi-Classical Analysis.* Phys. Rev. A, **51**, 1495–1507 (1995).

[81] M. J. J. Vrakking. *An iterative procedure for the inversion of two-dimensional ion/photoelectron imaging experiments.* Rev. Sci. Instrum., **72**, 4084–4089 (2001).

[82] B. R. Yang, K. J. Schafer, B. Walker, K. C. Kulander, P. Agostini and L. F. Dimauro. *Intensity-Dependent Scattering Rings in High-Order above-Threshold Ionization.* Phys. Rev. Lett., **71**, 3770–3773 (1993).

[83] G. G. Paulus, W. Becker, W. Nicklich and H. Walther. *Rescattering Effects in above-Threshold Ionization - a Classical-Model.* J. Phys. B-At. Mol. Opt., **27**, L703–L708 (1994).

[84] H. G. Muller. *An efficient propagation scheme for the time-dependent Schrodinger equation in the velocity gauge.* Laser Physics, **9**, 138–148 (1999).

[85] S. V. Popruzhenko and D. Bauer. *Strong field approximation for systems with Coulomb interaction.* J. Mod. Opt., **55**, 2573–2589 (2008).

[86] T. Brabec, M. Y. Ivanov and P. B. Corkum. *Coulomb focusing in intense field atomic processes.* Phys. Rev. A, **54**, R2551–R2554 (1996).

[87] G. L. Yudin and M. Y. Ivanov. *Physics of correlated double ionization of atoms in intense laser fields: Quasistatic tunneling limit.* Phys. Rev. A, **63**, 033404 (2001).

[88] Y. Mairesse *et al. High Harmonic Spectroscopy of Multichannel Dynamics in Strong-Field Ionization.* Phys. Rev. Lett., **104**, 213601 (2010).

[89] A. Becker and F. H. M. Faisal. *Intense-field many-body S-matrix theory.* J. Phys. B: At., Mol. Opt. Phys., **38**, R1 (2005).

[90] O. Smirnova, M. Spanner and M. Ivanov. *Analytical solutions for strong field-driven atomic and molecular one- and two-electron continua and applications to strong-field problems.* Phys. Rev. A, **77**, 033407 (2008).

[91] F. H. M. Faisal. *Multiple absorption of laser photons by atoms.* Journal of Physics B: Atomic and Molecular Physics, **6**, L89 (1973).

[92] H. R. Reiss. *Effect of an intense electromagnetic field on a weakly bound system.* Phys. Rev. A, **22**, 1786–1813 (1980).

[93] R. Kopold, W. Becker and M. Kleber. *Quantum path analysis of high-order above-threshold ionization.* Opt. Commun., **179**, 39–50 (2000).

[94] T. Marchenko, H. G. Muller, K. J. Schafer and M. J. J. Vrakking. *Electron angular distributions in near-threshold atomic ionization.* J. Phys. B-At. Mol. Opt., **43**, 095601 (2010).

[95] K. C. Kulander, K. J. Schafer and J. L. Krause. *Atoms in Intense Laser Fields*. Academic, New York (1992).

[96] H. R. Reiss. *Novel Phenomena in Very-Low-Frequency Strong Fields*. Phys. Rev. Lett., **102**, 143003 (2009).

[97] A. D. Bandrauk, S. Chelkowski and S. Goudreau. *Control of harmonic generation using two-colour femtosecondattosecond laser fields: quantum and classical perspectives*. Journal of Modern Optics, **52**, 411–428 (2005).

[98] W. Quan *et al. Classical Aspects in Above-Threshold Ionization with a Mid-infrared Strong Laser Field*. Phys. Rev. Lett., **103**, 093001 (2009).

[99] A. D. Shiner, B. E. Schmidt, C. Trallero-Herrero, H. J. Wörner, S. Patchkovskii, P. B. Corkum, J.-C. Kieffer, F. Légaré and D. M. Villeneuve. *Probing collective multi-electron dynamics in xenon with high-harmonic spectroscopy*. Nat. Phys., **7**, 464 (2011).

[100] E. Cormier and P. Lambropoulos. *Above-threshold ionization spectrum of hydrogen using B-spline functions*. Journal of Physics B: Atomic, Molecular and Optical Physics, **30**, 77 (1997).

[101] X. M. Tong and C. D. Lin. *Empirical formula for static field ionization rates of atoms and molecules by lasers in the barrier-suppression regime*. Journal of Physics B: Atomic, Molecular and Optical Physics, **38**, 2593 (2005).

[102] D. B. Milošević, W. Becker, M. Okunishi, G. Prümper, K. Shimada and K. Ueda. *Strong-field electron spectra of rare-gas atoms in the rescattering regime: enhanced spectral regions and a simulation of the experiment*. Journal of Physics B: Atomic, Molecular and Optical Physics, **43**, 015401 (2010).

[103] `http://www.nist.gov/index.html`.

[104] H. Bachau, E. Cormier, P. Decleva, J. E. Hansen and F. Martin. *Applications of B-splines in atomic and molecular physics*. Rep. Prog. Phys., **64**, 1815 (2001).

[105] X.-B. Bian and A. D. Bandrauk. *Phase control of multichannel molecular high-order harmonic generation by the asymmetric diatomic molecule HeH^{2+} in two-color laser fields*. Phys. Rev. A, **83**, 023414 (2011).

[106] L.-Y. Peng and A. F. Starace. *Application of Coulomb wave function discrete variable representation to atomic systems in strong laser fields*. The Journal of Chemical Physics, **125**, 154311 (2006).

[107] Y.-C. Han and L. B. Madsen. *Comparison between length and velocity gauges in quantum simulations of high-order harmonic generation*. Phys. Rev. A, **81**, 063430 (2010).

[108] T. J. Park and J. C. Light. *Unitary quantum time evolution by iterative Lanczos reduction.* The Journal of Chemical Physics, **85**, 5870–5876 (1986).

[109] X. Guan, O. Zatsarinny, K. Bartschat, B. I. Schneider, J. Feist and C. J. Noble. *General approach to few-cycle intense laser interactions with complex atoms.* Phys. Rev. A, **76**, 053411 (2007).

[110] N. B. Delone and V. P. Krainov. *Energy and Angular Electron-Spectra for the Tunnel Ionization of Atoms by Strong Low-Frequency Radiation.* J. Opt. Soc. Am. B, **8**, 1207–1211 (1991).

[111] A. M. Perelomov, V. S. Popov and M. V. Terent'ev. Sh. Eksp. Teor. Fiz., **50**, 1393 (1966). [Sov. Phys. JETP **23**, 924 (1966)].

[112] A. B. Yedder, C. Le Bris, O. Atabek, S. Chelkowski and A. D. Bandrauk. *Optimal control of attosecond pulse synthesis from high-order harmonic generation.* Phys. Rev. A, **69**, 041802(R) (2004).

[113] R. Kienberger *et al. Steering attosecond electron wave packets with light.* Science, **297**, 1144–1148 (2002).

[114] D. B. Milošević, G. G. Paulus, D. Bauer and W. Becker. *Above-threshold ionization by few-cycle pulses.* J. Phys. B-At. Mol. Opt., **39**, R203–R262 (2006).

[115] F. Rohmund, M. Heden, A. V. Bulgakov and E. E. B. Campbell. *Delayed ionization of C_{60}: The competition between ionization an fragmentation revisited.* J. Chem. Phys., **115**, 3068 (2001).

[116] E. E. B. Campbell, K. Hansen, K. Hoffmann, G. Korn, M. Tchaplyguine, M. Wittmann and I. V. Hertel. *From above threshold ionization to statistical electron emission: The laser pulse-duration dependence of C-60 photoelectron spectra.* Phys. Rev. Lett., **84**, 2128–2131 (2000).

[117] F. Lépine and C. Bordas. *Time-dependent spectrum of thermionic emission from hot clusters: Model and example of* C_{60}. Phys. Rev. A, **69**, 053201 (2004).

[118] I. Shchatsinin, T. Laarmann, G. Stibenz, G. Steinmeyer, A. Stalmashonak, N. Zhavoronkov, C. P. Schulz and I. V. Hertel. *C-60 in intense short pulse laser fields down to 9 fs: Excitation on time scales below e-e and e-phonon coupling.* J. Chem. Phys., **125**, 194320 (2006).

[119] M. Boyle, T. Laarmann, K. Hoffmann, M. Hedén, E.E.B. Campbell, C.P. Schulz and I.V. Hertel. *Excitation dynamics of Rydberg states in C_{60}.* Eur. Phys. J. D, **36**, 339–351 (2005).

[120] I. V. Hertel, I. Shchatsinin, T. Laarmann, N. Zhavoronkov, H.-H. Ritze and C. P. Schulz. *Fragmentation and Ionization Dynamics of* C_{60} *in Elliptically Polarized Femtosecond Laser Fields.* Phys. Rev. Lett., **102**, 023003 (2009).

[121] A. Jaroń-Becker, A. Becker and F. H. M. Faisal. *Saturated Ionization of Fullerenes in Intense Laser Fields.* Phys. Rev. Lett., **96**, 143006 (2006).

[122] M. Ruggenthaler, S. V. Popruzhenko and D. Bauer. *Recollision-induced plasmon excitation in strong laser fields.* Phys. Rev. A, **78**, 033413 (2008).

[123] W. Kohn and L. J. Sham. *Self-Consistent Equations Including Exchange and Correlation Effects.* Phys. Rev., **140**, A1133–A1138 (1965).

[124] D. Bauer, F. Ceccherini, A. Macchi and F. Cornolti. C_{60} *in intense femtosecond laser pulses: Nonlinear dipole response and ionization.* Phys. Rev. A, **64**, 063203 (2001).

[125] J. P. Perdew and A. Zunger. *Self-interaction correction to density-functional approximations for many-electron systems.* Phys. Rev. B, **23**, 5048–5079 (1981).

[126] M. J. Puska and R. M. Nieminen. *Photoabsorption of Atoms inside C60.* Phys. Rev. A, **47**, 1181–1186 (1993).

[127] M. Boyle, K. Hoffmann, C. P. Schulz, I. V. Hertel, R. D. Levine and E. E. B. Campbell. *Excitation of Rydberg series in C-60.* Phys. Rev. Lett., **87**, – (2001).

[128] L. F. Ruiz, P. A. Hervieux, J. Hanssen, M. F. Politis and F. Martn. *Molecular view of charge exchange in ionC60 collisions.* International Journal of Quantum Chemistry, **86**, 106–113 (2002).

[129] A. Rudel, R. Hentges, U. Becker, H. S. Chakraborty, M. E. Madjet and J. M. Rost. *Imaging delocalized electron clouds: Photoionization of C-60 in Fourier reciprocal space.* Phys. Rev. Lett., **89**, – (2002).

[130] E. Cormier, P.-A. Hervieux, R. Wiehle, B. Witzel and H. Helm. *ATI of complex systems: Ar and* C_{60}. Eur. Phys. J. D, **26**, 83–90 (2003).

[131] A. Rentenier *et al. Absolute Charge Transfer and Fragmentation Cross Sections in* He^{2+}-C_{60} *Collisions.* Phys. Rev. Lett., **100**, 183401 (2008).

[132] Y. Pavlyukh and J. Berakdar. *Angular electronic band structure of molecules.* Chemical Physics Letters, **468**, 313 – 318 (2009).

[133] N. Troullier and J. L. Martins. *Structural and electronic properties of* C_{60}. Phys. Rev. B, **46**, 1754–1765 (1992).

[134] R. Schlipper, R. Kusche, B. V. Issendorff and H. Haberland. *Thermal emission of electrons from highly excited sodium clusters.* Appl. Phys. A, **72**, 255 (2001).

[135] V. Weisskopf. *Statistics and Nuclear Reactions.* Phys. Rev., **52**, 295–303 (1937).

[136] S. Diaz-Tendero, M. Alcami and F. Martin. *Structure and electronic properties of highly charged C[sub 60] and C[sub 58] fullerenes.* The Journal of Chemical Physics, **123**, 184306 (2005).

[137] M. Kjellberg, O. Johansson, F. Jonsson, A. V. Bulgakov, C. Bordas, E. E. B. Campbell and K. Hansen. *Momentum-map-imaging photoelectron spectroscopy of fullerenes with femtosecond laser pulses.* Phys. Rev. A, **81**, 023202 (2010).

[138] M. Kjellberg. *Ionization of Large Molecules with Short Laser Pulses.* Ph.D. thesis (2010).

Summary

The motion of molecules, atoms and electrons govern many processes in and around us. Following their motion in realtime is therefore relevant for many scientific fields. The dynamics of interest is however fast; femtoseconds for molecular dynamics up to attoseconds for electron dynamics. To capture such fast motion, one needs a technique with a "shutter time" of the same order of magnitude as this motion, or faster, just as with a conventional camera. The required femtosecond to attosecond shutter time is usually achieved by irradiating the sample with a short pulsed laser. Creating a movie can subsequently be achieved by applying a so called "pump probe" technique in which a pump starts a certain reaction and, some time later, a probe images the status of the reaction. By varying the pump-probe delay, the evolution of the system can be monitored.

By for example using pump-probe techniques, in combination with femtosecond pulsed laser or electron sources, it is possible to follow the femtosecond motion of molecules. This is part of an active research field, called "femtochemistry", for which the pioneer, Ahmed Zewail, received the Nobel price in 1999. The recent advent of new light sources, such as the LCLS in Stanford, offer the perspective of real time measuring the structural changes in molecules by diffraction. By applying spectroscopy techniques, this was sofar only possible in an indirect way. Time-resolved diffraction offers the possibility to study much larger and complex molecules.

Following the ultrafast motion of electrons is another challenge, since their motion is three orders of magnitude faster than the motion of molecules and no standard laser system can offer such short pulses. Only recently two techniques have emerged that have the required attosecond "shutter time". Both techniques are based on the high harmonic generation process (HHG). The process starts with the ionization of an atomic or molecular gas target upon irradiation by a femtosecond infrared laser. Once in the continuum, the electrons oscillate under the influence of the laser field and can be driven back to the target ion. Here they can recombine, forming a light spectrum of odd harmonics of the fundamental laser frequency. Upon proper tuning, this spectrum of high harmonics can constitute an attosecond pulse, which, thanks to its short pulse duration, can be used to follow the attosecond electron dynamics in real time. The HHG process itself can also be viewed as a pump (ionization) - probe (recombination) experiment, storing the time and spatial information in the light spectrum itself. Both methods are currently used to unravel electron dynamics in atoms and small molecules.

This thesis attempts to unravel structure and dynamics via quite a different way, namely by looking at the photoelectrons that are emitted in an intense laser

field - target interaction. In such an interaction, the photon energy is usually much smaller than the ionization potential and ionization proceeds in a non-linear way, by absorbing a number of photons. In the continuum, the motion of the electrons will be governed by the laser; electrons will make an oscillatory motion on their way to the detector and they will in certain cases even collide with the target atom. The resulting photoelectron spectra carry a wealth of information about the electrons themselves and on the target. With a velocity map imaging (VMI) spectrometer, the three dimensional velocity distribution of the ionized electrons can be measured, storing most of the information available. By performing calculations, it is possible to uncover this information. Throughout the thesis this is done for different circumstances, and different targets.

Imaging xenon Rydberg states

In view of the question whether electrons also carry information about the shape of the atomic orbitals, we have investigated the ionization from selected Rydberg orbitals in atomic xenon in Chapter 2. Due to their low ionization potential, long wavelengths (i.e. small energy photons) with sufficient intensity are required in order to perform a multiphoton ionization experiment. These are available at the Free Electron Laser for IntraCavity Experiments (FELICE) in Rijnhuizen. By ionizing 12s, 11p, 11d and 8f Rydberg states, prepared in different magnetic quantum states m_ℓ, with a wavelength of $\lambda_{laser} = 31.2$ µm, we could demonstrate that each Rydberg orbital leaves its own specific fingerprint on the final photoelectron distribution. Furthermore the ionization dynamics was investigated by ionizing 10s and 11p Rybderg states with wavelengths between 21 µm to 31 µm. By performing various theoretical calculations, we have succesfully analyzed the patterns observed in the photoelectron spectra and their underlying electron dynamics from two viewpoints. Firstly by analyzing the patterns in the frequency domain, by regarding the ionization as a multiphoton absorption process, in which the momentum of the electron changes according to the selection rules for photon absorbtion. Secondly by analyzing them in the time domain, i.e. by analyzing the electron wave packet interferences with a semi-classical model. With the latter model it was furthermore possible to pinpoint which type of interference leads to certain patterns. The presented analysis demonstrates that structural and dynamical information is indeed encoded in the final three dimensional photoelectron spectrum and that, depending on the information of interest, observed patterns can be analyzed in either the frequency or the time domain.

Strong field photoelectron holography

The concept of holography, as invented by Gabor in 1947, can also be applied to strong field laser physics. In conventional holography methods, a coherent beam of light is split into an object beam, which illuminates an object and a reference beam. When these two beams are brought together on a detector, they form a

hologram, i.e. an interference pattern that stores the spatial information of the object. In strong field holography a coherent beam of electrons is created by strong field ionization. The object and reference wave are subsequently created by the influence of the laser field on the continuum photoelectrons. If a photoelectron is ionized with zero velocity in the direction orthogonal to the laser polarization, the laser will drive this electron back to its parent ion, where it can scatter, forming an object wave. If the photoelectron is ionized with a certain orthogonal velocity component it will turn around the ion and reach the detector without scattering, forming a reference wave. The interference of these photoelectron wave packets on a detector will constitute a hologram of the target ion. In Chapter 3 we show the first experimental proof of such a hologram in xenon, ionized with 7 µm light from the FELICE source. Furthermore, by carrying out a theoretical analysis, which is outlined in detail in Chapter 4, it was possible to reveal that such a hologram also contains temporal information on both the target ion and the electron on timescales of respectively femtosecond to attosecond timescale. In Chapter 5, the evolution of the pattern with wavelength, intensity and pulse duration is investigated, both experimentally and theoretically. As expected, the hologram does not change its shape with pulse duration, since the pattern is generated within one laser cycle. The intensity changes the holographic fringes only slightly. This explains the observability of the hologram in an experiment, where ionization always happens by the range of intensities that are available in the focal spot of the laser. The fringe spacing does change drastically with wavelength. By applying a semiclassical model, it can be shown analytically that this change in spacing is due to the change in time spent in the continuum by the photoelectron. In Chapter 3 and 5 only holograms observed with mid-infrared wavelengths are presented. To obtain an empirical law for the observation of the hologram, a much larger wavelength and intensity space is investigated in Chapter 6. It turns out that the electrons' ponderomotive energy, i.e. its quiver energy in the laser electric field, should be large compared to the photon energy.
The photoelectrons that form the strong field hologram are ionized within a quarter laser cycle. This is however not the only sub-cycle interference pattern that can be formed. In Chapter 7 a detailed theoretical investigation is performed in order to distinguish all possible sub-cycle interference patterns. This shows that the above discussed holographic interference is the only interference that creates a pattern in the angular direction. All other sub-cycle interferences create patterns in the radial direction. Consequently the hologram is the only easily distinguishable pattern. In the last part of this chapter it is furthermore shown that the holographic pattern is sensitive to the shape of the atomic orbital.

All in all we have given the first experimental proof of the strong field photoelectron hologram, shown that it contains both spatial and temporal information on the time and length scales relevant for molecules and electrons. Furthermore we have thoroughly investigated the pattern for a wide range of laser parameters and for different atomic orbitals. In order to study electron or molecular dynamics,

further investigations are required to build methods that can retrieve the spatial and temporal information from the hologram.

Imaging a large and complex molecule

Extracting information is most valuable if it can be done for molecules. In Chapter 8 the large and complex C_{60} molecule is investigated. With a wavelength of 800 nm, a pulse duration of about 30 fs and a whole range of intensities, C_{60} is ionized. The resulting three dimensional photoelectron velocity distribution is analyzed using two theoretical models. Though C_{60} has many electrons, the first model regards the system as a "single active electron" system, in which electron correlations play no role. Since the observed smooth photoelectron angular distribution can be well reproduced with this model, C_{60} can be regarded as a kind of super atom, in which electron correlations play only a minor role. The residual effect of electron correlations shows up in a smoothing of the radial structures, as demonstrated by the applied statistical model.

The presented experimental and theoretical investigations show that photoelectrons carry information about the structure of atomic orbitals and about the ionization dynamics in atoms and large molecules. Of special interest are the strong field photoelectron holograms that are able to store both Ångström spatial and femtosecond temporal information of the target and attosecond temporal information on electron dynamics.

Samenvatting

Veel van wat er in en om ons heen gebeurt wordt aangestuurd door processen die voor ons onzichtbaar zijn. Deze vinden plaats op het niveau van kleine deeltjes die we niet met het blote oog kunnen zien, zoals moleculen, atomen en elektronen. Of het nu gaat om het opnemen van medicijnen in ons lichaam, het lichtgeven van sommige kwallen, het omzetten van licht naar energie in planten of in zonnecellen, de werking van de computer, het zijn uiteindelijk de bewegingen van deze deeltjes die hieraan ten grondslag liggen. Omdat ze zo'n cruciale rol vervullen, zijn er vele wetenschapsgebieden die zich bezig houden met de bestudering van deze deeltjes en in het bijzonder met hun beweging. Voor het bestuderen van de bewegingen van moleculen zijn de eerste technieken al enkele tientallen jaren geleden ontwikkeld. Het volgen van elektronen is echter nog een stap ingewikkelder, omdat deze nog sneller en kleiner zijn dan moleculen. Met de komst van de zogenaamde "attoseconde laser", zo'n tien jaar geleden, is hier verandering in gekomen.
Er is ook een andere, meer indirecte manier om veel informatie te verzamelen over moleculen, atomen en hun elektronen. Door met intens laserlicht een molecuul of atoom te beschijnen, kan het elektron als het ware weggeschoten worden. Door vele van deze elektronen te meten, is het mogelijk om terug te rekenen waar ze vandaan komen of welke pad ze hebben gevolgd. Dit hebben we[1] voor verschillende systemen gedaan. Daarnaast hebben we op deze wijze ook een hologram kunnen maken van een atoom, en dat met de elektronen uit het atoom zelf. Dit is heel bijzonder, omdat zo'n hologram niet alleen informatie bevat over de vorm van het atoom, maar ook over de beweging van zowel het atoom als de elektronen. Dit zou het begin kunnen zijn van een nieuwe techniek om deze snelle bewegingen in kaart te brengen.

De ultra snelle camera

Wat zijn elektronen ook alweer, wat is hun rol en hoe kunnen we dit meten? Om deze dingen te begrijpen beginnen we bij atomen. Dit zijn kleine deeltjes om ons heen, waaruit alles is opgebouwd. Bekende atomen zijn bijvoorbeeld waterstof, zuurstof, koolstof, calcium, goud, uranium. Het woord atoom komt van het Griekse woord 'atomos', wat ondeelbaar betekent. Vroeger geloofde men dat dit de kleinst bestaande deeltjes waren, nu weten we dat atomen uit nog kleinere deeltjes zijn opgebouwd, maar nog steeds beschouwen we atomen als de "legosteentjes" van

[1] Hoewel dit proefschrift over mijn onderzoek gaat, heb ik dit niet alleen uitgevoerd. In samenwerking met een groot aantal collega's uit binnen en buitenland, is het werk dat ik presenteer tot stand gekomen. Vandaar dat ik refereer naar 'wij' en niet naar 'ik'.

ons leven. Een blok goud bestaat dus uit vele goudatomen bij elkaar, en water uit de atomen zuurstof en waterstof. Een atoom zelf bestaat uit een positief geladen kern, waar omheen negatief geladen deeltjes bewegen die we elektronen noemen en welke centraal staan in dit proefschrift. Elektronen hebben namelijk een bijzondere rol. Meestal vinden we atomen namelijk niet geïsoleerd, maar vormen ze een molecuul. Deze kan bestaan uit slechts twee atomen, maar ook uit vele miljarden. Dat een molecuul niet uit elkaar valt is te danken aan de elektronen, die de bindingen vormen tussen de verschillende atomen. Als er een verandering optreedt in het molecuul, doordat het bijvoorbeeld van vorm of grootte verandert, dan spelen elektronen een cruciale rol; zij vormen immers de "lijm". Alle processen in en om ons heen worden gestuurd door de beweging van moleculen, atomen en dus ook van elektronen. Daarom zijn vele wetenschappers bezig om deze bewegingen te bestuderen. Echter, door de hoge snelheid van deze deeltjes valt het niet mee om deze te volgen. De langzaamste van deze deeltjes, het molecuul, beweegt al op een tijdschaal van picoseconde (10^{-12} s) tot femtoseconde (10^{-15} s). Dit is een miljoen tot een miljard keer sneller dat het klapperen van de vleugels van een bij, en zelfs dat kunnen we al niet volgen met onze ogen! Hele snelle camera's kunnen dit wel. Dit kunnen ze door een hele korte sluitertijd te gebruiken. Hierdoor is het mogelijk om toch een scherpe afbeelding te maken van iets dat snel beweegt. Door kort achter elkaar plaatjes te maken met zo'n korte sluitertijd is het mogelijk om een film te maken en deze bijvoorbeeld heel langzaam af te spelen, zodat onze ogen de beweging ook nog kunnen volgen. Moleculen zijn echter te klein en bewegen te snel om met een normale camera te bekijken. Daarom hebben we een andere methode nodig. Meestal wordt dit gedaan door middel van lasers met een korte pulseduur. De korte pulseduur zorgt als het ware voor een korte belichtingstijd van het proces, zodat - ook al is het indirect - er toch een scherp beeld kan worden genomen. Maar met alleen een scherp beeld is de film niet af. Om een film te maken moeten we een hele verzameling beeldjes achter elkaar plakken. Dit kan door middel van de zogenaamde "pomp-probe" techniek. Eerst wordt met bijvoorbeeld een laserpuls een reactie aangezet, bijvoorbeeld het opbreken van een molecuul. Dan wordt op een later tijdstip met een tweede laserpuls gemeten hoever het molecuul al opgebroken is. Door steeds het tijdstip tussen het aanzetten van de reactie (pomp) en het meten van de status (probe) te variëren kan er een film worden gemaakt.

De snelle beweging van elektronen

Al sinds tientallen jaren bestaan er lasers met een pulsduur die kort genoeg is om de beweging van moleculen te meten. Echter, voor het meten van de elektronenbeweging hebben we een laser met een pulsduur nodig van attoseconden (10^{-18} s), wat duizend miljard keer sneller is dan het klapperen van de vleugels van een bij. Tot voor kort bestond er nog geen techniek die dit kon, maar sinds in 2001 via een complex proces een attoseconde laser is ontwikkeld, worden de hele snelle

bewegingen van elektronen in atomen en moleculen bestudeerd. In dit proefschrift onderzoeken we via een hele andere methode de structuur en beweging van moleculen, atomen en voornamelijk elektronen. De nadelen van deze methode zijn de indirecte wijze van meten, waardoor niet alle bewegingen in kaart kunnen worden gebracht, en de analyse vaak complex is. Voordelen zijn echter de eenvoud van de methode en de mogelijkheid om met een andere kleur licht te werken, wat de bestudering van andere systemen mogelijk maakt.
Met deze methode wordt eerst een elektron "weggeschoten" bij het atoom door middel van de laser. Vervolgens gaat het elektron een op- en neergaande beweging uitvoeren, omdat het laserlicht als een golf kan worden beschouwd die de elektronen op en neer laat bewegen. Na een tijdje wordt het elektron opgevangen en gemeten met een speciale detector die oplicht op de plaats waar een elektron terechtkomt. Dan kunnen we vervolgens terugrekenen waar het elektron vandaan kwam. Het idee van het terugrekenen werkt als volgt. Stel er ligt een bal ergens achter een hoge muur. Dan laat jij iemand die bal oppakken en een aantal stappen vooruit zetten, een paar stappen opzij, nog een paar stappen vooruit, net zolang tot je diegene ziet. Hij of zij legt de bal neer, en omdat jij weet hoeveel stappen diegene heeft gezet, en welke kant op, is het mogelijk om terug te rekenen waar de bal oorspronkelijk lag.

Welk pad heeft het elektron gevolgd en waar kwam het vandaan?

Het terugrekenen is in ons geval een stukje ingewikkelder, we schieten namelijk heel veel elektronen weg, en kijken dan naar het totaalplaatje wat ze geven op de detector (elektronenplaatje). Vervolgens rekenen we niet alleen terug waar deze elektronen vandaan kwamen, maar ook nog welk pad ze hebben gevolgd. Een voorbeeld van zo'n elektronenplaatje is Figuur 1. Hier zijn een aantal ringen te zien, met in elke ring lichte en donkere delen. In Hoofdstuk 2 van het proefschrift hebben we uitgerekend dat deze lichte en donkere delen in elke ring worden veroorzaakt door een interferentiepatroon van elektronen. Volgens de kwantummechanica, een beroemde theorie in de natuurkunde, kunnen we elektronen niet alleen beschouwen als deeltjes, maar ook als golf. Dit is een ongrijpbaar feit, maar wel cruciaal voor ons onderzoek. Hierdoor kunnen elektronen namelijk ook "interfereren". En zoals verschillende golven in water door interferentie een speciaal patroon kunnen vormen, kunnen elektronen dat dus ook. Als nu deze "elektrongolfpakketjes", die op verschillende momenten vrijkomen en andere paden volgen, op dezelfde plek op de detector terechtkomen, kunnen ze elkaar door interferentie versterken of juist uitdoven. De ringen die te zien zijn in Figuur 1, zijn een voorbeeld van zo'n elektron-interferentiepatroon, en de donkere en lichte vlekken in elke ring zijn weer een voorbeeld van een ander elektron-interferentiepatroon. Welke interferentie dat is, hebben we in dit hoofdstuk laten zien.

Iets anders dat we in dit hoofdstuk hebben aangetoond, is dat de baan van het atoom waaruit het elektron komt, een "vingerafdruk" nalaat op het uiteindelijke

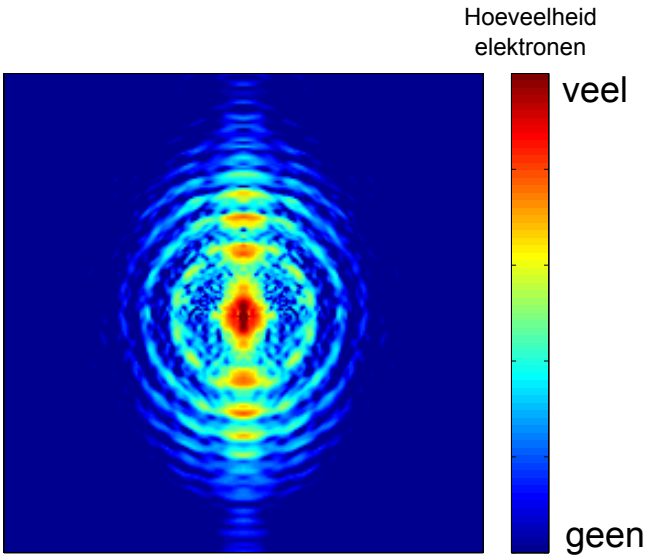

Figuur 1: Elektronenplaatje. Elektronen die in het midden terecht komen hebben weinig tot geen snelheid. Hoe verder de elektronen bij het centrum vandaan komen, hoe hoger hun snelheid. In het figuur zijn ringen zichtbaar die kunnen worden beschouwd als een interferentiepatroon. In elke ring is weer een patroon zichtbaar dat bestaat uit een afwisseling van lichte en donkere plekken. Ook dit is een interferentiepatroon.

elektronenplaatje. Deze banen worden orbitalen genoemd. Er zijn banen die zich dichtbij de kern van het atoom bevinden en banen die ver weg liggen, net zoals er verschillende planeetbanen om de zon zijn. Maar hier houdt de vergelijking op, want de banen van elektronen vormen geen eenvoudige ellipsen. In Figuur 2a zijn de verschillende orbitalen weergegeven. Het s-orbitaal is een ingekleurde bol, wat betekent dat het elektron zich overal in deze bol kan begeven. Bij het p-orbitaal kan het elektron zich overal in de twee weergegeven bollen begeven. Zo heeft elke orbitaal z'n eigen vorm. In Figuur 2b staat een elektronenplaatje van elektronen uit een f-orbitaal, deze bestaat, net als de s-orbitaal uit Figuur 1, uit een hele serie ringen. We hebben ook elektronenplaatjes gemeten van de andere orbitalen (niet te zien in het figuur). Om goed de verschillen tussen de elektronenplaatjes te zien, hebben we gekeken naar de elektronenverdeling op de eerste ring, zoals aangegeven met de stippellijn in Figuur 2b. Hoe deze elektronenverdeling eruit ziet is weergegeven in Figuur 2c, met de lichtblauwe lijn. Hoe sterker het elektronensignaal bij een bepaalde hoek, hoe hoger de lijn. In dit figuur kunnen we nauwkeurig bekijken hoe deze verdeling er bij 180 graden uitziet (zie stippellijn). Voor een s-orbitaal is er een sterke piek te zien bij deze hoek, er komen dus veel elektronen bij 180 graden terecht. Bij de p-orbitaal verschijnt er een kleine, bijna onzichtbare, dip bij 180 graden. Deze dip wordt groter voor de d-orbitaal, en voor

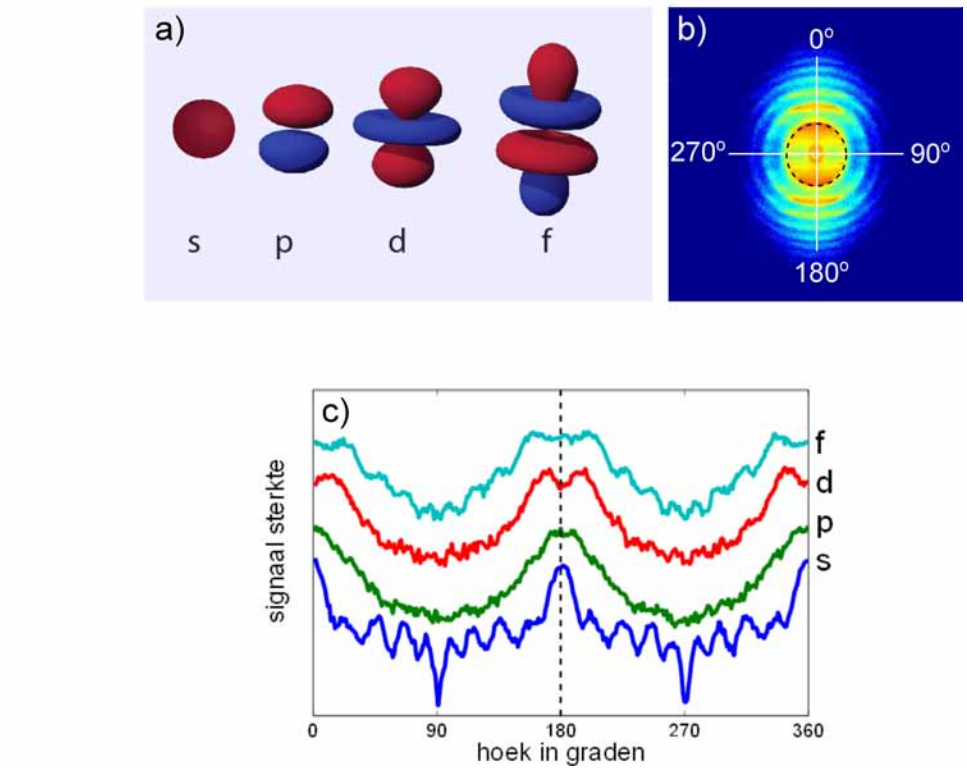

Figuur 2: a) Verschillende atoom-orbitalen. Overal waar het rood of blauw gekleurd is kunnen zich elektronen bevinden. b) Elektronen plaatje zoals in Figuur 1, maar nu van een f-orbitaal. De assen geven aan hoe de hoeken gedefinieerd zijn. c) Elektronen opbrengst versus de hoek, zoals aangegeven in subfiguur b). Bij 180 graden is er een groot verschil tussen de orbitalen s, p, d en f. Voor de s-orbitaal is de verdeling nog een scherpe piek, maar voor de f-orbitaal is het een hele brede piek geworden.

de f-orbitaal verschijnt er een nieuwe bult in de dip. Hoe de verdeling er rond 180 graden uitziet, hangt dus af van of het elektron uit het s-, p-, d-, of f-orbitaal komt. Hieruit kunnen we concluderen dat het niet alleen mogelijk is om te achterhalen welke paden elektronen moeten volgen om een bepaald interferentiepatroon te kunnen maken (Figuur 1), maar ook uit welk type orbitaal het elektron komt (Figuur 2).

Atoom maakt hologram van zichzelf

Een belangrijk deel van het proefschrift (Hoofdstuk 3 tot en met 7) gaat over het maken van een hologram van een atoom. In holografie wordt de vorm van een object opgeslagen in een interferentiepatroon dat we een hologram noemen. Dit wordt mogelijk gemaakt door het golfkarakter van het licht of van de elektronen die in de meting gebruikt worden. Het holografieconcept werd al in 1947

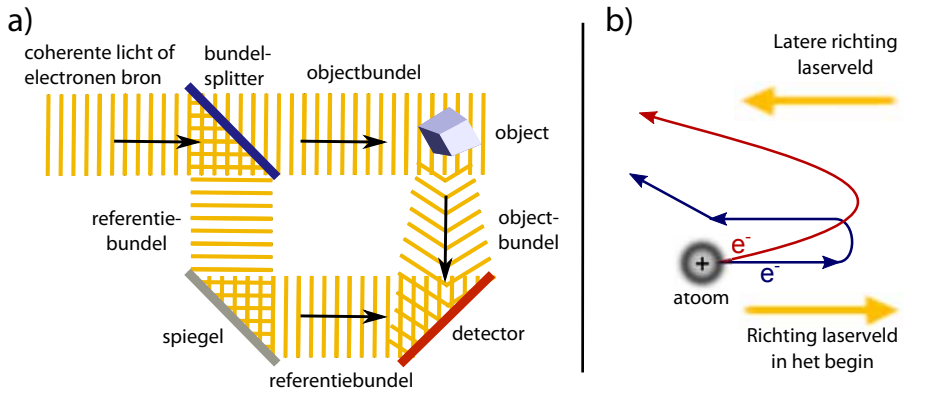

Figuur 3: Deze figuren geven aan hoe a) het algemene concept van holografie werkt en b) hoe ditzelfde concept kan worden gebruikt in een atoom dat wordt beschenen door een intense laser. Een gedetailleerde uitleg van beide concepten wordt gegeven in de tekst.

geïntroduceerd door Gabor en kent tegenwoordig vele toepassingen, waaronder het bekende "regenboogplaatje" in de creditcard. In Figuur 3a is schematisch weergegeven hoe holografie werkt. Eerst wordt een (coherente) golf in tweeën gesplitst, door middel van een spiegel die de helft doorlaat en de helft een andere kant opstuurt. De doorgelaten golf gaat rechtdoor en verstrooit aan het te bestuderen object. Via weer een spiegel wordt deze verstrooide golf naar een detector gebracht. Deze golf noemen we de objectgolf. De afgebogen golf gaat via een andere spiegel ook naar de detector. Deze golf noemen we de referentiegolf. Als de object- en referentiegolf bij elkaar komen, vormen ze een interferentiepatroon, waarin de vorm van het object is opgeslagen. In Hoofdstuk 3 laten we zien dat dit concept ook kan worden toegepast op atomen die worden geïoniseerd (dit is het weghalen van een elektron bij het atoom) met intens laserlicht. Het idee wordt weergegeven in Figuur 3b. Eerst wordt een elektron door de interactie met het intense laser licht uit het atoom gehaald. Afhankelijk van de richting waarin het elektron vrijkomt, zal het een bepaald pad volgen. Als het met een bepaalde snelheid vrijkomt die loodrecht staat op de richting waarin het laserveld het elektron heen en weer beweegt, dan volgt het elektron de rode lijn en maakt het een wijde boog om het atoom heen. Als het elektron precies in de richting vrijkomt waarin het op en neer wordt bewogen door het laserveld, dan zal het laserveld het elektron ook weer terugbrengen bij het atoom, waar het kan botsen en een andere kant op kan gaan (blauwe lijn). Elektronen die het rode pad volgen kunnen als referentiegolf worden beschouwd, zij bewegen immers met een wijde boog om het atoom heen en zullen niet botsen. Elektronen die het blauwe pad volgen vormen de objectgolf; zij botsen met het atoom alvorens ze naar de detector gaan. Als deze twee elektrongolfpakketten op de detector terechtkomen vormen ze een inter-

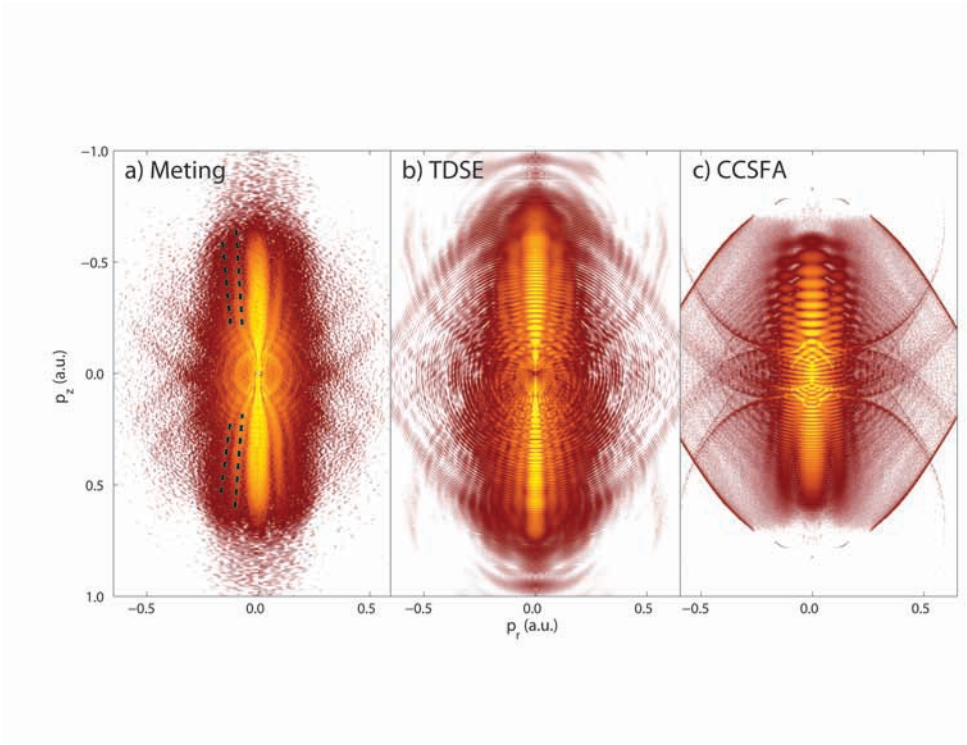

Figuur 4: Meting en berekeningen van het hologram. a) Het gemeten hologram. Met zwarte stippellijnen wordt aangegeven welk patroon het hologram is. b) Met de hele nauwkeurige ' TDSE' methode hebben we het patroon nagerekend. c) Om meer inzicht te krijgen, hebben we het ook met een versimpelde methode nagerkend. Met deze methode kunnen we precies narekenen welk pad een elektron heeft gevolgd dat op een bepaald punt terecht is gekomen. Met een nog simpeler model (niet weergegeven hier) hebben we bovendien aangetoond dat het hologram ook tijd informatie bevat over zowel het atoom als het elektron.

ferentiepatroon waarin de vorm van het atoom is opgeslagen, een hologram van het atoom!

In Figuur 4a is het resultaat te zien. De kleur geeft aan hoeveel elektronen ergens terecht zijn gekomen: rood zijn veel elektronen, geel een paar en wit geen. Met de stippellijn is het patroon aangegeven dat het hologram is van het atoom. Dit is, voor zover wij weten, het eerste experimentele bewijs dat het mogelijk is een hologram te maken van een atoom, met de elektronen uit het atoom zelf. We hebben dit gedaan onder hele specifieke condities. Ten eerste hebben we het atoom xenon gebruikt. De reden hiervoor is heel praktisch; xenon is makkelijk om mee te werken en er zijn al heel veel metingen aan gedaan. Hierdoor maken we het onszelf niet onnodig moeilijk en hebben we veel vergelijkingsmateriaal. Daarnaast hebben we een hele speciale laser gebruikt, namelijk de "Free Electron Laser for

IntraCavity Experiments" (FELICE). Wat bijzonder is aan deze laser is dat het heel intens mid-infrarood licht geeft, iets dat op maar een aantal plekken in de wereld beschikbaar is.

Om het achterliggende proces tot in detail te begrijpen, hebben we drie verschillende theoretische methoden gebruikt om na te rekenen wat we in Figuur 4a hebben gemeten. Het klinkt onzinnig om drie methoden te gebruiken, er is per slot van rekening maar één waarheid, die we willen uitrekenen. Maar omdat het zo complex is, kunnen we het zelf niet uitrekenen en bestaan er ook geen computers die snel en krachtig genoeg zijn om het exact uit te kunnen rekenen. Daarom moeten we het model versimpelen. We hebben dit op drie manieren gedaan. Ten eerste door een model te gebruiken dat de situatie bijna helemaal exact uitrekent. Het resultaat is te zien in Figuur 4b en komt goed overeen met de meting in Figuur 4a. Dit model is echter zo ingewikkeld, dat het alleen mogelijk is om op het niveau van de wiskunde te begrijpen wat er gebeurt. Het achterhalen van fysische informatie, zoals welke paden elektronen volgen en wanneer ze vrij komen uit het atoom is echter moeilijk. Daarom gebruiken we twee versimpelde methoden die uitgebreid beschreven worden in Hoofdstuk 4. Hoewel deze modellen een minder goede overeenstemming geven met de werkelijkheid, geven ze wel veel inzicht. Het resultaat van één van deze modellen is te zien in Figuur 4c. Met nog weer een ander model hebben we kunnen aantonen dat dit hologram niet alleen informatie opslaat over de vorm van het atoom, maar ook over de beweging van het atoom en van de elektronen! En dan ook nog op de tijdschaal die relevant is voor het bestuderen van deze bewegingen, namelijk femtoseconden voor het atoom en attoseconden voor het elektron.

Om de holografie beter te begrijpen hebben we in Hoofdstuk 5 door middel van experimenten en theoretische modellen uitgezocht hoe het hologram verandert als je de sterkte, de kleur en pulsduur van de laser verandert. In Hoofdstuk 6 zijn we dieper ingegaan op de vraag wanneer je een hologram kunt meten, welke kleuren lasers daarvoor geschikt zijn en welke sterkte je nodig hebt. Op basis van metingen en berekeningen hebben we hiervoor een empirische wet gevonden. In het laatste hoofdstuk over holografie, Hoofstuk 7, berekenen we alle soorten patronen die kunnen ontstaan als je elektrongolfpakketen met elkaar laat interfereren. Dan blijkt dat je heel veel verschillende patronen kunt maken, maar dat alleen het holografie patroon goed te onderscheiden valt van andere patronen, waardoor het dus extra geschikt is om informatie uit te halen.

Al met al hebben we dus laten zien dat het mogelijk is om een hologram van een atoom te maken, met de elektronen die uit het atoom zelf komen. Daarnaast hebben we door middel van theoretische modellen kunnen uitrekenen dat dit hologram niet alleen informatie bevat over de vorm van het atoom, maar ook tijd informatie over zowel het atoom als de elektronen. Om te zien of deze methode echt een nieuwe en aanvullende methode kan worden in het meten van de hele snelle elektronenbeweging en ook voor het meten van veranderingen in de structuur van moleculen, moeten er nog een aantal dingen gebeuren. Ten eerste moeten

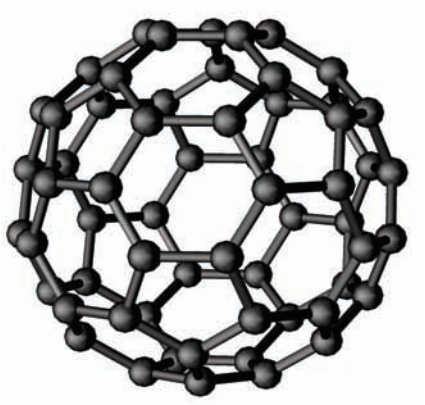

Figuur 5: C_{60} is een atoom dat bestaat uit 60 koolstofatomen en heeft de vorm van een voetbal.

we uitvinden hoe we de informatie die in het hologram opgeslagen zit er uit kunnen halen. Ten tweede is het belangrijk om experimenten met moleculen uit te gaan voeren, want die zijn een stuk interessanter dan losse atomen.

Het grote C_{60} molecuul

In Hoofdstuk 2 tot en met 7 hebben we naar het elektronsignaal gekeken om zoveel mogelijk tijd- en ruimtelijke informatie te verkrijgen over de atomen en elektronen. Maar in de meeste gevallen zijn we in de praktijk niet geïnteresseerd in de beweging van elektronen in atomen, maar in hun beweging in moleculen, want het zijn de veranderingen in moleculen, die zo relevant zijn voor alle processen in en om ons heen. Daarom hebben we in Hoofdstuk 8 een modelstudie uitgevoerd op C_{60}. Dit is een groot molecuul dat uit 60 koolstofatomen bestaat, zoals geïllustreerd in Figuur 5. Omdat C_{60} redelijk groot is en niet te complex (het bestaat alleen maar uit koolstofatomen), is dit een mooi modelmolecuul om effecten te bestuderen die niet of nauwelijks voorkomen in atomen en kleine moleculen, maar wel in grote, zoals een sterke interactie van elektronen met elkaar of de verspeiding van energie in het molecuul. Om te bekijken in hoeverre deze effecten een rol spelen, hebben we C_{60} geïoniseerd door middel van laserlicht. Hiermee stoppen we dus energie in het systeem en kunnen we bekijken in hoeverre deze door elektron-elektron interactie of andere interacties wordt verdeeld. Door naar het elektronenplaatje te kijken en deze na te rekenen, hebben we aangetoond dat C_{60} nog steeds voor een groot deel kan worden beschouwd als een soort van superatoom, waarin maar één elektron reageert op het licht en niet meerdere. De interactie met andere elektronen is dus niet dominant, maar deze is er wél, want we hebben een vervaging van bepaalde patronen gemeten die volgens onze berekeningen veroorzaakt worden door deze elektron-elektron interactie.

Samenvatting

Al met al hebben we dus laten zien dat we elektronen, die uit het atoom of molecuul worden getrokken door intens laser licht heel goed kunnen gebruiken om informatie te krijgen over de beweging van elektronen, de interactie met andere elektronen en de orbitaal waar ze zich oorspronkelijk in bevonden. Verder hebben we een aanzet gegeven in het ontwikkelen van een nieuwe methode om zowel tijd- als ruimtelijke informatie te meten van moleculen, atomen en elektronen. En dat allemaal op een ultrasnelle tijdschaal, femtoseconden voor de moleculen tot atteseconden voor de electronen.

Acknowledgements

Pile Higher and Deeper (PhD) is a famous comic among PhD students, which illustrates the ups and downs of an average PhD life. Well, I've certainly piled higher and deeper during my PhD, but the average definitely tends towards positive. With satisfaction I look back on a very nice time, both socially and scientifically and for this I would like to thank a large number of people.

First, my promoter Marc Vrakking. Marc, with you as a supervisor - running around with tons of nice ideas and working together with many scientists - there were always more projects than time. Stepping on the PhD train in your group is realizing that you took the high speed train that, once in the right direction, would take you far. I had to push the emergency break sometimes, but unlike reality there was never a penalty. The train took me along experiments at free electron lasers, international collaborations, conferences in snow and burning sun, collaboration in Berlin and Baton Rouge and many other things. Though regularly tough, it was a great experience. Marc, I will remember you as a challenging group leader, always trying to get the best out of me, being very enthusiastic and involved in my projects and always optimistic. Thanks for the high speed train ride!

Though being the last Chapter, C_{60} was my first project, followed by a long collaboration with Franck Lépine. Franck, it was a pleasure to carry out the C_{60} experiments with you and I have appreciated all the time you took to explain me details about the calculations and interpretations over and over again.

Most of my experiments I carried out at FELICE, for which I would like to thank the Rijnhuizen Crew: Lex van der Meer, Britta Redlich, Joost Bakker and Chiel Berden. You all made it a great pleasure to perform the beamtime-runs at FELICE, thanks for the assistance, the help, the explanations, for borrowing the YAG laser and for the extra care from Britta for the personal side! Verder wil ik hier ook heel graag de operatoren Jules en Cor bedanken voor alle hulp, vooral in de nachtelijke uren (zoals het regelen van een waterstofzuiger, zodat we ons waterballet weer konden opruimen). En natuurlijk Michel en Rene voor alle technische assistentie! I would also like to thank all the people from AMOLF and other institutes who joined one or both experimental runs at FELICE. Cecilia, Franck, Sébastien, Arjan, Arnaud, Aneta, Julia and Paul, thank you for all the effort!

After almost two years of experimental work, I started on the analysis and interpretation, which I enjoyed a lot. My great wish was to do some calculations myself. Olga Smirnova gave me the opportunity to write a code for calculating

and analyzing the hologram. This was a great experience. Olga, under your supervision I learned so much in such a short time. I felt privileged to work together with such a bright, creative mind and with such a warm and kind person. Olga, many thanks for the great time in Berlin! While being in Berlin, I got to know Misha Ivanov too. He regularly joined the discussions of Olga and me, with very valuable input. Cheering us up when we thought we would never get there (it's a catastrophe!) and giving me numerous private lessons on theory. Thank you Misha, for being such an educative, positive and patient person! During the same time I got in contact with Sergey Popruzhenko and Dieter Bauer, both theoreticians and experts on the CCSFA method. It has been very nice, discussing with you and meeting you at the Max Born Institute or at conferences. Thanks for all the explanations and the contribution to the Science paper.

In February 2011 I visited Ken Schafer in Baton Rouge, Lousiana (US). In the Netherlands it was raining, in Baton Rouge it was 25 degrees, sunny and the trees were blooming. But this was not the only nice part of the visit. In these weeks Ken taught me all the ins and outs the TDSE-code. Ken, thanks for all the very educative explanations, the scientific discussions we had, your hospitality and for trusting me not to lose the key again of the bike you borrowed me!

Towards the end of my PhD there were a few other collaborations that started, all on the holography. Tatiana, thanks for all the discussions. I have appreciated your clear way of writing and your very careful reading of all my documents! Xue-Bin, it was a short but fruitful collaboration and I was impressed by your very fast response time to any email I sent. Predrag and Daniel, we have had quite a number of very interesting discussions. Though I felt often too busy (it was my last year of PhD), I always enjoyed our Skype conversations a lot. I hope the paper gets accepted soon.

Reading a thesis and joining the defense is quite a time investment. Femius Koenderink, Wilhelm Becker, Dave Parker, Ronnie Hoekstra, Gerhard Paulus and Bernhard Piraux, thank you for accepting to be in my thesis and/or reading committee.

Dat het op AMOLF prettig werken is, komt voor een groot deel door de ontzettend goede ondersteuning daar. Graag wil ik een ieder bedanken van de receptie, kantine, technische dienst, P&O, financiële afdeling, bibliotheek en magazijn, voor alle ondersteuning en de prettige sfeer. Ook aan de technische kant valt niet te klagen. Voor de verschillende bundeltijden moesten er vele zaken onder hoge tijdsdruk geregeld worden. Duncan, Ronald, Itsart, bedankt voor al jullie ondersteuning op het gebied van Electronica en Ronald dankjewel voor je nauwe betrokkenheid bij FELICE en je cursus. Op het gebied van ICT was ik niet de makkelijkste klant, ik had enorm veel ruimte nodig op de XUV server en ik versleepte de AMOLF computers naar andere instituten. Ik ben erg blij met alle ondersteuning die ICT heeft gegeven. Verder wil ik natuurlijk de tekenkamer en de werkplaats bedanken voor het ontwerpen en bouwen van onderdelen en ma-

chines, bedankt voor de goede ondersteuning en het meedenken.

Hinco, Ad en Rob, onze groepstechnici, verdienen ook een dikke pluim! Ik hoefde maar een kik te geven of jullie stonden klaar om het op te lossen. Echt zo fijn! Ad, ik wil je bedanken voor al je hulp, en in het bijzonder je doorzettingsvermogen om op FELICE na onze computercrash toch de dye-laser sturing weer aan de praat te krijgen! Hinco, jij hebt het tijdens FELICE een paar keer moeten ontzien, "Hinco, de metastabiele bron is stuk, kun je deze op stel en sprong repareren??!" En natuurlijk die keer dat je ik je per ongeluk de hele nacht lege sms-jes stuurde, omdat ik bij het licht van mijn telefoon wilde lezen en me niet realiseerde dat ik, door het actief houden van mijn beeldscherm, automatisch lege sms-jes stuurde... Hinco, bedankt voor alle hulp en je goede humeur!

Rob, dank je wel!!!! Naast je tomeloze inzet voor de experimenten ook voor je rol als 'vader van de groep'. Gaat het wel goed met de PhD's, werken ze niet te hard, hebben ze een zetje in de rug of een positief woordje nodig? Het was duidelijk dat je niet alleen wilde dat onze experimenten goed gingen maar ook dat we ons er goed bij voelden. Bedankt daarvoor en heel veel plezier straks als je met pensioen gaat, met je vrouw, je kinderen en kleinkinderen!

On the "high speed train" I had very nice fellow travelers. When I joined, the group was small, but very 'gezellig en hecht'. Going out for drinks, organizing dinners and movie nights, celebrating Sinterklaas, sailing and trips to Sweden, it was great fun. I've also appreciated all the mental support in times when it was though, especially Wing Kiu and Georg where a great help. Arjan, jij was de eerste met wie ik samenwerkte en die mij alle details leerde van de VMI. Je bent zeer nauw betrokken geweest bij mijn grootste projecten (FELICE en C_{60}) en ik ben erg blij geweest met jouw bijdrage, je geduld, en de wandelingetjes die we maakten als ik dacht dat ik het allemaal niet kon. Hoewel we een totaal andere werkwijze hadden heb ik met veel plezier met je samengewerkt. Paul, bedankt voor de goede samenwerking en je grote betrokkenheid bij het C_{60}- en het FELICE-project. Ik wens je veel plezier en succes met je promotie aan de UvA! Omair, it was short, but nice to have you around, especially your humor! Per, det var mycket roligt att har dig med i gruppen. Jag har många fina minnen av middagarna hemma hos dig i Amsterdam och midsommarfirandet tillsammans med kollegor hos dina frldrar vid Östersjökusten. Arnaud, we've worked a lot together. I've always been impressed by how much you know and how skilled you are. It was tough, all these weeks at FLASH, but it was nice to work there with you. Thanks also for your great hospitality in Berlin, with all the good care and delicious French cheese and wine! Freek, het is indrukwekkend hoe scherp jij vragen kunt stellen en kunt analyseren. Ik heb genoten van alle felle discussies die je met mij of anderen voerde en natuurlijk van al het schaatsen. Ik had nooit gedacht dat jij degene zou zijn die iemand anders zou overtuigen om vrij te nemen van het werk! Wing Kiu, in het begin waren we de enige twee vrouwen, en wat was ik blij dat ik niet de enige was! Wij hebben misschien niet veel samengewerkt, maar ik had je niet willen missen!

De gezelligheid, alle gesprekken, je steun als het even moeilijk was, dank je wel! Georg, op twee weken na zijn we tegelijk begonnen. In het oude AMOLF gebouw zaten we op één kantoor en dat was erg leuk. Je enthousiasme en creativiteit zijn erg aanstekelijk en ook aan jou heb ik veel gehad als het even moeilijk was. Julia en Aneta, met jullie heb ik op FELICE heel nauw samengewerkt. Normaal zijn bundeltijden vooral zwaar, maar met jullie was het ook heel leuk! Werken met jullie ging heel efficient, en hoewel het technisch soms flink tegen zat, hebben we met z'n drieën - en natuurlijk ook met de hulp van de anderen - een erg geslaagd experiment kunnen uitvoeren op FELICE. Julia en Aneta, jullie zijn twee spontane en lieve meiden, met wie ook de laatste maanden op AMOLF allerminst saai waren, ook al waren we maar met z'n drieën over. Bedankt voor het FELICE experiment , alle constructieve en snelle commentaren op artikelen en presentaties en voor natuurlijk alle gezelligheid! About a year before the group moved to Berlin, we expanded. Axel, Fede, Christian, Chung Hsin, Jesse, Truong, it was nice with such a diverse group of people and I enjoyed all the diners and drinks we had, especially the famous Sangria evening... Daarnaast wil ik de groep van Ron Heeren bedanken voor het adopteren van Aneta en mij, toen Marc en andere collega's verhuisd of gepromoveerd waren.

During my time in Amsterdam, I was spoiled to live right in the Pijp, together with other AMOLFers and some non-AMOLFers. Marco, Rutger, Alette, Behnaz, Gianluca, Jose, Yael and Tom, thanks for the nice time and dinners in the Eerste Jan Steenstraat!

AMOLF is famous for its coffee breaks. One might think we're lazy, but I honestly think it really adds to a positive working atmosphere. Marjon, Marina, Maaike, Paolo, James, Johannes, Klaas-Jan, Bergin, Chris, Ernst-Jan, Ruben and many others, thanks for the nice conversations!

Beside my own group and the people at AMOLF, I would like to thank the group of Olga in Berlin. Although I joined the group for only half a year, I felt very welcome. Maria, Zac, Filipe, Alex, Olga and Misha, thanks for the nice time together, for the dinners, wine tasting and poetry night. You guys made my stay in Berlin a great pleasure!

Om lekker in mijn vel te zitten en met plezier te werken, zijn mijn vrienden en familie van onschatbare waarde. Vanaf de basisschool heb ik een groepje vrienden verzameld die me erg dierbaar zijn met wie ik kan lachen en kan huilen en die er altijd voor me zijn. Marleen, Marjolein, Else, Bernadette, Ingrid, Maarten, Thijs, Michiel, Hilgien, Laura, Marijn, Anisa, Lennie, dank jullie wel! En natuurlijk, Joost, Johan, Vero, Aad, Joost, Hilde, Linda, Sander, Arend, Evert-Jan, Mathijs, Feiko, Hugo, Hans, Marjon, Thijs, Irene, Maartje, Jochem, Kasja, Joost, Inge, Matthijs, dank jullie wel voor de feestjes, etentjes, weekenden, spelletjesavonden, wandelingen en vele andere leuke momenten! Martijn, Hendrike, Eamon, Annechien, Auke en Marjanne, bedankt voor alle leuke weekenden, Oud & Nieuw, Erria en andere feestjes! Ina and Maria, thanks for the nice trips to Germany and

your visits to the Netherlands!

Marijn en Laura, ik heb jullie al genoemd, maar ik ga het nog een keertje doen! Laura, het was misschien maar een jaar dat we samen in Amsterdam hebben gewoond, maar ik mis het nog steeds om elke donderdagavond samen te eten, bij te kletsen en te Lindy-Hoppen! Marijn, jou kwam ik tegen in Nepal. En ook al kenden we elkaar amper, we zijn samen door de Kathmandu vallei gaan fietsen, en dat klikte! Terug in Nederland hebben we veel samen gedaan, op toneel, zwemmen, naar theater, naar de bios en altijd een bedje voor me klaar in Amsterdam, toen ik al naar Rotterdam was verhuisd. We hebben echt lief en leed met elkaar gedeeld deze afgelopen vier jaar en ik hoop dat we dat nog heel lang blijven doen!

Je ouders kies je niet, maar ik mag absoluut niet klagen! Mama, dank je voor je Friese nuchterheid, je onvoorwaardelijke liefde, je zorg, je steun en voor alle weekenden en vakanties samen! Papa, bedankt voor alle goede zorgen, het geruststellen, het altijd vragen en interesse tonen! En mijn lieve “kleine” broertje ;) Geert Willem naast dat ik natuurlijk heel trots op je ben, vind ik het eigenlijk vooral leuk dat we het zo goed met elkaar vinden!

Een schoonmoeder en een vriendin van je vader kies je natuurlijk ook niet, maar ook hier heb ik niet te klagen. Frederike en Brigit, ook jullie bedankt voor alle gezelligheid, goede zorgen en gastvrijheid!

Lieve Klaas, ik ben ontzettend blij met jou. Met jou ben ik stabieler, rustiger, blijer. Als ik te hard werk, fluit jij me terug, als ik sip ben, beur jij me op. Samen naar theater, naar concerten, naar de klimhal (jij 6c of 7a overwinnen en ik mijn proefschrift schrijven), wandelen in Lapland of Peru, heel hard fietsen (en afzien...) om de boot te halen, naar Erria, muziek maken, schaatsen in de winter, we doen zoveel leuke dingen, ik hoop dat we dat nog heel lang samen blijven doen!

Ymkje Huismans, 11 Maart 2012, Rotterdam

List of publications

Publications covered in this thesis:

Photo-electron angular distributions from the ionization of xenon Rydberg states by mid-infrared radiation, Y. Huismans, A. Rouzé, A. Gijsbertsen, P. S. W. M. Logman, F. Lépine, C. Cauchy, S. Zamith, J. M. Bakker, G. Berden, B. Redlich, A.F.G. van der Meer, K.J. Schafer and M. J. J. Vrakking, *manuscript in preparation* (*Chapter 2*)

Time-Resolved Holography with Photoelectrons, Y. Huismans, A. Rouzée, A. Gijsbertsen, J. H. Jungmann, A. S. Smolkowska, P. S. W. M. Logman, F. Lépine, C. Cauchy, S. Zamith, T. Marchenko, J. M. Bakker, G. Berden, B. Redlich, A. F. G. van der Meer, H. G. Muller, W. Vermin, K. J. Schafer, M. Spanner, M. Yu. Ivanov, O. Smirnova, D. Bauer, S. V. Popruzhenko, M. J. J. Vrakking, in Science **331**, 61 (2011) (*Chapter 3 and 4*)

Scaling laws for photoelectron holography in the mid-infrared wavelength regime, Y. Huismans, A. Gijsbertsen, A. S. Smolkowska, J. H. Jungmann, A. Rouzée, P. S. W. M. Logman, F. Lépine, C. Cauchy, S. Zamith, T. Marchenko, J. M. Bakker, G. Berden, B. Redlich, A. F. G. van der Meer, M. Yu. Ivanov, T. -M. Yan, D. Bauer, O. Smirnova and M. J. J. Vrakking, *submitted* (*Chapter 5*)

Criteria for the observation of strong-field photoelectron holography, T. Marchenko, Y. Huismans, K. J. Schafer, and M. J. J. Vrakking, in Phys. Rev. A **84**, 053427 (2011) (*Chapter 6*)

Subcycle interference dynamics of time-resolved photoelectron holography with midinfrared laser pulses, Xue-Bin Bian, Y. Huismans, O. Smirnova, Kai-Jun Yuan, M. J. J. Vrakking, and André D. Bandrauk, in Phys. Rev. A **84**, 043420 (2011) (*Chapter 7*)

Macro-atom vs many-electron effects in ultrafast ionization of C_{60}, Y. Huismans, E. Cormier, C. Cauchy, P.-A. Hervieux, G. Gademann, A. Gijsbertsen, O. Ghafur, P. Johnsson, P. Logman, C. Bordas, F. Lépine and M.J.J. Vrakking, *manuscript in preparation* (*Chapter 8*)

Other related publications:

Direct visualization of laser-driven electron multiple-scattering in strong-field ionization, Daniel D. Hickstein, Predrag Ranitovic, Stefan Witte, Xiao-Min Tong, Ymkje Huismans, Paul Arpin, Xibin Zhou, K. Ellen Keister, Craig W. Hogle, Bosheng Zhang, Chengyuan Ding, Per Johnsson, N. Toshima, Marc J. J. Vrakking, Margaret M. Murnane, and Henry C. Kapteyn *submitted*

List of publications

Angle-resolved photoelectron spectroscopy of sequential three-photon triple ionization of neon at 90.5 eV photon energy, A. Rouzée, P. Johnsson, E. V. Gryzlova, H. Fukuzawa, A. Yamada, W. Siu, Y. Huismans, E. Louis, F. Bijkerk, D. M. P. Holland, A. N. Grum-Grzhimailo, N. M. Kabachnik, M. J. J. Vrakking, and K. Ueda, in Phys. Rev. A **83**, 031401(R) (2011)

Characterization of a two-color pumpprobe setup at FLASH using a velocity map imaging spectrometer P. Johnsson, A. Rouzée, W. Siu, Y. Huismans, F. Lépine, T. Marchenko, S. Düsterer, F. Tavella, N. Stojanovic, H. Redlin, A. Azima, and M. J. J. Vrakking, Optics Letters **35**, 4163-4165 (2010)

Velocity map imaging using an in-vacuum pixel detector, Georg Gademann, Ymkje Huismans, Arjan Gijsbertsen, Julia Jungmann, Jan Visschers, and Marc J. J. Vrakking, Rev. Sci. Instrum. **80**, 103105 (2009)

Field-free molecular alignment probed by the free electron laser in Hamburg (FLASH), P. Johnsson, A. Rouzée, W. Siu, Y. Huismans, F. Lépine, T. Marchenko, S. Düsterer, F. Tavella, N. Stojanovic, A. Azima, R. Treusch, M. F. Kling and M. J. J. Vrakking, J. Phys. B **42**, 134017 (2009)

About the author

Ymkje Huismans was born in Amsterdam in 1982. Shortly after, the family moved via Friesland to Delden, a village in the eastern part of the Netherlands. Here she grew up and attended secondary school in Hengelo, at Scholengemeenschap Twickel. After obtaining her degree in 2001, she moved to Groningen, where she started her studies in Physics at the University of Groningen. She followed a broad scope of subjects, varying from theoretical physics to climate studies. In her Bachelor research she studied the interaction of the solar wind with comets, a topic with aspects from atomic- and astrophysics. Her Master research was an international project, performed in Groningen at the Zernike Institute for Advanced Materials, in Sweden at the Ångström Laboratory of the University of Uppsala and at the Synchrotron facilities in Lund (Sweden) and Triëste (Italy). This condensed matter topic focussed on the intercalation of organic crystals and the effect on their conduction properties. Besides her studies, Ymkje has been a member of several boards and committees, among which the faculty board of the Science Faculty at the University of Groningen.
After graduating in summer 2007, she spent three months in Nepal, where she taught English and Math in a primary school in Kathmandu. Back in the Netherlands she started her PhD research in the group of Marc Vrakking at the FOM-Institute AMOLF in Amsterdam. The results of this research are presented in this thesis.